Min, Liang (2024) *Flexible control and optimisation of multi-energy systems.* PhD thesis.

https://theses.gla.ac.uk/84345/

Flexible Control and Optimisation of Multi-Energy Systems

Liang Min

Submitted in fulfilment of the requirements for the
Degree of Doctor of Philosophy (Ph.D.)

Electronics and Electrical Engineering
James Watt School of Engineering
University of Glasgow

January 2024

Abstract

With the deterioration of the environment and the increasing severity of the energy crisis, the UK government sets the Net Zero 2050 plan. Under this context, the traditional power distribution networks, struggling to adapt to the demands of local renewable energy generation (REG), low-carbon technology, and energy storage, are transforming to active distribution networks (ADNs) with soft open points (SOPs) as a flexible control device for enhanced operational efficiency. Meanwhile, to overcome the limitations of a single energy vector, the multi-energy system (MES), which can utilise the complementary advantages of different energy vectors, becomes a promising solution, especially in facilitating the integration of REGs. As the natural gas network has a mature infrastructure across the UK and the technologies of gas-fired units (GFU) and power-to-gas (P2G) can contribute to the constitution of the energy loop between electricity and gas, the electricity-gas MES become a hot research area. Selecting the electricity-gas MES as the key solution, this PhD research investigates the impact of SOPs on improving the operation of ADNs and explores the role of electricity-gas MES in facilitating the integration of REGs.

For the SOP, the technology is advanced at the converter level, focusing on topology, control, and strategy to improve the operational efficiency of ADNs. The three-phase four-wire (3P4W) back-to-back (B2B) converter is investigated as the new topology of SOPs. Based on the new topology, a new control scheme and the operational strategy are developed. The simulation shows that the 3P4W-B2B converter based ASP-SOP can achieve load balancing and phase imbalance in the unbalanced ADNs.

For the ADN, an optimal operation strategy based on developed ASP-SOPs is proposed to enhance the performance of unbalanced ADNs. The effects of different types of ASP-SOPs is compared. For the first time, in the SOP-based optimisation of ADN, the symmetrical semidefinite programming (SDP) is applied to solve the three-phase optimal power flow problem. The case study demonstrates that the proposed method can achieve a power loss reduction of up to

49.83% and an imbalance reduction of up to 77.68%.

For the MES, encompassing both ADNs and natural gas networks, a comprehensive operational coordination optimisation approach is designed to not only minimise the operational costs, the curtailment of REGs and carbon emissions but also enable simultaneous analysis of both energy vectors' networks. Additionally, a graph-based model is developed for directly solving the nonlinear optimisation problems in stochastic MES, considering the uncertainties associated with variable REG. The results of case studies indicate that the proposed optimisation method for MESs can reduce the total operational cost by 21.81%, the overall carbon emissions by 33.95% and the curtailment of wind power generations by 94.41%. Furthermore, the implementation of ASP-SOP can significantly mitigate the voltage imbalance condition in three-phase power systems, improving it by up to 36.82%.

Acknowledgements

I would like to express my deepest gratitude to my supervisor, Dr. Jin Yang, for his exceptional expertise, understanding, patience, and guidance. His invaluable support has been a cornerstone of my PhD research and thesis development.

My sincere thanks also go to Dr. Chengwei Lou for contributing his insights and inspiration to my research.

I am profoundly grateful to Dr James Yu from Scottish Power, the Energy Technology Partnership (ETP), and the University of Glasgow for granting me the Studentship, which has been instrumental in my academic journey.

Additionally, my heartfelt appreciation goes to the dedicated staff at the University of Glasgow. Their ceaseless assistance, friendly support, and commitment to creating an environment of enthusiasm and academic rigour have greatly enriched my experience.

Lastly, I would like to extend my warmest thanks to my friends and family. Their unwavering support, constant encouragement, and belief in my abilities have been the foundation of my perseverance.

Author’s Declaration

I declare that, except where the reference is made to the contributions of others, this dissertation is the result of my own work and has not been submitted for any other degree at the University of Glasgow or any other institution.

Liang Min

16/05/2024

Contents

List of Tables

List of Figures

Abbreviations and Nomenclature

3P4W	Three-Phase Four-Wire
ADN	Active Distribution Network
ASP	All-Switching-Phase
B2B	Back-to-Back
DEG	Distributed Energy Generation
DER	Distributed Energy Resource
DG	Distributed Generation
DNO	Distribution Network Operator
EGMES	Electricity-Gas Multi-Energy System
GFU	Gas-Fired Unit
LP	Linear Programming
MES	Multi-Energy System
MI-SOCP	Mixed-Integer Second-Order Cone Programming
MOO	Multi-Objective Optimisation
NLP	Nonlinear Programming
NOP	Normal Open Point
OPF	Optimal Power Flow
P2G	Power-to-Gas
PC	Phase-Changing
PCC	Point of Common Coupling
PDE	Partial Differential Equation
PID	Proportional-Integral-Derivation
PR	Proportional Resonant
PR	Proportional-Resonant
PV	Photovoltaic
PWM	Pulse Width Modulation

REG	Renewable Energy Generation
SDP	Semidefinite Programming
SDP	Semidefinite Programming
SOP	Soft Open Point
VI	Voltage Imbalance
VUF	Voltage Unbalanced Factor
WSM	Weighted Sum Method

Parameters

c_p, T_{gas}, γ	Natural gas parameters of heating capacity, temperature and isentropic efficiency
α, β	Weights for objectives
$\bar{g}_u$	Upper limit of the gas supply
Δt	Time interval
Δx_l	Spatial interval
$\emptyset^{P2G}$	Energy conversion factor of natural gas and electric power
η^{P2G}	Energy efficiency of P2G
ω_c	Frequency of the resonance bandwidth
$\overline{\theta}_{boost}$	Maximum limit for the pressure of boost in the compressor
ρ_L, ρ_V	Weight indexes of the power loss objective and the voltage imbalance condition objective
$\theta_{\varphi,i}^{DG}$	Power factor angle of DG on phase φ at node i
$\theta_{i,t}^{P2G}$	Power factor of P2G
$\underline{E^{ES}}$, $\overline{E^{ES}}$	Lower/upper limit of the stored energy in the ES
$\underline{U}$, $\overline{U}$	Lower and upper limits for the node voltage
$\underline{v_i}$, $\overline{v_i}$	Lower and upper limits of voltage at node i
$\underline{pr_m}$, $\overline{pr_m}$	Lower and upper limits of the pressure of gas node
A^{ES}	Power loss coefficient of the ES
A_{SOP}	Power loss coefficient of SOP
$c_{1,l}$, $c_{2,l}$, $c_{3,l}$	Constants of the pipeline l
e_z	Reference voltage of the fourth leg of the VSC
e_{an}, e_{bn}, e_{cn}	reference voltage at the output of the PR controller
e_{an}^*, e_{bn}^*, e_{cn}^*	References of three-phase output voltages for PWM
$f_{Original}^L$, $f_{Original}^V$	Values of f^L and f^V in the original network before optimisation.
$H_{m,n,T}$	Line pack of pipeline mn at the end of the time period

$H_{m,n}^{0}$	Initial line pack of pipeline *mn*
$I_{k,\ rate}$	Rated branch current in feeder #k
i_{oa}^{*}, i_{ob}^{*}, i_{oc}^{*}	References for the output terminal currents of the VSC
k	Resonant gain
k_i	Integral gain of the resonant regulator
k_p	Proportional gain
$k_{m,n}$	Natural gas flow constant of the pipeline from node *m* to node *n*
$P_{\varphi,i}^{DG,ref}$	Given active power generated by DG on phase φ at node *i*
$P_{i,t,s}^{P2G}$, $Q_{i,t,s}^{P2G}$	Active power and reactive power of P2G in node *i* at time *t* of scenario *s*
p_{Max}^{dis}, P_{Min}^{dis}	Maximum and minimum discharge pressure of the compressor
P_{Max}^{suc}, P_{Min}^{suc}	Upper and lower limits for the suction pressure of the compressor
r_a, r_b, r_c	Voltage ratios on phase A, B and C of the step-voltage regulators
r_{ij}, x_{ij}	resistance and impedance of the branch ij
S^{SOP}	Power reference of the SOP
S_{φ}^{SOP}	Power reference on each phase of SOP
S_{i}^{GFU}	Capacity of the GFU at node *i*
S_{i}^{P2G}	Capacity of power input of P2G
$S_{\varphi,i}^{DG}$	capacity of DG installed on phase φat node *i*
$S_{m,n}$	Line pack constant of pipeline *mn*
$S_{SOP}^{Capacity,i}$, $S_{SOP}^{Capacity,j}$	Capacity of the SOP at the node i/j
$S_{SOP}^{Capaciy} \geq 0$	Capacity of SOP
Tap_a, Tap_b, Tap_c	Integers for the phase A, B and C of the step-voltage regulators
v^{φ}	Voltage of phase φ in the optimisation results of various algorithms
v_a^{*}, v_b^{*}, v_c^{*}	Three-phase reference values of the network voltage
$v_{OpenDSS}^{\varphi}$	Voltage of phase φ in the results of OpenDSS
W_L	Weight coefficient of the total power losses
W_U	Weight coefficient of the voltage imbalance condition
W_{Cost}, W_{Wind}, W_C	Weight coefficients of the operational cost F^{Cost}, the curtailment of wind power generation F^{Wind} and the carbon emission F^{C} in objectives
$y_{j,t}$	Nodal shunt capacitance
Z_{ij}	Line impedance of branch ij
z_{re}	Impedance of the voltage regulator
$Error_{v}^{\varphi}$	Voltage error of phase φ

Variables

E_t^{ES}, E_{t+1}^{ES}	Stored energy in the ES at the time $t/t+1$
f^L	Total power losses of ADN
f^V	Voltage imbalance condition of ADN
$f_{l,t,1,s}^{gas}$, $f_{l,t,s}^{in}$	Input flow at the spatial point k of the pipeline l in time t of scenario s
$f_{l,t,k,s}^{gas}$	Flow at the spatial point k of the pipeline l in time t of scenario s
$f_{l,t,N_x,s}^{gas}$, $f_{l,t,s}^{out}$	Output flow at the spatial point k of the pipeline l in time t of scenario s
$f_{l,t,s}^{comp}$	Gas flow through the compressor l at time t for scenario s
$f_{l,t,s}^{in}$, $f_{l,t,s}^{out}$	Input/output flow of the compressor l at time t in scenario s
$f_{t,s}^{gas}$	Gas supply at time t in scenario s
$G_{n,t,s}^{P2G}$	Natural gas output of P2G at node n at the time t of scenario s
$G_{n,t}^{P2G}$	Natural gas output of P2G at node n of the natural gas network at the time t
$g_{u,t}$	Natural gas supply of the gas well unit u at the time t
$H_{m,n,t}$, $H_{m,n,(t-1)}$	Stored mass of natural gas (line pack) in pipeline mn at time t and $t-1$
I_{φ}	Actual phase current of the feeder
I_a, I_b, I_c	Actual current on phase a, b and c
i_a, i_b, i_c	Instantaneous output currents of VSCs
I_k	Actual branch current in feeder #k
$I_{ij,t,s}$	Current of branch ij at time t in scenario s
$I_{ij,t}$	Current vector of branch ij at time t
$I_{ij,t}$	Line current vector of branch ij
$I_{ij,t}^a$, $I_{ij,t}^b$, $I_{ij,t}^c$	Currents on phases a, b, and c of branch ij at time t
i_{oa}, i_{ob}, i_{oc}	Instantaneous inductor currents of the VSC
$l_{ij,t}$	Second-order decision variable of the current on branch ij at time t
l_{re}	Second-order variables of current of regulator
$P_t^{ES,Loss}$	Power loss of the ES
P_t^{ES}	Input/output power of the ES
P_t^{grid}	Electric power from the upstream power grid at the time t
$P_{\varphi,i}^{DG}$, $Q_{\varphi,i}^{DG}$	Active/reactive power output of DG on phase φ at node i
$P_{a,i,\,t,s}^{P2G}$, $P_{b,i,\,t,s}^{P2G}$, $P_{c,i,\,t,s}^{P2G}$	Active power of P2G unit in phase a, b, and c of node i at time t of scenario s
$P_{a,i,t,s}^{GFU}$, $P_{b,i,t,s}^{GFU}$, $P_{c,i,t,s}^{GFU}$	Active power output of GFU unit in phase a, b, and c of node i at time t of scenario s

$P^{P2G}_{a,i,t}$, $P^{P2G}_{b,i,t}$, $P^{P2G}_{b,i,t}$	Active power of P2G unit in phase a, b and c of node i at time t
$P^{GFU}_{i,t,s}$, $Q^{GFU}_{i,t,s}$	Active power and reactive power of GFU at node i at time t of scenario s
$P^{GFU}_{i,t}$, $Q^{GFU}_{i,t}$	Active power and reactive power of GFU at node i at time t
$P^{P2G}_{i,t}$, $Q^{P2G}_{i,t}$	Active power and the reactive power of P2G at node i at time t
$P_{ij,t,s}$, $Q_{ij,t,s}$	Active power and reactive power along branch ij at time t in scenario s
$P_{jk,t,s}$, $Q_{jk,t,s}$	Downstream power flows of node j at time t in scenario s
$P^{Avail}_{k,t}$	Available wind power generation of the wind power unit k at the time t
$P^{Wind}_{k,t}$	Actual power output of the wind power unit k at the time t
$P^{gas}_{l,t,1,s}$, $P^{in}_{l,t,s}$	Pressure at the start of the pipeline l in time t of scenario s
$p^{gas}_{l,t,k,s}$	Pressure at the spatial point k of the pipeline l in time t of scenario s
$P^{gas}_{l,t,N_x,s}$, $P^{out}_{l,t,s}$	Pressure at the end of the pipeline l in time t of scenario s
$P^{comp}_{l,t,s}$	Power consumption of the compressor l at time t for scenario s
$p^{suc}_{l,t,s}$, $p^{dis}_{l,t,s}$, $\Delta p^{comp}_{l,t,s}$	Pressure of suction, discharge and boost in the compressor l at time t for scenario s
$P^{\varphi,i,t}_{SOP,Loss}$, $P^{\varphi,j,t}_{SOP,Loss}$	Power loss of SOP on phase φ of node i/j at the time t
$P^{Loss}_{SOP,t}$	Total power losses of SOPs
$P^{\varphi,i,t}_{SOP}$, $P^{\varphi,j,t}_{SOP}$	Active power injections by the SOP on phase φ of node i/j at the time t
$P^{grid}_{t,s}$	Electricity injection from the upstream power grid at time t in scenario s
$P^{Avail}_{t,s}$	Available wind power generation at time t in scenario s
$P^{Wind}_{t,s}$	Real-time wind power output at time t in scenario s
$Q_{m,n,t}$	Natural gas flow in pipeline mn at time t
$Q^{in}_{m,u,t}$	Inflow natural gas flow of pipeline mn at time t
$Q^{out}_{m,u,t}$	Outflow natural gas flow of pipeline mn at time t
$Q^{\varphi,i,t}_{SOP}$, $Q^{\varphi,j,t}_{SOP}$	Reactive power injections by SOP on phase φ of node i/j at the time t
S_1, S_2	Complex power injection of the feeder #1 and #2 from the PCC before the SOP operation
S^{New}_1, S^{New}_2	Complex power injection of the feeder #1 and #2 from the PCC after the SOP operation
S^{P2G}_i	Power capacity of P2G in node i
$S^{New}_{2,\varphi}$	Complex power injection on phase φ of feeder #2 after the SOP operation
$S_{2,Max}$, $S_{2,Min}$	Maximum and minimum values of the complex power injection from PCC among the three phases of feeder #2 before the operation of SOP
$S_{2,Median}$	complex power injection on the phases of feeder #2 beside $S_{2,Max}$ and $S_{2,Min}$

$S_{ij,t}$	Second-order decision variable of power from node i to node j at time t
$s_{j,t}$	Nodal injection at node j at time t
$S_{jk,t}$	Downstream power flows from node j at time t
$S_{l,t,s}$	Link pack of the pipeline l at time t in scenario s
S_{re}	Power flowing through the regulator
$U_{i,t,s}$, $U_{j,t,s}$	Voltage at node i/j at time t in scenario s
v_0	Second-order decision variable at the source node
V_0^{ref}	Nodal voltage vector at the source node
v_a, v_b, v_c	Instantaneous output voltages of the VSC
$V_{i,-}$, $V_{i,+}$	Negative and positive of the voltage on each node
$V_{i,t}$	Voltage vector of node i at time t
$v_{i,t}$	Second-order decision variable of the voltage on node i at time t
$V_{i,t}^{\varphi}$	Voltage on phase φ of node i at time t
$V_{i,t}^a$, $V_{i,t}^b$, $V_{i,t}^c$	Voltages on phase A, B and C of node i at time t
$v_{j,t}$	Second-order decision variable of voltage at node j at time t
$V_{pri,t}^a$, $V_{pri,t}^b$, $V_{pri,t}^c$	voltage on phase A, B and C of the primary side of the step-voltage regulators at time t
v_{pri}^{abc}, v_{sec}^{abc}	Second-order variables of the primary voltage and the second voltage of the regulators
$V_{sec,t}^a$, $V_{sec,t}^b$, $V_{sec,t}^c$	Voltage on phase A, B and C of the secondary side of the step-voltage regulators at time t
$\dot{P}_{l,t}^{comp}$, $\dot{P}_{i,t}^{P2G}$, $\dot{P}_{i,t}^{GFU}$, $\dot{P}_{i,t}^{Wind}$	First-stage variables for the compressors, P2G unit, GFU units, and the wind power generation
$pr_{m,t}$	Pressure of gas node m at time t
$pr_{n,t}$	Pressure of gas node n at time t

Indices and sets

012	Symmetrical components
φ	Phase a, b, and c
abc	Phase components
H	Hermitian transpose
L_c	Set of all natural gas network compressors
L_p	Set of all natural gas network pipelines
S	Set of all scenarios
T	set of time points
X	Set of equal spatial points of pipelines

Chapter 1

Introduction

1.1 Research Background & Motivations

The UK's commitment to achieving net-zero carbon emissions by 2050 is a pioneering step in acting for tackling global climate change [1] [2]. Stemming from the Climate Change Act of 2008, this target was bolstered in 2019 when the UK became the first major economy to legally commit to such an ambitious goal. As shown in Table 1.1, the Net Zero 2050 plan encompasses a vast range of strategies, including phasing out coal-fired power plants, amplifying the deployment of renewable energy generation (REG), enhancing energy efficiency in homes and industries, investing in carbon capture, usage and storage technologies, and promoting green transportation [3, 4]. This comprehensive approach necessitates innovations and paradigm shifts across multiple sectors of the economy [5].

In the context of the Net Zero 2050 plan, illustrated in Table 1.2, the electric power distribution network plays an important role in the application of low-carbon technologies, including the implementation of electrified heating solutions, the charging infrastructure for electric vehicles, and the installation of distributed REG [6–8]. Therefore, the distribution networks will be the key area of technology applications of distributed low-carbon technologies.

Table 1.1: Key Goals of UK Net Zero 2050 Plan

Sector	**Goal Description** [4]
Overall Emission Reduction	Achieve net-zero greenhouse gas emissions by 2050.
Power System	Fully Decarbonise the UK's power system by 2035. Focus on renewable energy sources.
Transport	Increase the use of electric vehicles. Phase out the sale of new petrol and diesel cars by 2035. Decarbonise public transport systems.
Buildings	Improve energy efficiency. Promote low-carbon heating systems. Phase out gas boilers in new homes by 2025.
Industry	Support the transition to cleaner industrial processes. Introduce carbon pricing. Invest in carbon capture, usage, and storage (CCUS).

Table 1.2: Goals of Power Sector in UK Net Zero 2050 Strategy

Aspect	**Details** [9]
Decarbonisation Target	Fully decarbonize the UK's power system by 2035.
Renewable Energy	Major expansion in renewable energy sources, particularly offshore wind and solar power.
Nuclear Energy	Increase in nuclear energy capacity to reduce reliance on fossil fuels. Plan for new nuclear power stations and small modular reactors.
Carbon Capture & Storage	Investment in carbon capture and storage technologies to reduce emissions from the remaining fossil fuel power plants.
Hydrogen Power	Development of hydrogen energy as a clean alternative, particularly for balancing and storage in the power grid.
Phasing Out Fossil Fuels	Phasing out coal-fired power generation by 2024. Complete phase-out of unabated natural gas for electricity generation by 2035.
Energy Storage & Flexibility	Development of energy storage solutions and flexible energy systems to manage the variability of renewable energy.
Grid Infrastructure	Upgrading and modernising grid infrastructure to accommodate higher shares of renewable energy and new technologies.
Policy & Regulation	Implementing policy and regulatory reforms to support the transition to a decarbonised power system and stimulate investment.

Traditional distribution networks, often inherently passive, were primarily designed to facilitate a unidirectional flow of electricity, typically from the substations to electric loads. However, with the proliferation of distributed energy resources (DERs), including photovoltaic (PV) and wind power generation, flexible loads and energy storage, a more dynamic and adaptive system has appeared. This gave rise to technologies to achieve the active distribution network (ADN) [10,11]. Here ADN represents an evolved grid infrastructure, equipped with a combined capability of local generation, flexible power distribution, and energy storage equipment installed close to the consumers, allowing for a two-way flow of electricity [12]. Under such circumstances, the operational optimisation of ADN can not only maximise the grid performance of power flows but also enhance overall grid flexibility and efficiency.

Central to the flexibility and efficiency of reconfigurating the topologies of ADNs is the Soft Open Point (SOP) [13, 14]. The SOP usually consisting of fast-adjustable and controllable power electronic-based converters, can be applied to replace the normal open points (NOPs) [15], which are the traditional backup connection points between feeders of distribution networks. Unlike the conventional NOP, which can only offer a binary operation of either opening or closing power flow paths, an SOP can regulate and redirect power flows accurately and rapidly [16, 17]. This dynamic control helps in mitigating potential grid constraints, alleviating voltage issues, and optimising the integration of REG into the network. By providing the power exchange between connected feeders, SOP plays a pivotal role in enhancing the reliability, adaptability, and flexibility of ADNs [18]. Therefore, research on the SOP device and the SOP-based optimisation for the optimal operation of ADN is essential.

To further utilise all clean distributed energy resources (DERs), research on electricity systems cannot be isolated from other energy vectors [19]. The interaction among different energy vectors, including (but not limited to) electricity, natural gas, heating, cooling, and hydrogen, can contribute to optimising the overall energy efficiency, achieved by utilising or storing surplus energy from one vector in another [20, 21]. For instance, the excess heat, produced during electricity generation, can utilised by a combined heat and power plant. Similarly, the surplus power generated by DERs, which may not be easily stored within the electric power system, can be converted and stored in other forms, including heating, cooling, natural gas, and hydrogen.

Under this context, the multi-energy system (MES) is a holistic approach to energy management that synergistically integrates various energy vectors, including electrical, thermal, and gas systems, into a cohesive, unified framework [22]. Unlike traditional energy systems that operate in isolation, MES embraces the interdependencies and interactions between different energy vectors, enabling optimised and flexible energy conversion, storage, and distribution. By leveraging the strengths of different energy vectors and mitigating their individual limitations, MES provides a more adaptive energy solution to enhance overall system efficiency, reduce operational costs, and bolster resilience against energy supply disruptions [23]. In an electricity and natural gas MES [24], the Power-to-Gas (P2G) technology plays an instrumental role in facilitating the accommodation of wind power generation [25]. The P2G can convert excess electricity generated from wind turbines into hydrogen through the process of electrolysis. This hydrogen can then be either stored directly or further converted into synthetic methane, allowing it to be injected into the natural gas grid [26, 27]. The energy efficiency of converting electricity into hydrogen, through electrolysis, is about 60% to 80%. If the hydrogen is further converted into methane, the efficiency of methanation is around 70% to 80% [28]. This gas can then be used to generate electricity via gas turbines with energy efficiency ranging from 40% to 50%. Although the round-trip energy efficiency between electricity and natural gas usually be lower than the battery energy storage, by acting as a bridge between the electricity and natural gas systems, P2G can create an integrated energy storage mechanism, enabling a smoother, more efficient accommodation of wind power generation in the MES. Thus, the research on the operational optimisation of MES with P2G unit is pivotal, as MES can contribute to greatly reducing the curtailment of wind power generation.

1.2 Research Aim and Objectives

Utilising the MES as the key solution, this PhD research aims to investigate the impact of SOPs on improving the operation of ADNs and the role of MES, consisting of ADN and the natural gas network, in facilitating the integration of REG. The research focuses of this thesis is shown in Fig 1.1.

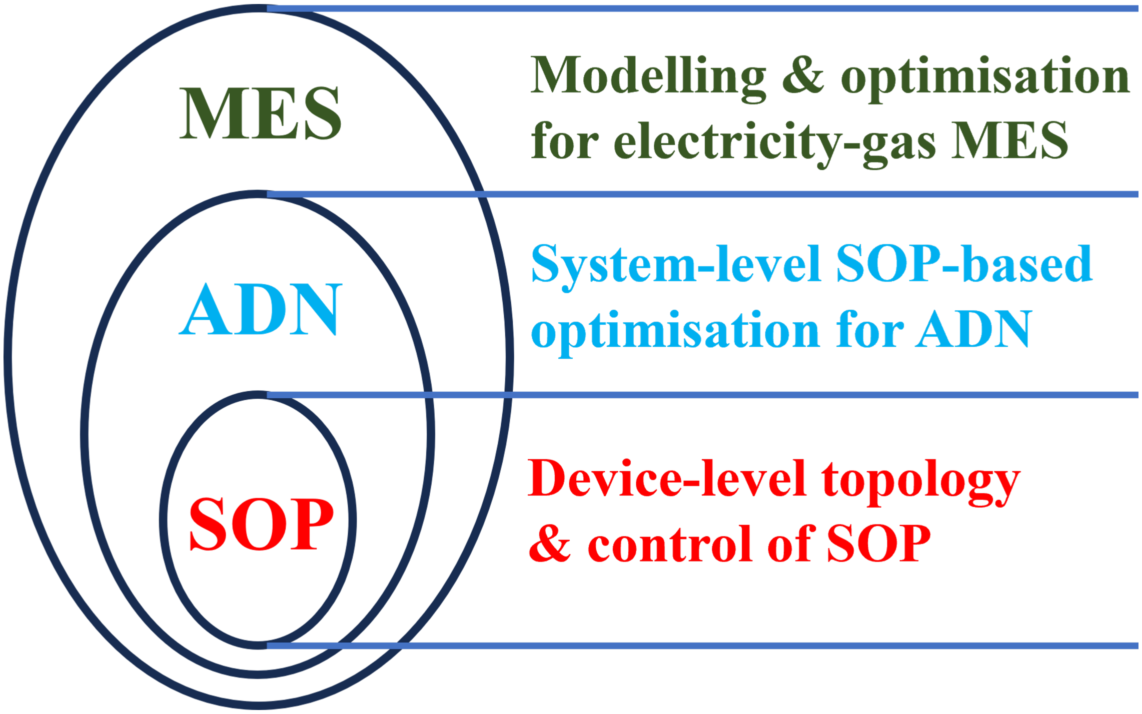

Figure 1.1: The research Focuses of the Thesis

In this thesis, the first objective is to enhance the technology of SOPs in the field of topology, control and strategy for enhancing the operational efficiency of ADNs. The focus is on how SOPs can make the operational efficiency of ADNs better and serve as a cost-effective alternative to traditional network reinforcement, including the upgrading of transformers and power lines, as well as the reconfiguration of networks with passive switches. The study investigates the potential of SOPs to serve as a cost-efficient substitute for conventional network reinforcement methods, typically including the upgrading of transformers and power lines, as well as the reconfiguration of networks using passive switching mechanisms. It is acknowledged that the aforementioned traditional network reinforcement strategies are not mutually exclusive with the implementation of SOPs.

Furthermore, the study seeks to augment the decision-making capabilities of distribution network operators (DNOs), who are tasked with the management of large-scale distribution networks with the deployment of SOPs. Therefore, a comparative analysis of various SOP types and their performance in optimising ADN operations will be conducted. The research aims to elucidate the methodologies through which the SOPs can be more effectively integrated into ADN operations, thereby providing DNOs with innovative strategies to overcome operational challenges, such as power losses and three-phase imbalances. Hence, a new SOP-based optimisation for ADNs will be proposed.

Then, this thesis extends beyond the optimisation of ADNs to a comprehensive exploration of MES, which represents a paradigm shift in energy system integration and management. The foremost objective is to delve into the capacity of MES in the accommodation of REG. By investigating the extent to which MES can enhance the accommodation of REG beyond the capabilities of isolated ADNs, the research will elucidate the transformative potential of MES in the energy landscape. The key to the research is to design the strategic operation of coordination between the electricity and natural gas networks within the MES. In pursuit of this, the study will craft a coordinated operation optimisation model specifically for MES, which is designed to leverage the interaction of energy vectors. This model will be pivotal in managing and improving the efficiency of MES operations, and it is anticipated to lay the foundations for a more resilient and sustainable energy infrastructure. Furthermore, building upon the SOP proposed in the early chapter of this thesis, a thorough analysis will be conducted to unearth the operational performance and the multifaceted benefits brought by SOPs. This investigation will not only focus on the enhancement of operational efficiency within ADNs (e.g., three-phase imbalance) but will also extend to appraising the SOP's contribution to elevating the overall systemic efficiency of the MES. By dissecting the interplay between SOP operation and MES efficiency, the research aims to uncover novel insights that could substantiate the SOP's role as a pivotal component in a path towards a more sustainable and efficient energy future.

1.3 Contributions of the Thesis

Under the research context mentioned in Sections 1.1 and 1.2, focusing on the research objects of SOP, ADN and MES, the contributions of this thesis are summarised as follows:

- For the SOP, the three-phase four-wire (3P4W) back-to-back (B2B) voltage-source converter (VSC) topology has not been fully explored for the topology of SOPs. In this research, the potential of the 3P4W B2B VSC as the topology of SOPs will be explored. Based on the application of the topology, the new control scheme, named the all-switching-phase (ASP) control, is developed for the all-switching-phase SOP (ASP-SOP). Also, based on the ASP-SOP, the new control strategy is designed to mitigate (1) the issue of load imbalance between feeders and (2) the phase imbalance in the heavily loaded feeders.

- For the ADN, an optimal operation strategy based on proposed ASP-SOPs is designed for unbalanced ADNs, with the aims of power loss reduction and voltage imbalance mitigation. For the first time, in the SOP-based optimisation, the symmetrical semidefinite programming (SDP) method is applied to convert the original non-convex nonlinear model into an SDP model, to be efficiently solved.

- For the MES, because of oversimplification, the current modelling finds difficulties in the simultaneous analysis of the states of both the power system and the natural gas network. In this research, aiming to minimise the operational costs, the curtailment of REG and the emission of carbon, a holistic operational coordination optimisation approach is proposed for electricity-gas MES. A comprehensive model is built: the phase imbalance of the electricity distribution system and the line pack dynamics of the natural gas pipelines are considered simultaneously.

- To better enable the direct modelling and solving of nonlinear constraints and to tackle the stochastic challenges in the MES, a graph-based model is developed for directly modelling and solving the nonlinear optimisation problems of stochastic MES and for handling the stochastic issues caused by the REG.

1.4 Organisation of the Thesis

The organisation of this thesis is described as follows:

Chapter 2 - Literature Review

To lay the groundwork for the investigative journey of this thesis, an initial overview of SOPs in ADNs is undertaken. This exploration serves not only to understand the current state of SOP application and research but also to pinpoint the specific research gaps yet to be fully explored within this realm. Following this, the focus shifts to a detailed examination of the current research regarding MES, with particular emphasis on identifying the research gaps in the domain of MES. Moreover, the chapter progresses to provide a comprehensive literature review on two optimisation techniques: symmetrical semi-definite programming (symmetrical SDP) and graph-structured modelling.

Chapter 3 - Soft Open Point: Topology, All-Switching-Phase Control, Strategy

This chapter sets the groundwork for the research at the device level of the flexible power electronics device, focusing on the novel topology, control, and strategy of the SOP. Specifically, the 3P4W-B2B-VSC is introduced as the topology for the SOPs. Building upon this, a ASP control is proposed, culminating in the new ASP-SOP. The strategy is designed to address the issues: (1) load imbalances between feeders and (2) three-phase imbalances in heavily loaded ADN feeders. The simulation results demonstrate the practicability of the 3P4W-B2B-VSC based ASP-SOP and the effectiveness of the all-switching-phase control in achieving load balancing and phase imbalance compensation.

Chapter 4 - Operational Optimisation of Active Distribution Networks based on All-Switching-Phase Soft Open Points

In this chapter, the potential of ASP-SOP in the system-level operational optimisation of ANDs is explored. Based on the ASP-SOPs developed in Chapter 3, an optimal operation strategy is proposed for unbalanced ADNs, with the aims of power loss reduction and voltage imbalance mitigation. Also, the different types of ASP-SOPs are modelled and compared. Furthermore, in the area of SOP-based optimisation, the symmetrical SDP method is, for the first time, applied to convert the original non-convex nonlinear model into a solvable symmetrical SDP model. The outcomes of the case studies indicate that in the proposed optimisation strategy, the new ASP-SOP based on 3P4W-B2B-VSC can lead to a significant reduction of power losses and mitigation of voltage imbalance conditions.

Chapter 5 - Multi-Energy System: Operational Coordination of Active Distribution Networks with All-Switching-Phase Soft Open Points and Natural Gas Networks Considering Power-to-Gas

In this chapter, the application of the symmetrical SDP method based optimisation, applied to ADNs in Chapter 4, is extended to the MES consisting of the ADN as an electric vector and the natural gas network. In the MES, the bi-directional energy flows are implemented through P2G units and gas-fired power plants. The three-phase power distribution system is modelled to fully consider the unbalanced operational network. The natural gas network is incorporated with steady-state gas flows and the dynamic link pack of pipelines. Additionally, the impact of the ASP-SOP for the MES is investigated. Case studies demonstrate the effectiveness of the proposed method in simultaneously minimising the total operational cost, the curtailment of the installed REG, the voltage imbalance of the three-phase power system and the overall carbon emissions.

Chapter 6 - Graph-Structured Two-Stage Stochastic Parallel Nonlinear Optimisation for Multi-Energy System

Although the MES's effects have been highlighted in Chapter 5, the inherent nonlinearity and strong coupling may cause challenges in the modelling of MES; the randomness and volatility of stochastic REG may cause uncertainties in the operation of MES. To handle these challenges, a graph-structured two-stage stochastic nonlinear optimal operation model is proposed for the MES. The first stage ensures consistent equipment performance across all scenarios. The second stage focuses on the MES states. Using parallel evaluations and decomposition, the model consolidates the optimisation into an abstract objective: ’Opti-Graph’, comprising ’Opti-Nodes’ (variables, constraints, objectives, and data) and ’Opti-Edges’ (connections between Opti-Nodes). The case studies showed that our proposed method can reduce operational costs, the curtailment of REG, and carbon emissions while maintaining the integrity of the nonlinearity of the model.

Chapter 7 - Conclusions and Future Work

The main research findings and relevant conclusions are elaborated, followed by subsequent potential research innovation points for future research.

Chapter 2

Literature Review

2.1 Active Distribution Network with Soft Open Point

2.1.1 Active Distribution Networks

The ADNs represent a transformative evolution in the field of power distribution, emerging in response to the limitations of traditional distribution networks and the changing dynamics of energy generation and consumption [29]. Traditional distribution networks, originally designed for a unidirectional flow of electricity from centralised power stations to consumers, have shown considerable drawbacks in the face of modern energy demands [30, 31]. These networks are characterised by

- Limited flexibility, especially in integrating distributed energy resources (DERs) like solar PV and wind power.
- Inefficiencies and reliability issues, primarily due to their inability to dynamically adjust to changing load demands.

- Struggling to cope with increasing electricity demand and technological advancements without significant infrastructure upgrades [32].

Traditional distribution networks often struggle to mitigate or resolve these challenges, particularly when considering the contemporary requirement of low-carbon economic principles. To tackle these issues more effectively, during the 18th International Conference on Electricity Distribution (CIRED), the idea of ADNs was introduced [33].

As defined by the International Council on Large Electric Systems C6.11 working group [34], an ADN is a public distribution network that operates with a flexible structure. It incorporates active management of DER, integrates energy storage solutions, and employs bidirectional approaches to customer demand management. ADNs play a crucial role in the broader public distribution networks managed by electricity distribution companies and distribution network operators. ADNs encompass various functions such as management of DERs, power factor correction, automatic adjustments of on-load tap changers, network reconfiguration, and flexible load management [35].

Differing significantly from traditional networks, ADNs are characterised by the following main aspects [36, 37].

- Integration of various DERs, like wind, solar, and hydro, along with energy storage systems. These resources can be transformed between the Alternating Current (AC) system or the Direct Current (DC) system using power electronic devices and connected to the main grid through power transformers [38].
- Designed for bi-directional energy flows, allowing not just for the distribution of power electricity but also for its reception from DERs. This bi-directional flow is fundamental

in integrating and utilising energy from diverse distributed sources [39].

- The information and communication technology (ICT) and the automation devices are installed and implemented for the operational optimisation of the whole system network [40].
- Installation of smart metres on the customer side. These metres enable the real-time collection of data and information, which can facilitate bidirectional operational control between customers and distribution network/system operators.

However, during this transition of ADNs, the significant intermittence and potential instability of DERs can have negative impacts on the operations of ADNs, with increased complexity and hence challenges.

One challenge is the phase imbalance existing at a mass scale. For example, in the UK's power distribution networks, above 50% of substations see over 50% difference in phase peak currents [41].

In traditional power distribution networks, the phase imbalance primarily arises from two factors: asymmetrical characteristics of power lines or cables, and uneven distribution of power loads across three phases [42,43]. This imbalance can be attributed to varying line impedance, differing electrical distances from the source to the load, and a non-uniform allocation of single-phase loads among the three-phase system [44].

With the evolution towards ADNs, the dynamics of phase imbalance have become more complex. In ADNs, the increasing integration of single-phase DERs, such as solar panels, and single-phase loads like electric vehicles (EVs) and heat pumps, introduces new challenges and opportunities [45, 46]. Whilst these technologies offer potential for system optimisation and enhanced network flexibility, they can also exacerbate phase imbalances, threatening the stability and security of the distribution network.

The negative impacts of phase imbalance are multifaceted and significant [47,48]:

- Additional network investment costs: Phase imbalance leads to inefficient utilisation of network assets. This inefficiency necessitates additional infrastructure to handle the imbalanced load, thereby increasing capital expenditure [49].
- Extra energy losses: Imbalances in the phase load can result in higher power losses in the distribution lines. This not only reduces the overall efficiency of the power distribution system but also translates into higher operational costs.
- Nuisance tripping: Protection systems in electrical networks are sensitive to imbalances. Frequent phase imbalances can cause protective devices to trip unnecessarily, leading to reliability issues and service interruptions.
- Damages to induction motors: Induction motors, widely used in industrial and commercial applications, are particularly susceptible to phase imbalance. Even a small imbalance can cause motor overheating and reduce the lifespan of these motors.

Meanwhile, power losses are an inevitable consequence of electricity transmission and distribution across any network assets. These losses represent a significant inefficiency in the energy supply chain and have wider implications. Over 80% of the total power losses in electric networks occur at the distribution level, especially a critical concern amidst the growing penetration of DERs [50]. The presence of these DERs often results in reverse currents in radial distribution networks, exacerbating power loss challenges. Furthermore, power losses in distribution networks contribute to over 1.5% of the UK's greenhouse gas emissions [51].

The environmental impact of these losses is significant, as they contribute to climate change and reduce the overall efficiency of DERs integrated into the network.

The impacts of power losses have extended significantly to distribution network operators (DNOs) and electricity customers [51]. For DNOs, these losses represent a major operational challenge, as they must balance the efficiency of the distribution network with the increasing demand and integration of diverse energy sources. The financial burden of power losses often leads to increased operational costs for DNOs, which can, in turn, be passed onto consumers in the form of higher electricity tariffs. This creates a direct economic impact on electricity customers, who bear the cost of inefficiencies in the distribution network. Therefore, at the level of the power distribution network, both the DNOs and electricity customers must consider power losses to reduce power costs and further carbon emissions.

Consequently, the research of this thesis focuses on the operational optimisation of ADN, aiming to mitigate phase imbalance while concurrently minimising power losses. This approach is pivotal in enhancing the efficiency and reliability of these networks.

2.1.2 Soft Open Points

In traditional ADNs operating on a radial basis, backup connection points between feeders, commonly referred to as Normally Open Points (NOPs), are characterised by remotely operated switch disconnects [52]. Nowadays, these NOPs are gradually superseded by an innovative concept termed Soft Open Points (SOPs), which are integrated with swiftly controllable power electronic (PE) converters. The SOP, diversely known in academic literature as soft multi-state open point (SMOP) [53], loop balance controller (LBC) [54], and soft normally-open point 'SNOP' [15,55], presents a transformative approach in the realm of ADNs.

The advent of SOP technology combines the inherent simplicity of protection systems in radial ADNs with the superior reliability characteristic of meshed ANDs. Importantly, SOPs achieve this advantage without necessitating any substantive alterations to the prevailing radial layout of ADNs.

SOPs primarily aim to achieve load balancing between connected feeders and expedite the process of supply restoration (SR) in the aftermath of a fault within unaffected sections of the feeders [56]. SR refers to the rapid re-energizing of parts of the feeder that remain operational post-isolation of the faulted segment. SOPs drastically outperform NOPs in SR, operating in mere milliseconds compared to NOPs' slower response of hundreds of milliseconds. SR refers to the prompt reinstatement of power supply to normally operational sections of the feeder after the isolation of the faulted feeders. SOPs demonstrate a remarkable proficiency in SR, executing operational tasks within milliseconds, a significant advancement over the hundreds of milliseconds typically required by NOPs.

SOPs also manifest functionalities akin to other PE devices like the unified power flow controller (UPFC) [57] and the smart transformer (ST). The performance comparison, presented in Table 2.1, shows that the SOP can encapsulate the most functionalities of PE device in ANDs. The advantages of SOPs include [58]:

- Enhanced power flow regulation of active power and reactive power for optimal load balancing.
- Quicker operational response and more accurate control of power flow than NOPs, attributed to the controllable power electronic device rather than the mechanical switch.
- Improved power quality through harmonics and unbalanced current compensation, alongside voltage support capabilities.

- Limitation of fault propagation. SOPs can swiftly disconnect and isolate the faulted feeder within milliseconds to curtail the spread of fault current [59].

Table 2.1: Performance Comparison between SOPs and Other Devices in ADNs

Funtions	**UPFC** [60]	**ST** [61]	**SOP**
Active Power Control	Y	Y	Y
Reactive Power Compensation	Y	Y	Y
Load Balancing	Y	Y	Y
Fault Isolation	N	N	Y
Bidirectional Power Control	N	Y	Y
Installed Location	After transformer	Replacing the transformer	At end of feeders or NOPs
Converter Numbers	Two	One to Three	Two or more
Connected Feeders	One or more	One or more	Two or more

Y for yes; N for no

SOPs are categorised into three types:

- Two-terminal SOP (2T-SOP)
- Multi-terminal SOP (MT-SOP)
- SOP with energy storage (SOP+ES) [62]

The foundational type of SOP, known as the 2T-SOP, typically consists of a pair of back-to-back (B2B) converters [63]. These converters are interconnected in parallel via a common DC-link capacitor. This capacitor serves two functions: firstly, as an energy buffer, and secondly, to mitigate voltage ripples on the DC side, thereby enhancing the stability and efficiency of the system. The 2T-SOP can be further developed into a more sophisticated type of SOP, termed the MT-SOP which can enhance the operational performance of ADNs by interconnecting three or more feeders. The MT-SOP is engineered to connect vulnerable feeders which are particularly susceptible to instabilities, primarily because of the extensive integration of DERs and substantial power load demands [64]. This design aims to achieve load balancing within the connected feeders.

The SOP+ES, in which Energy Storage (ES) is coupled to the DC side of the SOP via a DC-DC converter, centralises ES at a strategic location, as opposed to a more dispersed arrangement throughout the ADN [65]. Such centralisation can offer potential cost efficiencies, especially as the ES becomes increasingly essential in modern ADNs due to the intermittent nature of integrated DERs [62]. In the SOP+ES, the DC-link voltage is regulated by the DC-DC converter. Concurrently, the AC/DC converters, connected to the feeders, play a pivotal role in managing the charging and discharging power of the ES, enabling it to effectively adapt to fluctuating energy demands and storage requirements [66].

In this research, the 2T-SOP and the 2T-SOP+ES will be taken into consideration for the optimal operation of the ADNs.

Topology of Soft Open Points

Various converter topologies are available for deployment in SOPs, particularly in the context of 2T-SOP configurations, which necessitate bidirectional power flow control capabilities. Among these, the two-level voltage source converter (VSC) [56] is extensively utilised for SOP applications, and the Modular Multilevel Converter (MMC) [67] is also considered due to its lower switching losses and high-voltage quality attributes. Further, configurations such as B2B Modular Multilevel Matrix Converter (M3C) [68], Unified Power Flow Controller (UPFC) configuration [69, 70], Cascaded H-bridge (CHB), and Multi-Active Bridge (MAB) converters [71] have been examined in academic literature. The topologies of SOPs are summarised in Table 2.2.

In previous studies of the B2B VSC based SOP, the two-level three-phase three-wire (3P3W) VSC has been the predominantly used topology [56]. The fundamental principle of the 3P3W

Table 2.2: Topologies of SOPs

Converter Topology	References
VSC	[56] Most widely used
MMC	[67]
M^3C	[68]
Electric Spring	[70]
CHB, MAB	[71]
UPFC Configurated SOP	[69, 70]

VSC involves using two levels of voltage, either positive or negative, to effectively convert and control the AC power in a three-phase power system. This topology is favoured for its relative simplicity and efficiency in handling power conversion tasks [59]. However, in the circumstances of ADNs, the existence of the neutral lines introduces the potential for decoupling the three phases, meaning that the neutral line current of the feeder can be independently regulated, offering a significant advantage in managing power flows and enhancing stability [72] [73]. This capability becomes particularly crucial in the unbalanced networks, which are commonplace in ADNs.

The three-phase four-wire (3P4W) VSC consists of six semiconductor switches, typically IGBTs (Insulated Gate Bipolar Transistors) or MOSFETs (Metal-Oxide-Semiconductor Field-Effect Transistors), arranged in a bridge configuration. Each phase of the converter has two switches that are controlled to convert DC power into AC power. The fourth wire, or the neutral wire, is used to manage the zero-sequence current, especially in unbalanced load conditions. This is crucial in applications where the power of the three phases is not equal [74].

Recognising this, the 3P4W VSCs have been identified as a more suitable topology for applications in such unbalanced systems [75]. Their ability, including handling the neutral line and compensating for unbalanced voltage, allows for improved performance in both grid-connected and stand-alone operations [76, 77]. Nevertheless, despite the apparent advantages of the 3P4W VSCs, their application in B2B VSC based soft open points (SOPs) has not been fully explored. In the research of this thesis, 3P4W-B2B-VSCs will be used as the topology of SOPs to achieve better control performance, especially under the circumstances of unbalanced ADNs.

Control of Soft Open Points

For the conventional SOPs of the B2B-VSC, a dual closed-loop current-controlled mode is applied to control the active and reactive power flows through the SOP, under the circumstance of the stable network conditions [78]. The control of the two VSCs in the B2B SOP usually comprises three principal components [79, 80]:

- Outer power control loop: one VSC operates with the active/reactive power (P/Q) control, where the errors between the references and actual values of the active and reactive power are transformed into the reference dq current components, while the other VSC operates with the V^{dc}/Q control to maintain the voltage across the DC-link capacitor. These processes generate current references for the subsequent inner current control loop.
- Inner current control loop: The reference VSC dq voltage can be computed using the proportional-integral (PI) controller [81, 82]. This calculation takes into account the dq current discrepancies. To enhance the dynamic response, the voltage feed-forward and current feed-back compensations are incorporated. After the voltage references of the VSC terminal are obtained from the transformation of the reference VSC dq voltage, the gate signals for the power thyristors can be generated by using pulse width modulation (PWM),

- Phase-locked loop (PLL): The PLL plays an important role in synchronising the real-time phase of the VSC output voltage with the AC network voltage by collecting precise information about the AC network, including phase angle, frequency, and the voltage value of positive and negative sequences.

During the period of faults or disturbances in any one of the feeders connected by the terminal of SOP, the SOP terminal connected to the isolated loads operates as a voltage source to provide the requisite voltage and stable frequency to the isolated loads, which is the control mode of SOPs recognised as the supply restoration [83]. Concurrently, another converter, associated with the unfaulty feeders, continues to function as a current source and operate under the V^{dc}/Q control.

To alleviate the imbalance issue of ADNs, the concept of 'phase-changing (PC) SOP (PC-SOP)' has been proposed in [84, 85]. However, in these two papers, the power exchange can only be realised between the specific AC phases of two terminals of PC-SOP, for example: phase A to phase B, phase B to phase C, and phase C to phase A. It is noteworthy that these studies do not delve deeply into the fundamental control scheme of PC-SOP. Moreover, the strategies for optimal operation remain a gap area for further investigation and development.

SOP based ADN operational optimisation

In [86], a two-stage robust SOP based optimization method for ADNs is proposed to handle the uncertainties of PV outputs, aiming to achieve desired voltage and reduced power losses. Through convexification, the model is formulated as a two-stage Second Order Cone Programming (SOCP) problem. By using a MT-SOP, Ref. [64] introduces a optimisation method to alleviate feeder load imbalance and decrease power losses in ADNs. involving transforming the initial non-convex nonlinear model into a tractable SOCP model through convex relaxation and linearization.

In [87], with the increasing penetration levels of single-phase distributed generation (DG), an operation optimization model for unbalanced ADNs is developed based on SOPs to minimize the operational losses and mitigate three-phase unbalances in ADNs. The original nonlinear model is converted into an semidefinite programming (SDP) model via convex relaxation. In [62], the results of case study illustrate that the SOP based optimisation can provide the ADN with the improved accommodation of the PVs, attributed to SOP's precise and swift control over power flow, both spatially and temporally.

In [88], a model considering the long-term operational traits of DG and network topology alterations is established to optimise the placement and sizing of SOPs. The objective is to minimise the annual power loss costs of the distribution system, along with the capital and operational costs of SOPs. Through linearization and conic relaxation techniques, the complex nonconvex mixed integer nonlinear model is converted into a traceable mixed integer SOCP (MISOCP) model to ensure the reach of the global optimality. In [89], the authors developes a mixed-integer non-linear programming (MINLP) model to achieve the optimal planning of the distributed ES in ADN. The installed SOPs is regulated to optimise the flexible active and reactive power control on the connected feeders of ADN. Ref. [90] presents a coordinated optimisation model based on SOP is proposed to achieve the minimum value of the operation costs and to improve the voltage profile in ADNs considering the controllable equipment including the SOP, on-load tap changer and switchable capacitor banks. With the application of MISOCP, the global optimal results can be guaranteed.

In [91], an optimal configuration model of SOP is designed and implemented for ADNs, considering the characteristics of DERs, to minimise the SOP cost of fixed investments and annual operation and the ADN's annual power losses. Then, the MISOCP is deployed to solve the model with efficiency and convergence. During the blackouts in ADN, the SOPs in ANDs are utilised in [92], along with the routing repair teams and the electric vehicles, to realize fast and maximum supply restoration of the high-priority loads. In [93], a bi-level optimisation model is developed to coordinate the allocation and operation of DG, capacitor banks, and SOPs. The upper level focuses on minimizing investment in controllable devices, operational and maintenance costs, and the cost of power purchased for ADNs. The lower level aims to minimize the power loss in ADNs. To solve the bi-level model, a genetic algorithm is applied.

Table 2.3: Comparison of Research on SOP based Optimisation

Reference	**Optimisation Objectives**	**Controllable Device**	**Case Study Network**
[86]	Minimise uncertainties of PVs, power losses and voltage deviations	2T-SOP, PV	IEEE 33-node system
[64]	Minimise feeder's unbalanced condition and total power losses	MT-SOP, DG	IEEE 33-node system
[87]	Minimise total power losses, imbalance of voltage and current	2T-SOP, PV	IEEE 33-, 123-node system
[88]	Minimise the capital and annual operational cost of SOP, and annual cost of power loss in ADN	2T-SOP, PV, Wind power	IEEE 33-node; Taiwan distribution system
[62]	Maximise the hosting capacity of PVs	2T-, MT-, SOP; SOP+ES; PV	IEEE 33-node system
[89]	Minimise the operational cost of ADN and ES investment cost	2T-SOP, Battery ES, PV, Wind power, On-load tap changer	IEEE 33-node system
[90]	Minimise the cost of total power loss and voltage deviation	2T-SOP, On-load tap changer, Capacitor banks	IEEE 33-, 123-node system
[91]	Minimise the fixed investment and annual operation cost of SOP, annual power loss of ADN	2T-SOP, PV, Wind power	IEEE 33-node system
[92]	Maximise the supply restoration of the high-priority loads	2T-SOP, EVs	IEEE 33-, 69- node system
[70]	Mitigate the voltage deviation	2T-SOP	IEEE 15-, 33-, 69 node
[93]	Minimise the investment of controllable devices, the operational and maintenance cost	2T-SOP, PV, Wind power, Capacitor banks	IEEE 33-node system

2.2 Multi-Energy Systems

2.2.1 Multi-Energy System with Power-to-Gas

The penetration of REG has been continuously increasing, to mitigate issues caused by environmental deterioration. Therefore, there is a global trend of transforming the energy sector toward a low-carbon economy. However, one critical bottleneck is that the development of current power grids is lagging behind to fully accommodate abundant REG because of the following characteristics of REG [16, 94–96]:

- Intermittent fluctuations. The inherent variability of REG, such as solar and wind power, results in intermittent fluctuations in energy output. This intermittency, influenced by external factors like meteorological conditions and the time of day, presents a significant challenge for power grids, which are designed to maintain a real-time balance between electricity supply and power demand. The absence of robust energy storage solutions or advanced demand-side management may cause difficulties in integrating high levels of REG, even potentially leading to grid instability and reliability issues.
- ‘Anti’ peak demand effect. This term likely refers to the mismatch between the peak production times of certain REG and the peak demand times of electric power. For example, the wind power generation reaches its highest output in the evening, which may not coincide with the peak power demand during the daytime. This misalignment can result in excessive generation during periods of low demand and insufficient output during periods of high demand, complicating grid management and necessitating additional flexible generation sources or storage to maintain grid stability.
- Causing reverse power flow in power grids. Traditional power grids are predominantly

designed for a unidirectional flow of electricity from centralised substations to end-users. However, when locally distributed REG exceed consumption, the excess energy can be fed back into the superior power grid, reversing the conventional flow direction. This reverse flow poses technical challenges, including the need for voltage regulation, the risk of overloading grid components, and complexities in maintaining power quality.

Therefore, both power network operators and individual customers would benefit from minimising the curtailment of REG.

One of the most promoted solutions is to facilitate this utilisation of the power-to-gas (P2G) units [25, 97, 98]. The P2G involves the use of surplus REG electricity, during periods of low electricity consumption, to produce hydrogen (H_2) via the electrolysis of water. The produced hydrogen can be either directly utilised in various applications, stored for later use, or further processed into methane (CH_4) through a process known as methanation. The methane, named natural gas (NG) can be injected into and stored in the pipelines of the natural gas network.

Compared with other energy storage methods, the P2G has the technological characteristics and advantages in realising large-scale accommodation of REG as follows [28, 99–103]:

- P2G is recognised as a low-carbon technology for two primary reasons. Firstly, by converting surplus REGs into hydrogen or methane, P2G facilitates the storage of excess renewable energy that might otherwise be curtailed due to the limited capacity of the power grid. Secondly, the outputs of P2G are hydrogen and methane. When combusted, hydrogen produces only carbon-free water. Meanwhile, the released CO_2 in methane combustion almost be equivalent to that originally captured from the atmosphere during the methanation process. Admittedly the P2G process requires significant inputs of energy and material, but it still can enhance the integration of REGs and markedly contribute to reducing the carbon emissions of the electricity-gas MES.

- Compared with battery energy storage, P2G has higher storage capacity and energy conversion efficiency. Battery energy storage systems usually have limitations in capacity size because of the high cost. In contrast, P2G allows for the storage of large amounts of hydrogen or synthetic natural gas stored in the existing infrastructure of natural gas, meaning that the utilisation of P2G will not be limited by the storage capacity. Meanwhile, there have been MW-level pilot projects under operation, with an efficiency of 60%–70%, e.g. the Energiepark Mainz, a 6.3MW P2G project in Germany [98]. If the waste heat can be better managed and utilised, the overall system efficiency can be further improved.

- The P2G unit can serve as a flexible controllable power load in the power grid. The power of P2G units can be rapidly ramped up or down depending on the availability of excess REG, resulting in that the P2G can contribute to not only the accommodation of large-scale REG, but also frequency regulation and peak-valley regulation. It has been observed from Hydrogenic's pilot P2G project that the P2G units demonstrate a rapid speed of dynamic response and can satisfy the demands of automatic generation control systems.

- The P2G has strong compatibility with existing infrastructure. Hydrogen, as the primary product of this process, is a premium energy source and has diverse applications in sectors like chemicals, transportation, methanation, and fuel cells. Additionally, this hydrogen can either be directly fed into the existing natural gas pipelines within certain thresholds or be converted into natural gas through methanation and then injected into the pipelines.

With the application of P2G, it is possible to leverage the storage capacity of the natural gas network as the energy storage for the electric power grid to counteract restraints of the power grid that in the power grid, the energy storage is capacity-limited and highly cost, and to facilitate the integration of REG [104].

Therefore, together with the gas-fired power plants (GFPPs), also named gas-fired units (GFUs), which use natural gas as fuel to generate electricity for the electric power grid, P2G units can help to form a closed loop of energy conversion in so-called electricity-natural gas (ENG) multi-energy system (MES) [95, 105–107].

2.2.2 Modelling of Multi-Energy System

Broad interests and efforts have been devoted to exploring the modelling of ENGMESs. Qi et al. [108] proposed an optimal dispatch model for the electricity and natural gas system where bi-directional energy flows are taken into account. To linearise natural gas flow constraints the Wendorff difference form was adopted. In [109], a day-ahead operational optimisation of the decentralised decision-making method is proposed for an integrated electricity and natural gas system with P2G. Yang et al. [110] proposed a distributionally robust chance-constrained model for the optimal power-gas flow problem with varying wind power to adjust the flexible resources in both systems for uncertainty mitigation. Chen et al. [111] proposed a mixed-integer nonlinear unit commitment model with non-convex nonlinear gas flow equations. An enhanced convex relaxation is implemented to make the model tractable while obtaining high-quality solutions. In [112], A combined power, heat, and natural gas dispatch model is established to investigate the network flexibility with the nonconvex flow dynamics of gas accounted in a computationally efficient manner.

However, in the above-mentioned research, the models of either the electric power system or the natural gas network are oversimplified, leading to an incomplete analysis of the comprehensive operational states of both the electric power system and the natural gas network. In [108, 109, 111, 112], although the line pack in pipelines is considered, the power systems are modelled simplistically using lossless ideal DC power flow. This approach results in a lack of analysis concerning the operational conditions of the electric power grid. In [110], voltage limits of the power system are not included in the constraints. Meanwhile, none of the research found in the literature uses a detailed three-phase model of electric power systems in the multi-energy network. Therefore, the need is highlighted in developing a comprehensive model of ENG-MES, consisting of a three-phase unbalanced power system and a natural gas network with the line pack dynamics of the pipelines.

2.2.3 Stochastic Optimisation of Multi-Energy System

Stochastic optimisation plays a pivotal role in ensuring the optimal operation of MES, as the multiple uncertainties, coming from variability or forecast errors of the energy carriers, sources and loads, may make the capture of stochastic scenarios difficult [113, 114]. Some research uses Monte Carlo simulation [115, 116] and Latin Hypercube Sampling (LHS) [117, 118] can be applied to produce the initial stochastic scenarios. In [119], a two-stage optimal operation method is proposed for a community-integrated energy system for the issue of uncertainties. The first stage is designed as a robust optimal operation model, while stochastic scheduling is deployed in the second stage. Ref. [120] established a two-stage stochastic optimisation model for multi-energy microgrids, where the equipment outputs are controlled according to day-ahead forecasts in the first stage, and in the second stage, the energy storage equipment is utilised to respond for fluctuations of scenarios. In [121], the two-stage stochastic optimisation was applied to the design of MES capacity and operation. In the first stage, the design parameters and decision variables are configured by a genetic algorithm. The second stage applies Monte Carlo simulation to fix the uncertainties in multi-energy flow.

However, like the research mentioned above, most stochastic optimisation models rely on the scenario curtailment or forecast, which can be easily influenced by the initial scenario setting and is hard to apply to different types of scenarios.

2.3 Operational Optimisation for Energy System

2.3.1 Convex Optimisation

In the field of convex optimisation, a hierarchical classification, as shown in Fig 2.1, describes the various problem types [122]. At the foundation of this hierarchy is linear programming (LP), which serves as the basis for quadratic programming (QP). Progressing further, QP forms the bedrock for second-order cone Programming (SOCP). In turn, SOCP underpins the framework of semidefinite programming (SDP), which then culminates in convex programming (CP). Every CP reduces to a graph form programming.

This classification not only shows the types of convex optimisation problems but also illustrates a gradation in complexity and generality. As one ascends in the class of this hierarchy, each problem can become more generalised and intricate. For instance, every case of SOCP can be inherently viewed as a case of SDP.

From the perspective of ADN optimisation, Convex optimisation, also named convex optimal

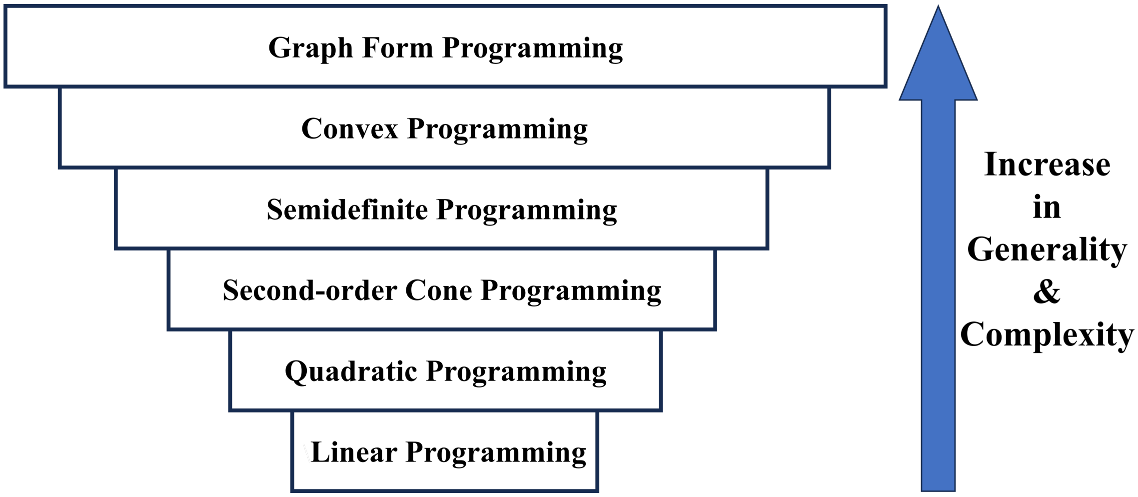

Figure 2.1: Hierarchy of Convex Optimisation Problems

power flow (OPF), includes:

- *DC OPF* [123]: While DC OPF can be instrumental in building economic dispatch and accommodating asset thermal constraints with simplified power flow constraints, DC OPF is usually applied in the optimisation of power transmission systems rather than distribution systems. Because it cannot be used in calculating the elements of power loss, voltage constraint, and reactive power flow, which are essential for the optimisation of distribution systems [124].

- *AC single-phase OPF* [125]: The AC single-phase OPF problem represents a specialised type of the more encompassing AC three-phase OPF problem. Under the circumstances when the three phases are balanced in the power gird, the AC three-phase OPF problem can be effectively reduced to an AC single-phase OPF problem for developing more efficient and effective power flow management strategies in varying electrical network configurations. In [126], the single-phase OPF in power distribution networks was derived as a mixed-integer second-order cone programming (MI-SOCP) by Jabr et al. to achieve the global optimal solution.

- *AC three-phase OPF*: The nonconvex nature of the single-phase OPF problem is markedly less pronounced compared to its three-phase counterpart [127]. In [128], an unbalanced three-phase OPF, based on a quasi-Newton method, was proposed and simulated in OpenDSS for the optimisation of distribution management systems. In [129], the authors proved that a bus-injection SDP (BIM-SDP) model can be utilised to obtain the global optimal solution of the original non-convex OPF problem. In [130], the authors indicated that the branch-flow model SDP (BFM-SDP), as an equivalent physical model, can improve the numerical stability of the BIM-SDP. Meanwhile, the chordal extension of a partial matrix can help to accelerate the solving process. In [131], to enhance numerical stability and accuracy, Wang, et al. substituted the existing BFM-SDP model with a symmetrical SDP model.

However, the symmetrical SDP has not been applied in the SOP-based optimisation of unbalanced ADNs and the operational optimisation of MES.

Convex optimisation is suitably applied in SOP-based optimisations for two reasons.

- The operational constraints of the B2B-VSC-based SOP are convex [15], while it has been proved that the problem of the non-convex OPF, including single-phase OPF and three-phase OPF, can be converted into convex problems [132].
- As the intersection of convex sets is convex, the set of convexed OPF constraints and SOP constraints is still mathematically convex [133].

2.3.2 Graph-Based Nonlinear Optimisation

In [134] and [135], a graph-based abstraction is proposed for the formulation of optimisation models. This framework conceptualises any optimisation model as a hierarchical graph. Within this graph, each level is constituted by a collection of nodes and edges. These nodes encapsulate individual optimisation models, encompassing relevant variables, objectives, constraints, and data. Meanwhile, the edges represent the interconnections (connectivity) between these models in the nodes. A key aspect of the approach is the dual expression of the optimisation models within nodes: they can be articulated either algebraically, like a traditional algebraic modelling language, or as a hierarchical graph. This dualism in expression permits the incorporation of both algebraic and object-oriented modelling paradigms into a singular, cohesive framework.

The characteristics and advantages of the graph-based modelling are summarised as follows [136–141]:

- The graph-based modelling effectively unveils the inherent structure of problems to algorithmic analysis and advocates a modular methodology for model construction, which can enable independent processing of distinct model components (such as automatic differentiation) and enhance data management efficiency.
- The graph-based modelling naturally encapsulates a broad spectrum of optimisation problems, including stochastic optimisation, dynamic optimisation, network optimisation, partial differential equation (PDE) optimisation, and multi-scale optimisation.
- The graph structure possesses the adaptability to automatically interface with decomposition solvers, contributing to the implementation of decomposition strategies, e.g.

Schur decomposition.

- The graph structure is designed to be compatible with graph visualisation tools, resulting in that it can be utilised to visualise the model using tools like Metis or KaHyPar.

Two software packages programmed in Julia, namely Plasmo.jl and MadNLP.jl, are instrumental in applying graph-based models for the tasks of solving the optimisation problem. Generally, Plasmo.jl is initially employed to represent optimisation problems within a graph-based framework. Subsequently, this graph-based model generated by Plasmo.jl is transferred to the solver package, MadNLP.jl.

To construct and solve the graph-based optimisation problems, a Julia-based software tool, Plasmo.jl, is explored to conduct the implementation of the hierarchical graph abstraction [142]. This software framework allows for a direct definition of the problem's structure during the model construction, which is significantly different from the traditional methods that focus on identifying graph structures after the model development. Plasmo.jl can combine all the elements of the optimisation problem, including (but not limited to) variables, constraints, objectives, and data, into an object of the abstract modelling, named Opti-Graph. A typical Opti-Graph usually consists of Opti-Nodes and Opti-Edges. Opti-Nodes hold essential modelling components like variables, constraints, objectives, and data, and Opti-Edges represent the structural connections between these components.

MadNLP.jl, a nonlinear programming (NLP) solver developed in the Julia programming language, was introduced by Shin in [143]. It effectively utilises graph structures modelled by Plasmo.jl through the application of Schwarz decomposition. The comprehensive interface between the modeller and solver, Plasmo.jl and MadNLP.jl, is detailed in [144], which also proves that Schur decomposition offers a flexible and robust decomposition paradigm for solving diverse graph-based structures modelled by Plasmo.jl.

2.4 Conclusion of Literature Review

This literature review above has examined the current research landscape, concentrating on SOPs, ADN, and MES. The research innovations of this thesis can be summarised as follows.

- For the SOP, the 3P4W B2B VSC topology has not been applied to the topology of SOPs. Based on the new application of this topology, the relevant control scheme and the control strategy will be developed to mitigate the issues of load imbalance and phase imbalance.
- For the ADN, based on the modelling of the proposed SOP, an optimal operation strategy will be designed for unbalanced ADNs. For the first time, in the SOP-based optimisation, the symmetrical SDP method is applied for the optimal operation of the unbalanced ADNs.
- For the electricity-gas MES, based on the symmetrical SDP, a comprehensive model will be built with the simultaneous consideration of the phase imbalance in the electricity distribution system and the line pack dynamics in the pipelines of natural gas. Additionally, the impact of the proposed ASP-SOP for the MES will be investigated.
- The graph-based optimisation of Julia framework has not been fully developed in the operational optimisation problem of the MES. To keep the natural characteristics of nonlinear functions or constraints and to handle the stochastic challenge caused by the uncertainty of REG, a graph-based model will be developed for directly modelling and solving the nonlinear optimisation problems of stochastic MES.

Chapter 3

Soft Open Point: Topology, Control and Operational Strategy

3.1 Introduction of SOPs

The SOPs, which can be utilised to regulate power flow between the connected feeders, can be recognised as a solution to both unbalanced situations, as they can realise load balancing between feeders and potentially compensate for unbalanced phase power flows. In this chapter, the three-phase four-wire back-to-back VSC (3P4W-B2B-VSC) is applied as the topology of the SOPs. Based on this, an all-switching-phase (ASP) control is proposed. It is designed to mitigate (1) the issue of load imbalance between feeders and (2) the phase imbalance in the heavily loaded feeder in ADNs.

The major work completed in this chapter are summarised as follows:

- The 3P4W-B2B-VSC is investigated as the new topology of SOPs.
- Based on the new topology, the realistic control theory (e.g., proportional-resonant (PR)

control) is incorporated for the all-switching-phase control scheme for the all-switching-phase SOP (ASP-SOP).

- The control strategy of the ASP-SOPs is designed to realise load balancing between connected feeders and phase imbalance compensation in heavily-loaded feeders.
- The case study through the power electronics simulation in Matlab/Simulink, is conducted to demonstrate the effectiveness and efficiency of the ASP-SOP based on the 3P4W-B2B-VSC.

3.2 Topology of Soft Open Points

Possible SOP topologies include B2B VSCs [68], [145], multi-terminal VSCs, and unified power flow controllers (UPFCs) [146] [59]. The B2B VSC is suitable for SOP operation due to the following characteristics [147].

- It is equipped with flexibility in controlling both the active and reactive power. The VSCs can generate their voltage or current waveforms, allowing complete control over the active power flowing across the DC link and independent reactive power supply or absorption at both feeder terminals.
- It can isolate disturbances and faults. The DC-link capacitor decouples the two AC sides, therefore, the two feeders can be connected asynchronously [56]. Thus, the network disturbances or faults on one connected feeder can be isolated from the other side by VSCs

- The B2B-VSC can supply isolated areas of a network or support a black-start. As VSCs can generate voltages without other sources at the receiving end, a black start could be achieved for supply restoration [71].

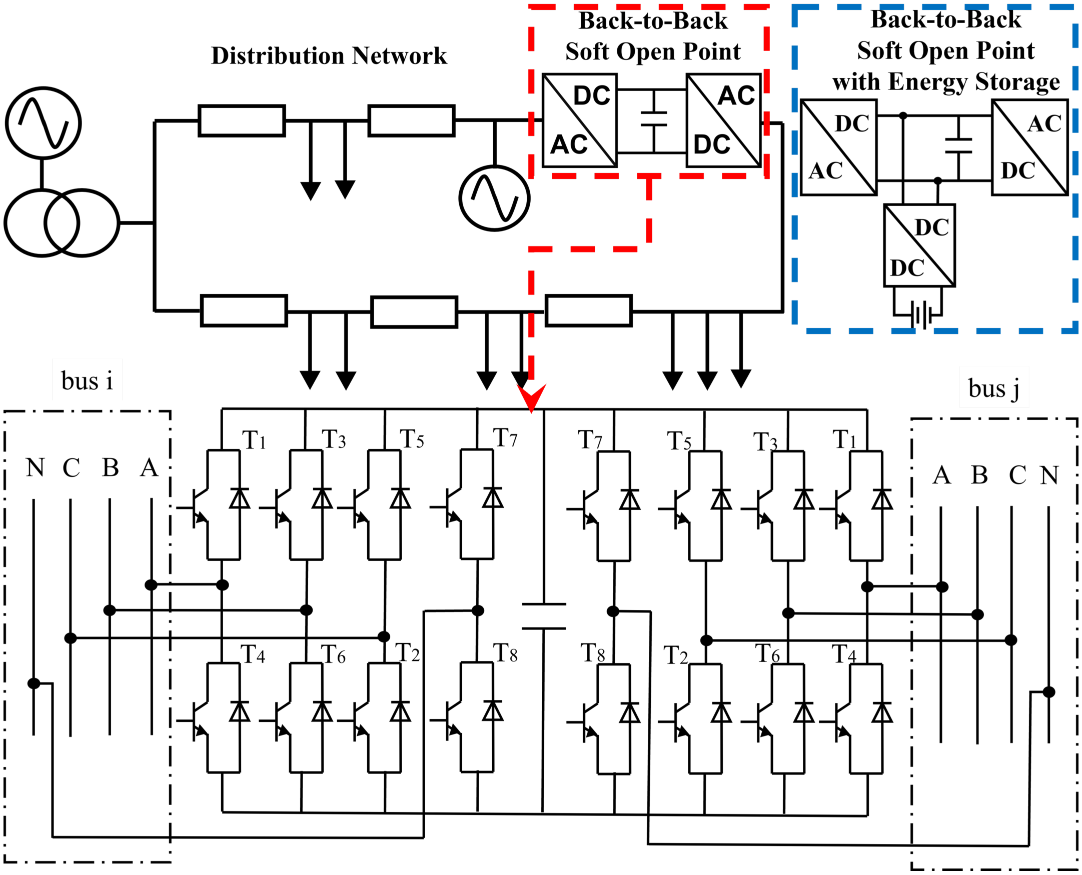

Figure 3.1: Illustration of a B2B-VSC SOP Installed in Distribution Networks

This research selects the 3P4W VSC as the foundational topology for B2B VSC-based SOPs. As depicted in Fig 3.1, the main circuit of the topology encompasses a pair of VSCs located at the endpoints of the AC feeders. These two converters are interconnected via a common DC link. The innovative SOP topology integrates two two-level, 3P4W insulated gate bipolar transistor (IGBT)-based VSCs, which can generate the voltage waveform through pulse width modulation (PWM) and are connected in parallel through a common DC-link capacitor. This capacitor serves a dual purpose: it acts as an energy buffer and reduces voltage ripple on the DC side. The fourth wire of the AC side is created through the connection between the neutral wire of the feeder and the midpoint in the fourth leg of VSCs. To eliminate harmonics of high frequencies in the output current of SOPs, the LC filters are connected at the VSC terminals of AC sides.

This research is predicated on two foundational assumptions essential for the application of the proposed 3P4W B2B VSC-based SOP.

- The electric power grid operates as a three-phase, four-wire system, which inherently includes the presence of a neutral line.
- The NOP, the installation position of SOP, exists within the power grid infrastructure.

3.3 All-Switching-Phase Control

In the traditional SOPs, the terminals are usually under the control of either Vdc/Q or P/Q, which are all realised through the proportional-integral-derivation (PID) regulators in the dq0 frame [148]. As a result, all three phases, at one terminal of either the input or output terminal, always have the same active/reactive power.

Different from the traditional SOPs, the new ASP-SOPs have the feature that the current/power of each phase of the terminal can be regulated independently, meaning that power flows from one AC side can be separately distributed at three different values to each phase of the other AC side [149].

To realise the ASP control, a scalar proportional-resonant (PR) controller, as shown in Fig 3.2, is applied to regulate the 3P4W VSCs. The PR controller comprises a voltage control loop to control the output voltages and a current control loop to provide the PWM with the reference signals. The transfer function of the PR controller is defined in (3.1) [147].

$$G_{PR}(s) = k_p + \frac{2k_i\omega_c s}{s^2 + 2\omega_c s + \omega_n^2} \tag{3.1}$$

where k_p is the proportional gain and k_i is the integral gain of the resonant regulator; ω_n is the angular frequency of the output (100 π rad/s for 50Hz); ω_c is the frequency of the resonance bandwidth.

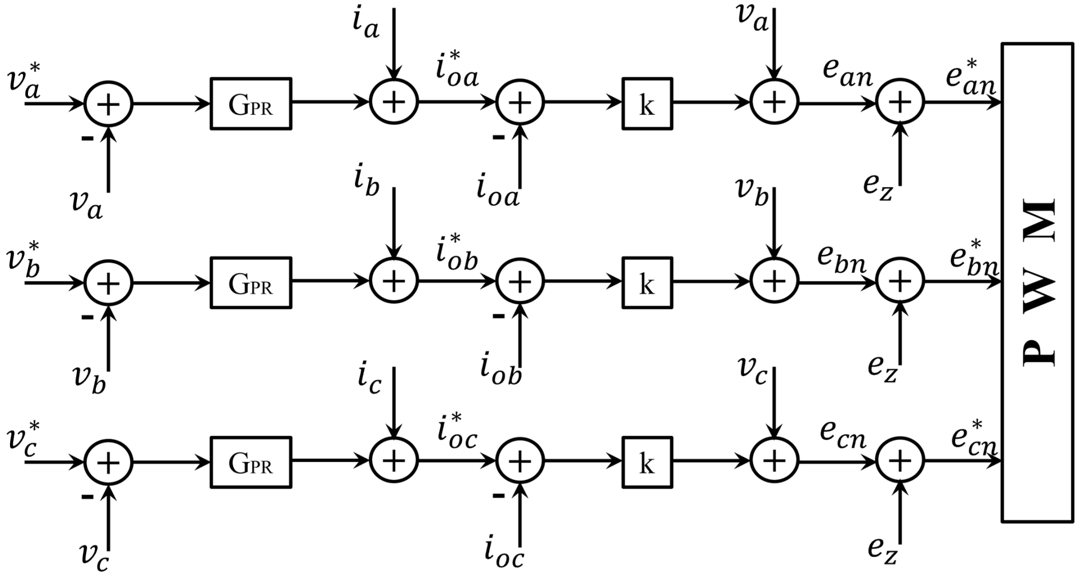

Figure 3.2: Control Diagram of the PR Controller

The voltage control loop can be described as below.

$$\begin{bmatrix} i_{oa}^* \\ i_{ob}^* \\ i_{oc}^* \end{bmatrix} = \begin{bmatrix} i_a \\ i_b \\ i_c \end{bmatrix} + G_{PR}(s) \begin{bmatrix} v_a^* - v_a \\ v_b^* - v_b \\ v_c^* - v_c \end{bmatrix} \tag{3.2}$$

where v_a^*, v_b^* and v_c^* are the three-phase reference values of the network voltage; i_{oa}^*, i_{ob}^* and i_{oc}^*

are the references for the output terminal currents of the VSC; i_a, i_b and i_c are the instantaneous output currents of VSCs; v_a, v_b and v_c are the instantaneous output voltages of the VSC.

The current control loop is described as:

$$\begin{bmatrix} e_{an} \\ e_{bn} \\ e_{cn} \end{bmatrix} = (k) \begin{bmatrix} i_{oa}^{*} - i_{oa} \\ i_{ob}^{*} - i_{ob} \\ i_{oc}^{*} - i_{oc} \end{bmatrix} + \begin{bmatrix} v_a \\ v_b \\ v_c \end{bmatrix} \tag{3.3}$$

where k is the resonant gain; i_{oa}, i_{ob} and i_{oc} are the instantaneous inductor currents of the VSC; e_{an}, e_{bn} and e_{cn} are the reference voltage at the output of the PR controller.

A fourth leg of the 3P4W VSC provides a neutral point, as well as regulates the zero-sequence voltage (e_z). In the PWM, e_z should be added to e_{an}, e_{bn} and e_{cn}. Therefore, the updated references of three-phase output voltages for PWM, which are e_{an}^{*}, e_{bn}^{*} and e_{cn}^{*}, are set as follows.

$$e_{an}^{*} = e_{an} + e_z \tag{3.4}$$

$$e_{bn}^{*} = e_{bn} + e_z \tag{3.5}$$

$$e_{bn}^{*} = e_{bn} + e_z \tag{3.6}$$

where e_z is the reference voltage of the fourth leg of the VSC and can be derived in (3.7) [150].

$$e_z = v_{dc}\,(0.5 - \mu) - (1 - \mu)\, v_{max} - \mu v_{min} \tag{3.7}$$

where v_{dc} is the voltage across the DC-link capacitor; v_{max} and v_{min} are the instantaneous maximum and the minimum voltage values of the three reference voltages; μ is the distribution ratio and has a value between 0 and 1 [151].

The PR controller is implemented in the abc coordinates, meaning that the voltage and current of each phase can be controlled independently. Also, extra decoupling control loops are not required, resulting in a simplified design process.

In this thesis, the SOP under the ASP control is named as ASP-SOP.

3.4 Control Strategy of the ASP-SOP in Unbalanced ADNs

The primary objective of employing the 3P4W-B2B-VSC based ASP-SOP within ADNs is to address the challenges associated with the load imbalances between connected feeders, as well as the phase imbalances within heavily-loaded feeders. Therefore, the proposed control strategies are categorised into three distinct groups based on their control effects:

1. Load balancing
2. Phase imbalance compensation
3. Combination of load balancing and phase imbalance compensation

For the context of this study, the preconditions for two feeders are as follows:

- The two feeders are originally connected through the point of common coupling (PCC) and then interconnected via the ASP-SOP at the end of both feeders.
- Feeder #1 operates under light loading conditions
- Feeder #2 experiences heavy loading, potentially extending to overloading, accompanied by serious phase imbalances.

- The load balancing should be achieved between feeder #1 and #2; meanwhile, the phase imbalance compensation is needed for feeder #2.

3.4.1 Load Balancing

In this part, the control of the SOP is to achieve the load balancing between connected feeders. After the load balancing, the expected complex power injection of two feeders from PCC is shown in (3.8).

$$S_1^{New} = S_2^{New} = \frac{S_1 + S_2}{2} \tag{3.8}$$

where S_1 and S_2 are the complex power injection of the feeder #1 and #2 from the PCC before the SOP operation; S_1^{New} and S_2^{New} are the complex power injection of the feeder #1 and #2 from the PCC after the SOP operation.

Therefore, the power reference of SOP can be calculated.

$$S^{SOP} = \frac{S_2 - S_1}{2} \tag{3.9}$$

where S^{SOP} is the power reference of the SOP. The positive value means that the power flow is transferred from the light feeder to the heavy feeders; the negative value indicates that the power flow is transferred from the heavy feeders to the light feeder.

If the total power flow is less or equal to the capacity of SOP, the load balancing can be fully realised, meaning that the expected complex power injection of two feeders from PCC, as shown in (3.8) can be achieved.

However, when S^{SOP} is greater than the SOP capacity as shown in (3.10), the load imbalance can only be mitigated but not fully solved.

$$S^{SOP} = \frac{S_2 - S_1}{2} > S_{SOP}^{Capaciy} \tag{3.10}$$

where $S_{SOP}^{Capaciy} \geq 0$ is the capacity of SOP. The power reference of the SOP becomes:

$$S^{SOP} = S_{SOP}^{Capaciy} \tag{3.11}$$

After the operation of the SOP, the value of S_1^{New} and S_2^{New} are shown as below.

$$S_1^{New} = S_1 + S_{SOP}^{Capaciy} \tag{3.12}$$

$$S_2^{New} = S_2 - S_{SOP}^{Capaciy} \tag{3.13}$$

The flowchart for the control strategy of the load balancing is shown in Fig 3.3.

3.4.2 Phase Imbalance Compensation

In this part, the SOP control is deployed to solve the phase imbalance issue and achieve a three-phase balance in the heavy-loaded feeder #2. As shown in (3.14), the expected complex power injection on each phase of feeder #2 is the average value of S_2.

$$S_{2,\varphi}^{New} = \frac{S_2}{3} \tag{3.14}$$

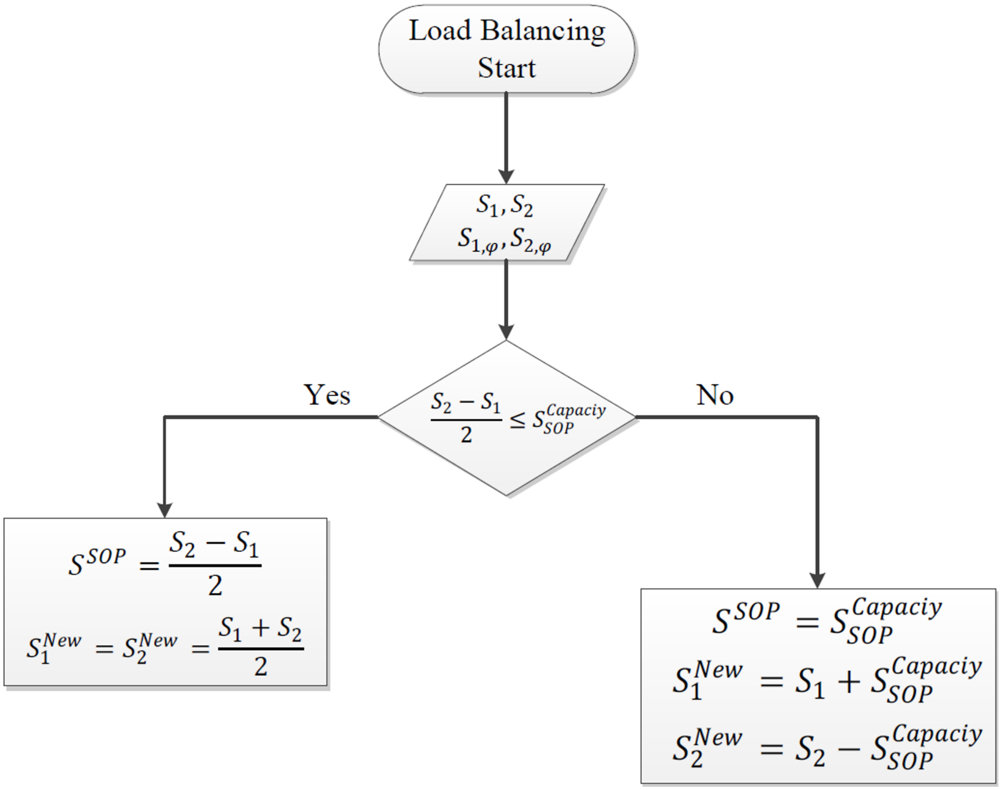

Figure 3.3: Flowchart of Load Balancing Control

where $S_{2,\varphi}^{New}$ is the complex power injection on phase φ of feeder #2 after the SOP operation; φ refers to phase a, b, and c.

Thus, the power references on each phase of SOP are calculated.

$$S_{\varphi}^{SOP} = S_{2,\varphi} - S_{2,\varphi}^{New} = S_{2,\varphi} - \frac{S_2}{3} \tag{3.15}$$

where S_{φ}^{SOP} is the power reference on each phase of SOP.

Due to the existence of the SOP capacity limits, the S_{φ}^{SOP} cannot be beyond the three-phase average value of SOP capacity. As a result, equation (3.16) must be verified to ensure that the capacity limits are met.

$$Max\left|S_{2,\varphi} - \frac{S_2}{3}\right| \leq \frac{S_{SOP}^{Capaciy}}{3} \tag{3.16}$$

When (3.16) is satisfied, the phase imbalance can be eliminated with the total power flow through SOP being zero.

If (3.16) is not satisfied and (3.17) is satisfied, the phase imbalance compensation can still be fully realized while the total power flow through the SOP is nonzero.

$$S_{2,Max} - S_{2,Min} \leq \frac{2}{3} S_{SOP}^{Capacity} \tag{3.17}$$

where $S_{2,Max}$ and $S_{2,Min}$ are the maximum and minimum values of the complex power injection from PCC among the three phases of feeder #2 before the operation of SOP.

The new expected complex power injection on each phase of feeder #2 becomes:

$$S_{2,\varphi}^{New} = \frac{S_{2,Max} + S_{2,Min}}{2} \tag{3.18}$$

The power reference on each phase of SOP is calculated in (3.19) and the phase balance can be fully achieved:

$$S_{\varphi}^{SOP} = S_{2,\varphi} - \frac{S_{2,Max} + S_{2,Min}}{2} \tag{3.19}$$

If (3.17) is not satisfied, the phase imbalances can only be mitigated. After the operation of

SOP, the expected complex power injection from PCC on each phase of feeder #2 is:

$$S_{2,\varphi}^{New} = \begin{cases} S_{2,Min} + \frac{S_{SOP}^{Capacity}}{3} \\ \frac{S_{2,Max}+S_{2,Min}}{2} \\ S_{2,Max} - \frac{S_{SOP}^{Capacity}}{3} \end{cases} \tag{3.20}$$

The underlying idea of (3.20) is that to substantially mitigate the phase imbalance to the greatest extent. To achieve this, the value of $S_{2,\varphi}^{New}$ is intended to approximate the average value of $S_{2,Max}$ and $S_{2,Min}$ as closely as possible.

As a result, the power reference of SOP can be determined.

$$S_{\varphi}^{SOP} = S_{2,\varphi} - S_{2,\varphi}^{New} = \begin{cases} -\frac{S_{SOP}^{Capacity}}{3} \\ S_{2,Median} - \frac{S_{2,Max}+S_{2,Min}}{2} \\ \frac{S_{SOP}^{Capacity}}{3} \end{cases} \tag{3.21}$$

where $S_{2,Median}$ is the complex power injection on the phases of feeder #2 beside $S_{2,Max}$ and $S_{2,Min}$, before the operation of SOP.

Then, the limitation of SOP capacity will be rechecked.

$$S_{2,Median} - \frac{S_{2,Max} + S_{2,Min}}{2} \leq \frac{S_{SOP}^{Capacity}}{3} \tag{3.22}$$

If the power reference of SOP is above the capacity and (3.22) is not satisfied, (3.23) and (3.24) calculate the new values for the expected complex power injection on each phase of feeder #2 after the operation of SOP and the power reference of each phase of SOP. It's noteworthy that all three SOP phases operate at their maximum capacity.

$$S_{2,\varphi}^{New} = \begin{cases} S_{2,Min} + \frac{S_{SOP}^{Capacity}}{3} \\ S_{2,Median} \pm \frac{S_{SOP}^{Capacity}}{3} \\ S_{2,Max} - \frac{S_{SOP}^{Capacity}}{3} \end{cases} \tag{3.23}$$

$$S_{\varphi}^{SOP} = S_{2,\varphi} - S_{2,\varphi}^{New} = \begin{cases} -\frac{S_{SOP}^{Capacity}}{3} \\ \mp\frac{S_{SOP}^{Capacity}}{3} \\ \frac{S_{SOP}^{Capacity}}{3} \end{cases} \tag{3.24}$$

The control flowchart of the phase imbalance compensation is shown in Fig 3.4.

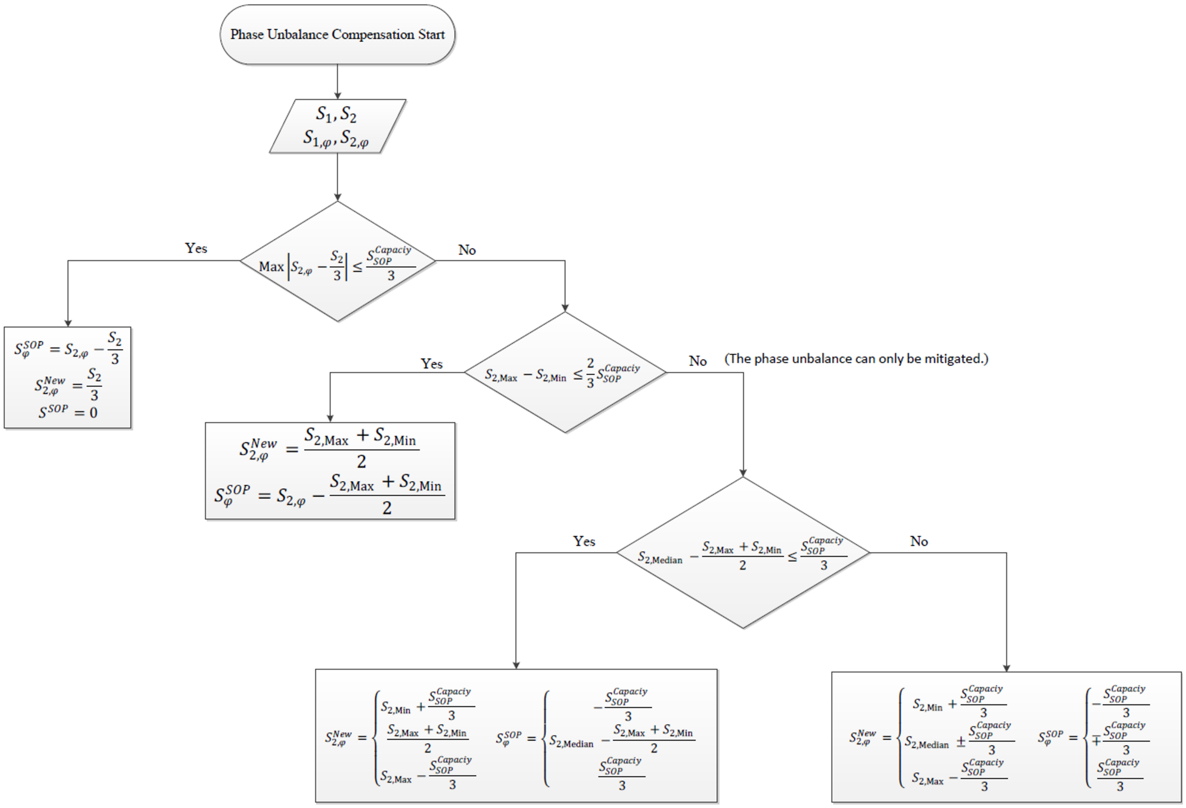

Figure 3.4: Control Flowchart of Phase Imbalance Compensation

3.4.3 Load Balancing & Phase Imbalance Compensation

In this section, the objectives are twofold: concurrently achieving load balancing (LB) and phase imbalance compensation (PIC).

Initially, when the LB between the feeders is attained, the expected complex power injections of both feeders are detailed in (3.25).

$$S_1^{New} = S_2^{New} = \frac{S_1 + S_2}{2} \tag{3.25}$$

Subsequently, after the accomplishment of PIC, the anticipated power injection for each phase of Feeder #2 at the PCC is given in (3.26).

$$S_{2,\varphi}^{New} = \frac{S_1 + S_2}{6} \tag{3.26}$$

Therefore, the power references on each phase of the SOP are calculated.

$$S_{\varphi}^{SOP} = S_{2,\varphi} - \frac{S_1 + S_2}{6} \tag{3.27}$$

The capacity limits of SOP should be checked by (3.28). When the condition in (3.28) can be met, indicating that the SOP operates within its capacity limits, both the LB of feeders and the PIC on feeder #2 can be fully obtained at the same time.

$$\max \left| S_{2,\varphi} - \frac{S_1 + S_2}{6} \right| \leq \frac{S_{SOP}^{Capacity}}{3} \tag{3.28}$$

$$\frac{S_2 - S_1}{2} \leq S_{SOP}^{Capacity} \tag{3.29}$$

$$Max\left|S_{2,\varphi}-\frac{S_2}{3}\right|\leq\frac{S_{SOP}^{Capaciy}}{3} \tag{3.30}$$

Consequently, equations (3.28), (3.29) and (3.30) constitute three conditions that determine the achievable extent of LB and PIC.

- The fulfilment of the condition in (3.29) represents that the LB can be separately actualised.
- If the condition in (3.30) is met, the PIC can be separately accomplished.
- Meeting the condition set in (3.28) indicates the potential for the simultaneous realisation of both LB and PIC.
- When the condition in (3.29) and (3.30) can be fulfilled whilst the condition in (3.28) is not satisfied, one of the LB and PIC can be fully realised while the other can only be achieved to a partial extent.

Under the last circumstances listed above, it becomes essential to prioritise the sequence of the LB and the PIC. This prioritisation is designed for two purposes:

- Maximise the efficacy of the LB and the PIC.
- Ensure the power of the SOP within its designated limits of capacity.

Hence, two distinct control sequences are developed, as shown in Table 3.1.

Table 3.1: Sequences of SOP Control Strategy

Sequences	First Step	Second Step
PIC+LB	PIC	LB
LB+PIC	LB	PIC

PIC+LB

In this sequence, the first step is to fully realise the PIC. Therefore, $S_{2,\varphi}^{New}$ and S_{φ}^{SOP} are expressed as follows:

$$S_{2,\varphi}^{New} = \frac{S_2}{3} \tag{3.31}$$

$$S_{\varphi}^{SOP} = S_{2,\varphi} - \frac{S_2}{3} \tag{3.32}$$

The redundant capacity of the SOP on each phase, which represents the specific capacity available on each phase for the purpose of LB, can be quantified as follows:

$$S_{aval,\varphi}^{Capacity} = \frac{S_{SOP}^{Capacity}}{3} - \max(S_{2,\varphi} - \frac{S_2}{3}) \tag{3.33}$$

where $S_{aval,\varphi}^{Capacity} \geq 0$ is the surplus capacity on each phase of the SOP.

In the load balancing of the second step, the calculated results of equation (3.33) can guarantee that every phase of SOP runs within its capacity. After the LB, the updated values for the feeders' power injection and the SOP's power references can be determined.

$$S_{2,\varphi}^{New} = \frac{S_2}{3} - \left[\frac{S_{SOP}^{Capaciy}}{3} - Max\left(S_{2,\varphi} - \frac{S_2}{3} \right) \right] \tag{3.34}$$

$$S_{\varphi}^{SOP} = S_{2,\varphi} - S_{2,\varphi}^{New} \tag{3.35}$$

As a consequence, the phase imbalance can be eradicated, while simultaneously the load imbalance between feeders can be mitigated to the utmost degree.

LB +PIC

In this sequence, the first step is to fully achieve LB. Thus, the reference of the total power of SOP can be calculated.

$$S^{SOP} = \frac{S_2 - S_1}{2} \tag{3.36}$$

In the second step of the PIC, two distinct conditions need separate discussions.

1. The power injections from the PCC, across the three phases of feeder #2, only have one maximum value, specifically denoted as $S_{2,Max}$, $S_{2,Median}$ and $S_{2,Min}$.
2. Two of the three phases share the maximum power injection value, represented as $S_{2,Max}$, $S_{2,Max}$ and $S_{2,Min}$.

For condition #1 involving a single maximum power injection value, as the LB has been fully actualised through (3.36), all excess capacity on the phase with $S_{2,Max}$ should be employed for the PIC.

For the phase with the maximum power injection, the expected value of the feeders' power injection from the PCC, and the SOP's power reference for the phase with $S_{2,Max}$, are presented in (3.37) and (3.38).

$$S_{2,\varphi}^{New} = S_{2,Max} - \frac{S_{SOP}^{Capacity}}{3} \tag{3.37}$$

$$S_{\varphi}^{SOP} = \frac{S_{SOP}^{Capacity}}{3} \tag{3.38}$$

For the other two phases with $S_{2,Median}$ and $S_{2,Min}$,

$$S_{2,\varphi}^{New} = \frac{1}{2}[\frac{S_1+S_2}{2} - (S_{2,Max} - \frac{S_{SOP}^{Capacity}}{3})] \tag{3.39}$$

$$S_{\varphi}^{SOP} = S_{2,\varphi} - \frac{1}{2}[\frac{S_1+S_2}{2} - (S_{2,Max} - \frac{S_{SOP}^{Capacity}}{3})] \tag{3.40}$$

If the value given by (3.40) satisfies condition (3.41), indicating that each phase of SOP operates within its capacity limits.

$$S_{2,\varphi} - \frac{1}{2}[\frac{S_1+S_2}{2} - (S_{2,Max} - \frac{S_{SOP}^{Capacity}}{3})] \leq \frac{S_{SOP}^{Capacity}}{3} \tag{3.41}$$

When the condition (3.41) is not satisfied, the three phases need to be treated separately. For the phase with the maximum power injection, $S_{2,\varphi}^{New}$ and S_{φ}^{SOP} can still be obtained in (3.37) and (3.38).

For the phase with the median power injection, as the condition in (3.41) is not met, all remaining capacity should be applied for the PIC. Thus, $S_{2,\varphi}^{New}$ and S_{φ}^{SOP} can be given as follows.

$$S_{2,\varphi}^{New} = S_{2,Median} - \frac{S_{SOP}^{Capacity}}{3} \tag{3.42}$$

$$S_{\varphi}^{SOP} = \frac{S_{SOP}^{Capacity}}{3} \tag{3.43}$$

For the phase with the minimum power injection, since the other two phases of the SOP are operating at their maximum capacity, the requirement of LB should be considered when determining the power reference. $S_{2,\varphi}^{New}$ and S_{φ}^{SOP} can be described as follows.

$$S_{\varphi}^{SOP} = S^{SOP} - \frac{2}{3} S_{SOP}^{Capaciy} = \frac{S_2 - S_1}{2} - \frac{2}{3} S_{SOP}^{Capacity} \tag{3.44}$$

$$S_{2,\varphi}^{New} = S_{2,Min} - \left(S^{SOP} - \frac{2}{3} S_{SOP}^{Capacity} \right) = S_{2,Min} - \left(\frac{S_2 - S_1}{2} - \frac{2}{3} S_{SOP}^{Capacity} \right) \tag{3.45}$$

For condition #2 where two out of the three phases share identical maximum power injection values, on the two phases with the same maximum power injection, the SOP functions at full capacity on these two phases, aiming to decrease the power injection of feeder #2 from the PCC. Meanwhile, for the phase with $S_{2,Min}$, the requirement of LB should be incorporated when determining the power reference.

For the two phases with $S_{2,Max}$,

$$S_{\varphi}^{SOP} = \frac{S_{SOP}^{Capacity}}{3} \tag{3.46}$$

$$S_{2,\varphi}^{New} = S_{2,Max} - \frac{S_{SOP}^{Capacity}}{3} \tag{3.47}$$

For the phase with $S_{2,Min}$,

$$S_{\varphi}^{SOP} = S^{SOP} - \frac{2}{3} S_{SOP}^{Capacity} = \frac{S_2 - S_1}{2} - \frac{2}{3} S_{SOP}^{Capacity} \tag{3.48}$$

$$S_{2,\varphi}^{New} = S_{2,Min} - (S^{SOP} - \frac{2}{3} S_{SOP}^{Capacity}) \tag{3.49}$$

The flowchart of realising these functions is shown in Fig 3.5.

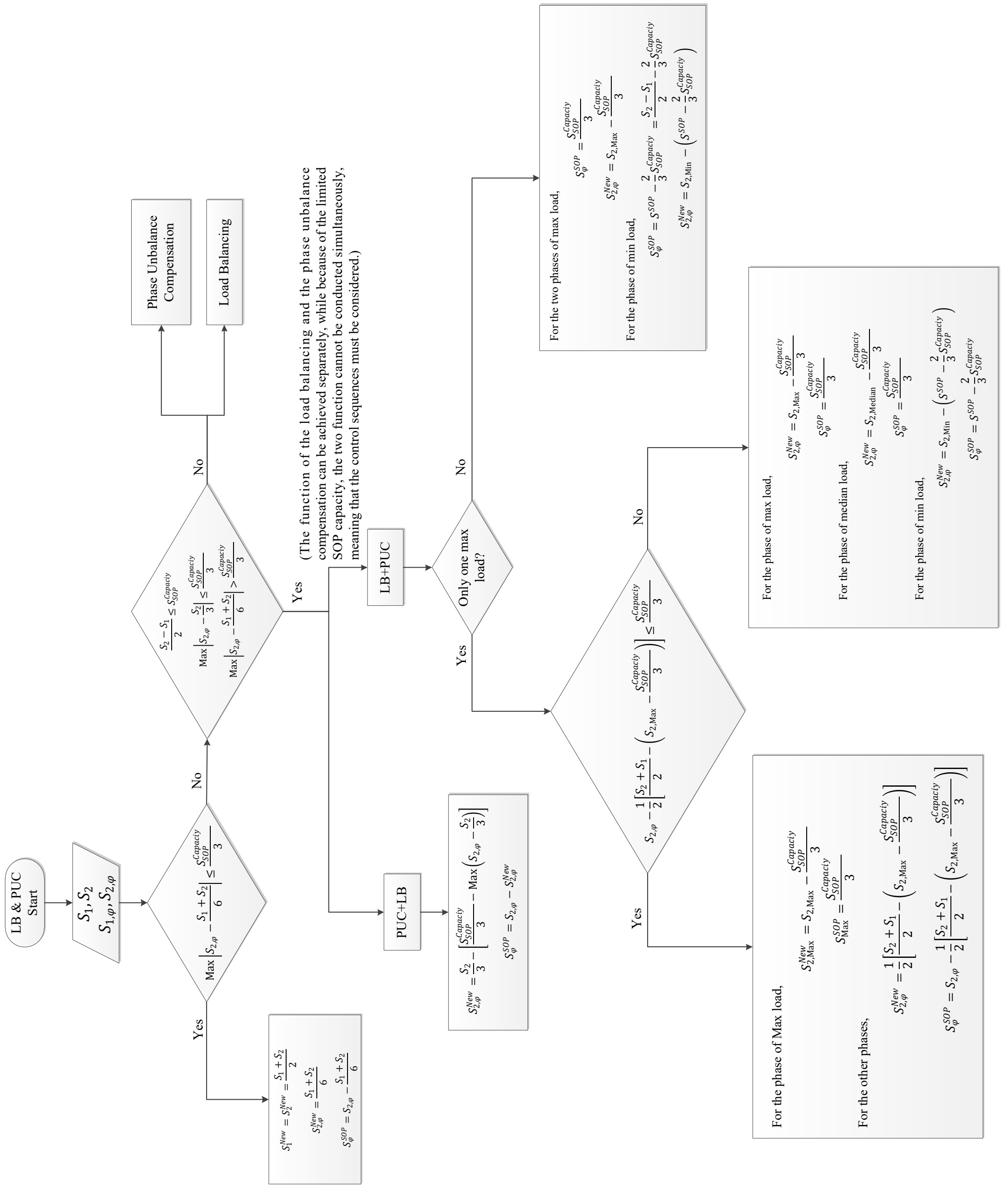

(The function of the load balancing and the phase unbalance compensation can be achieved separately, while because of the limited SOP capacity, the two function cannot be conducted simultaneously, meaning that the control sequences must be considered.)

Figure 3.5: Control Flowchart of LB and PIC

3.5 Case Study

In this case study, a time-domain power-electronics test model, established in Simulink/Matlab 2018a, is utilised to demonstrate the operational control and performance of the 3P4W-B2B-VSC based ASP-SOP.

3.5.1 Simulation Model

As illustrated in Fig 3.6, in the test model, two feeders are radially extended from a PCC of a distribution network. To interconnect the two feeders, an SOP is installed at the endpoint of both feeders. The screenshot of the test model, established in Simulink/Matlab is shown in Fig. 3.7.

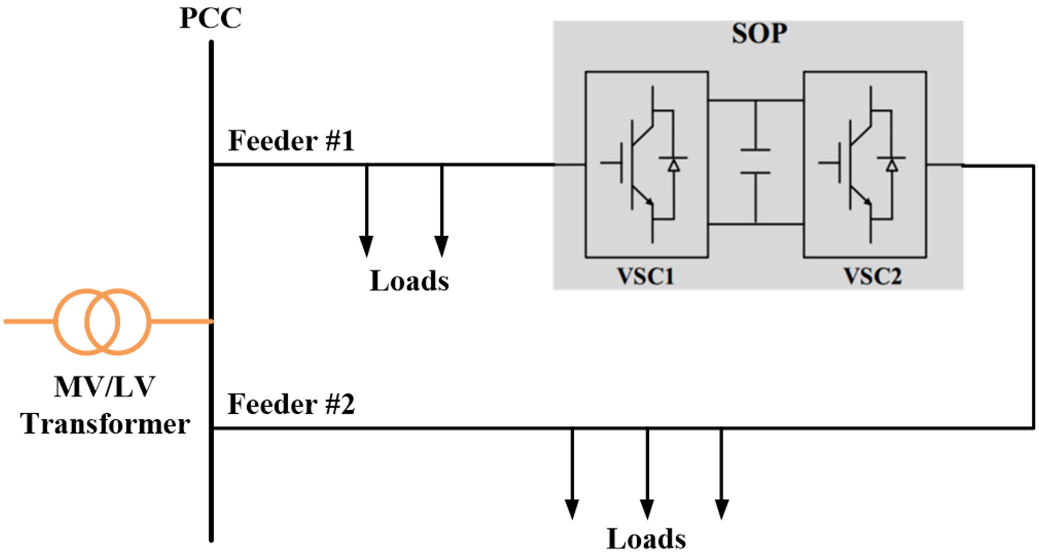

Figure 3.6: Illustration of Simulation Model of Two-Feeder Distribution Network with the SOP

The parameters, defining the feeders of the distribution network, are itemised in Table 3.2. The rated line-to-line voltage of the distribution network is 381 V. For each phase of the two feeders, the rated power is 166.67 kVA, with the maximum overload capacity reaching 250 kVA. Consequently, each feeder has a rated power of 500 kVA and a maximum overloaded power capacity of 750 kVA.

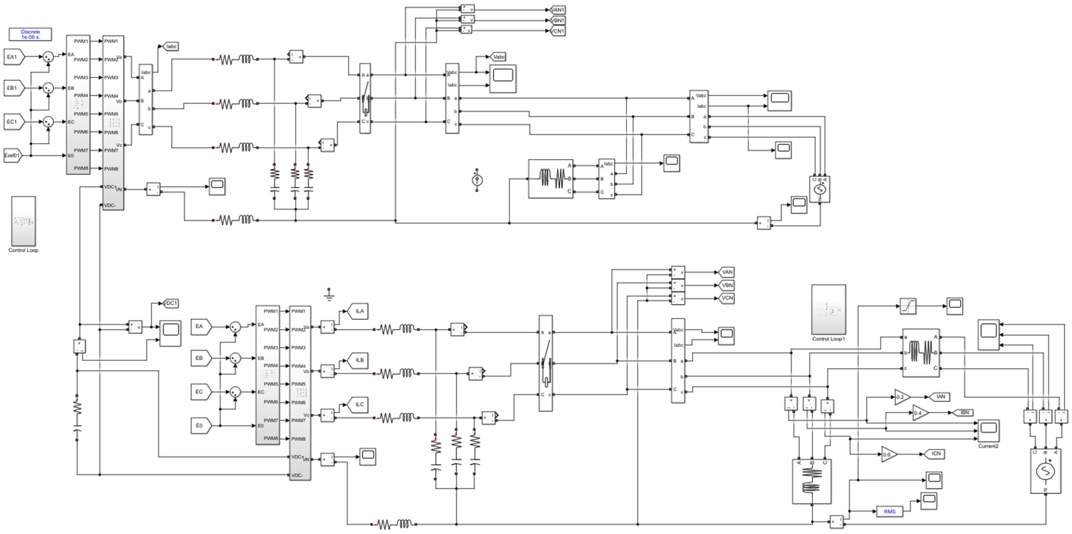

Figure 3.7: Screenshot of the Simulation Model in Simulink/Matlab

Table 3.2: Parameters of Feeders in the LV Distribution Network

Parameters	Value
Rated line to line voltage	381 V
Rated powers	500 kVA (in total) 166.67 kVA (each phase)
Maximum overloaded powers	750 kVA (in total) 250 kVA (each phase)
Cable ampacity (RMS value)	1.14 kA

Table 3.3: Conditions of Load Powers in Each Feeder

Feeder	**Load Power/kVA**			
	Phase A	**Phase B**	**Phase C**	**Total**
#1	20	30	50	100
#2	83.33	166.67	250	500

To assess the efficacy of the 3P4W-B2B-VSC based ASP-SOP in enhancing the power quality of the unbalanced network, as the load powers of two feeders shown in Table 3.3 and the load currents of feeder #2 displayed in Fig 3.8, not only the load imbalance between feeder #1 and #2 but also the phase imbalance within feeder #2 exists:

- Feeder #1 is light-loaded with a total load power of 100 kVA.
- Feeder #2 operates with significant phase imbalance among the three phases, with phase C running at the overloaded power level.

Therefore, the load balancing needs to be undertaken between the two feeders. Additionally, the phase imbalance compensation within the three phases of feeder #2 is essential.

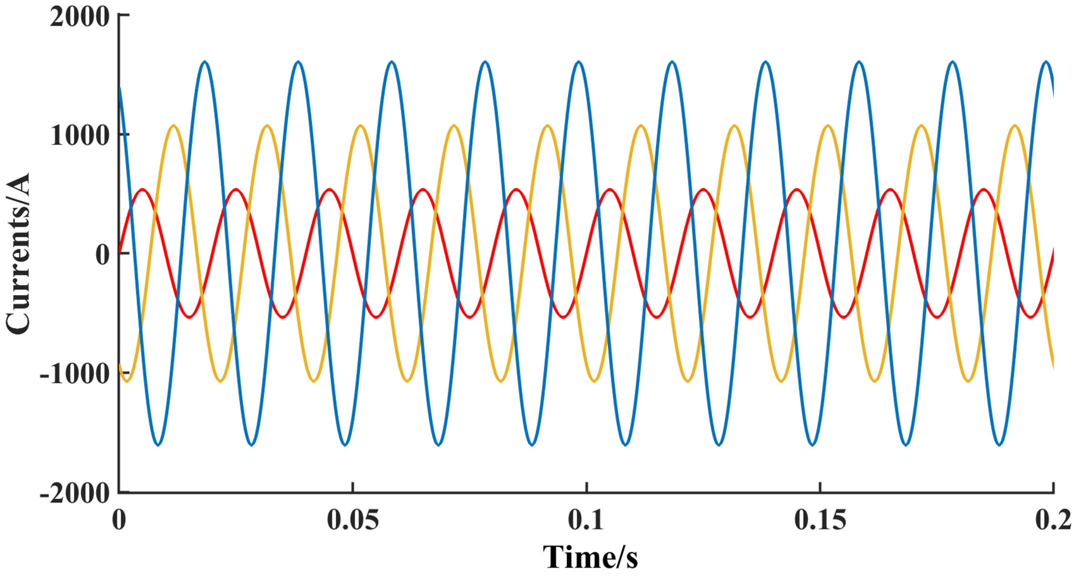

Figure 3.8: Currents of Loads in Feeder #2

The parameters of the ASP-SOP are in Table 3.4. In the simulations conducted, VSC1, which is directly connected to feeder 1, operates under the Vdc/Q mode, whereas VSC2, linked directly to feeder 2, functions in the ASP control.

Table 3.4: Parameters of the ASP-SOP

Parameters	Value
Rated Voltage	381 V
DC Link Capacitor	7500 μF
DC Link Voltage	800 V
Capacity(each phase)	166.67 kVA
Filter Inductor	1 mH
Filter Capacitor	10 μF

3.5.2 Analysis of Simulation Results

As shown in Fig 3.8, throughout the whole period of the simulation, the load power remains constant and, therefore, the currents of loads maintain the same value. From Fig 3.11, The ASP-SOP commences operation at 0.095s.

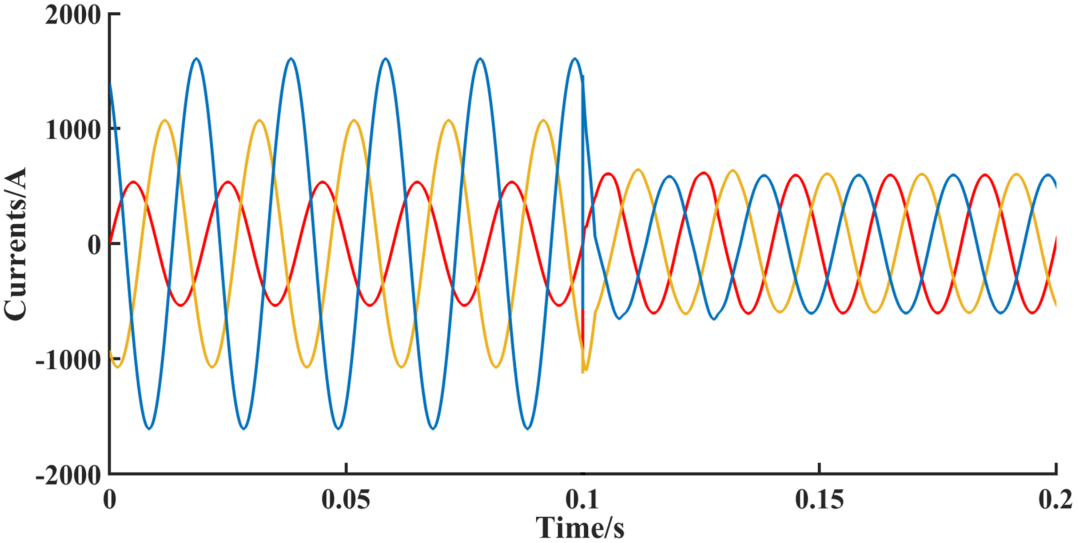

Figure 3.9: Injection Currents of Feeder #2 from the PCC

Before 0.095s, all loads of feeder #2 are exclusively supplied by the upstream power from the PCC, resulting in that the three-phase injection currents of feeder #2 from the PCC, in Fig 3.9, align with the loads' currents, in Fig 3.8, and exhibit substantial three-phase imbalance of current values.

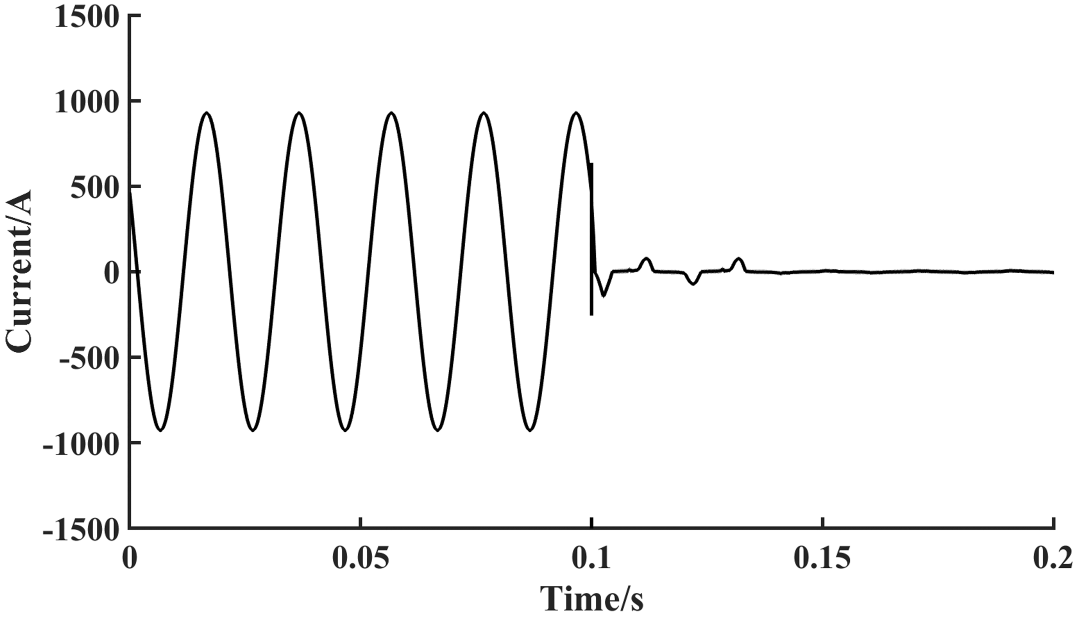

Figure 3.10: Neutral Line Current of Feeder #2

After the operation of ASP-SOP at 0.095s, the loads' demand of feeder #2 fulfilled through a combination of the output power of the ASP-SOP and the upstream power from the PCC, causing that with the currents of loads to keep constant as prior to 0.095s, the three-phase imbalance among the injection currents of feeder #2 from the PCC, in Fig 3.9, is greatly mitigated or even nearly eliminated.

The variation in the neutral line current of feeder #2 is presented in Fig. 3.10. Before the operation of the ASP-SOP, the existence of the three-phase imbalance in the load currents of feeder #2 results in the neutral line current reaching up to 610A. However, after the commencement of the ASP-SOP at 0.095s, the neutral line current is substantially reduced to almost zero.

Operation of ASP SOP

The waveform of output currents of the SOP in feeder #2 is shown in Fig. 3.11 and the values of the input and output power are given in Fig. 3.12. After the operation of the ASP SOP at 0.095s, because of the SOP terminal of feeder #2 under the ASP control, the three-phase output currents have three different values.

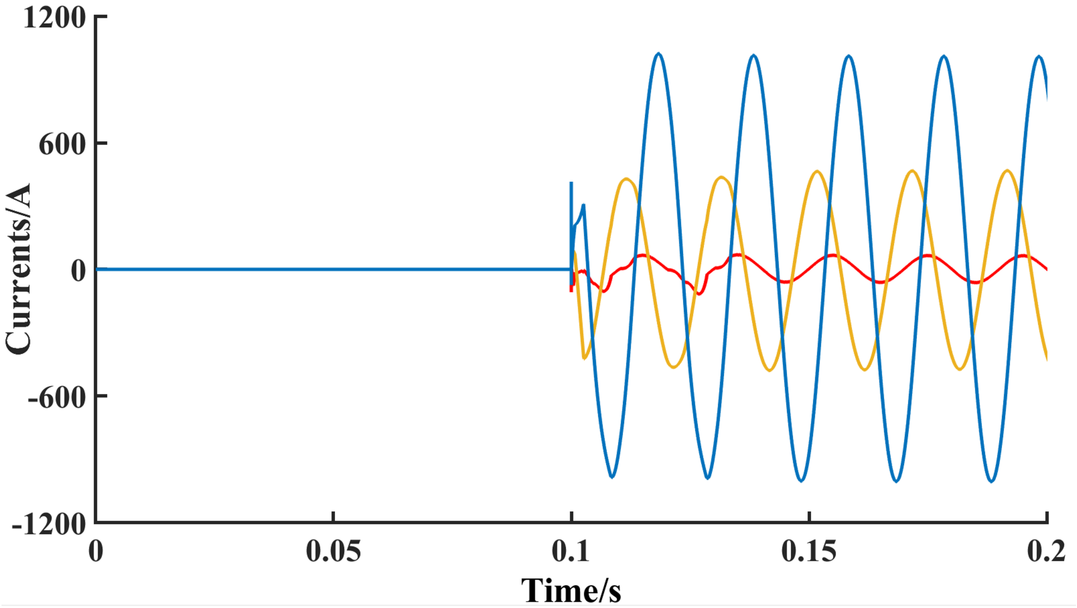

Figure 3.11: Output Currents of the SOP in Feeder #2

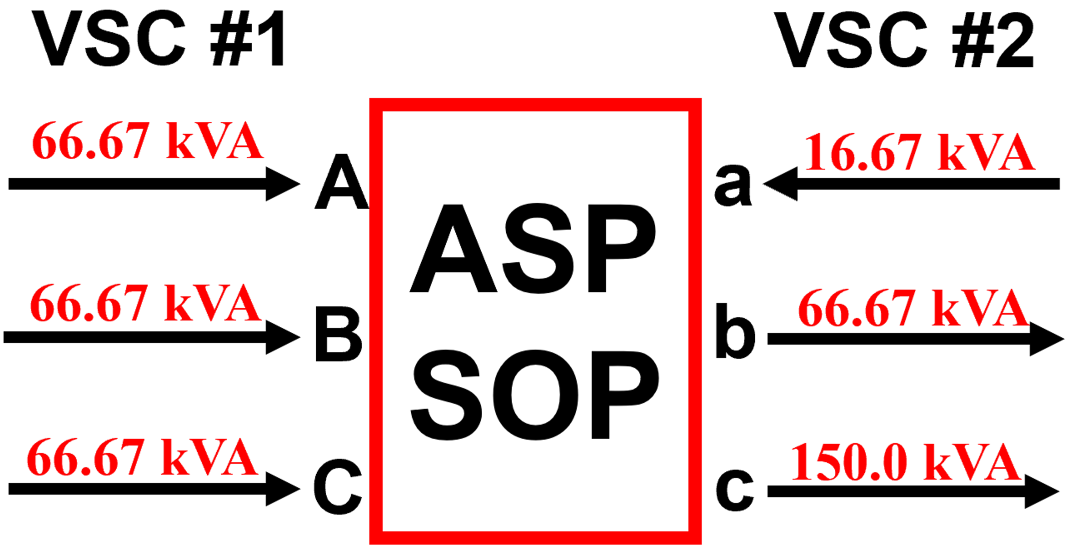

Figure 3.12: Input & Output Powers of the SOP

As mentioned in Section 3.4, the primary objectives of the ASP SOP are concurrently twofold:

1. The load balancing between interconnected feeders: Given that feeder #1 is lightly

loaded while feeder #2 is heavily loaded, the load balancing process involves the transfer of approximately 200 kVA from Feeder #1 to Feeder #2.

2. The phase imbalance compensation within the heavily loaded Feeder #2: The ASP SOP is configured to absorb 16.67 kVA from phase A and to deliver 66.67 kVA and 150 kVA to phases B and C, separately.

Owing to the sufficient installed capacity of the ASP SOP, which is 500 kVA in this case study, the requisite power transfer for the two objectives is feasible. As a result, both objectives — load balancing and phase imbalance compensation — can be simultaneously realised.

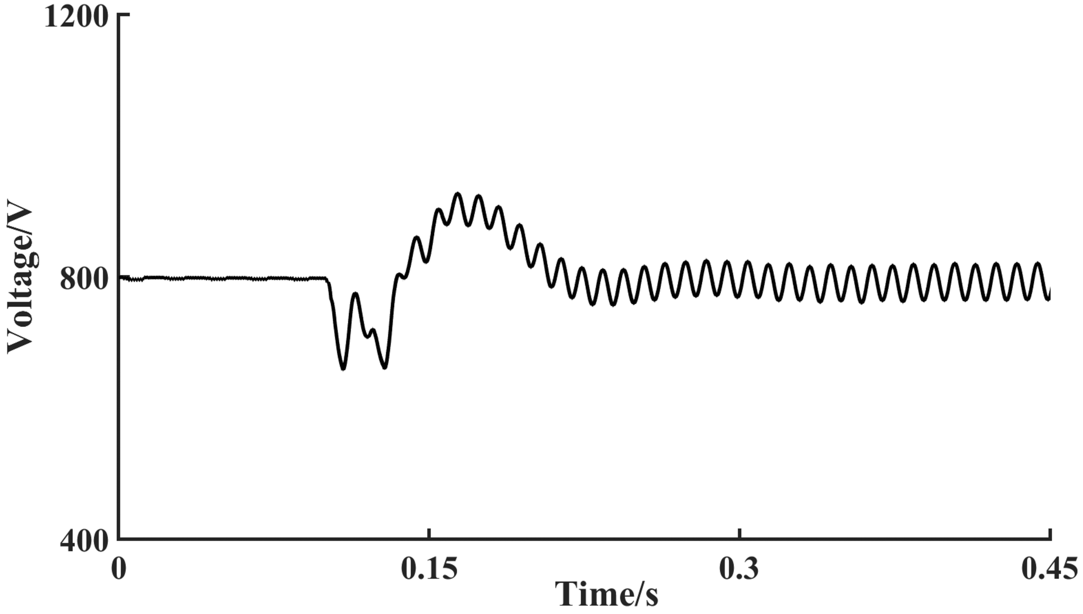

Figure 3.13: DC-side Voltage of the SOP

Effects of ASP SOP

In Table 3.5, the load balancing index of feeders can be calculated in (3.50).

$$LBI = \sum_{k=1}^{n} \left(\frac{I_k}{I_{k,\ rate}} \right)^2 \tag{3.50}$$

where I_k and $I_{k,\ rate}$ are the actual and rated branch current in feeder #k; n is the total number of feeders in the network.

Table 3.5: Conditions of Feeders Before & After the SOP Operation

Feeders		**Injection from the PCC / kVA**				**Load Balancing Index**
		Phase A	**Phase B**	**Phase C**	**Total**	
#1	**W/O SOP**	20	30	50	100	1.04
#2		83.33	166.67	250	500	
#1	**W/ SOP**	86.67	96.67	116.67	300	0.72
#2		100	100	100	300	

Table 3.5 reveals the change of conditions in the distribution of power across the three phases of two feeders, both pre- and post-operation of the ASP SOP. Initially, the total power injections of feeder #1 and feeder #2 from the PCC are 100 kVA and 500 kVA, respectively. After the SOP implementation, these two figures converge to a uniform value of 300 kVA for both feeders. The load balancing index, computed in (3.50), decreases by 30.77% from 1.04 to 0.72, signifying the achievement of load balancing between feeders #1 and #2.

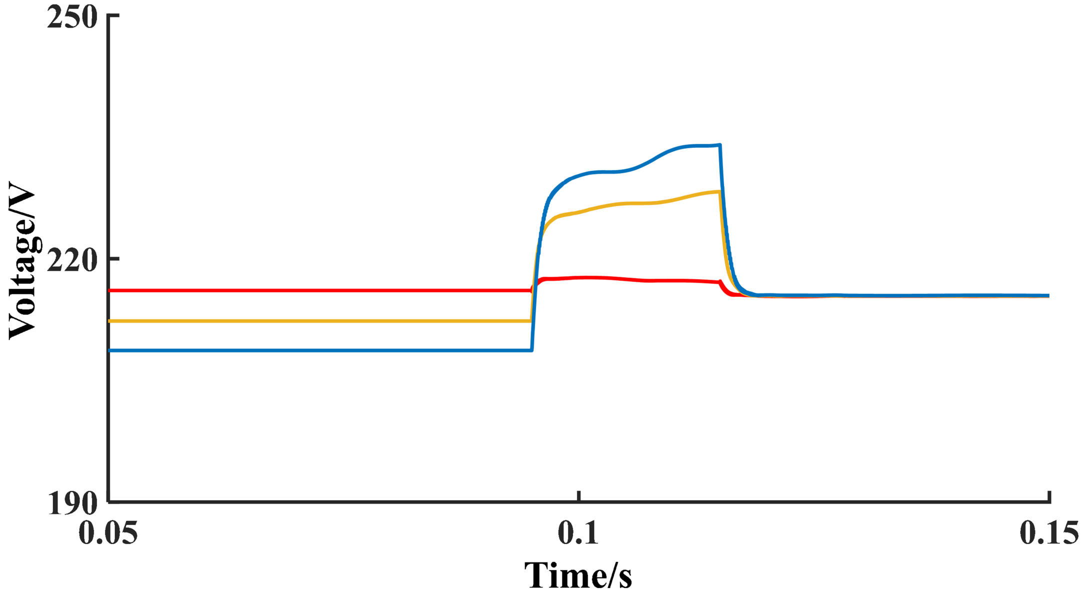

Figure 3.14: Values of Three Phase Voltages in Feeder #2

In Fig 3.14, the changes in the values of the three-phase voltages of the feeder #2, before and after the operation of the ASP SOP, are presented. Prior to the SOP's operation at 0.095s, the phase voltages on the loads of feeder #2 are unbalanced, attributable to the differential voltage drops caused by the unbalanced load currents. After the engagement of SOP at 0.095s, though the existence of a short transient period, the discrepancy in three-phase voltages on the loads is almost eliminated, caused by the impact of the ASP SOP on realising the phase imbalance compensation in feeder #2.

To further assess the improvement in the phase imbalance contributed by the ASP SOP, the indexes of the voltage imbalance can be calculated by (3.51).

$$V_{VI}\% = 100\% \times \frac{maximum\ deviation\ from\ average\ voltage}{average\ voltage} \tag{3.51}$$

Furthermore, the current imbalance can be estimated by (3.52).

$$I_{CI} = \sum_{\varphi=a}^{c} \left| I_\varphi - \frac{I_a + I_b + I_c}{3} \right| \tag{3.52}$$

where φ refers to phase a, b and c; I_φ is the actual phase current of the feeder; I_a, I_b and I_c are the actual current on phase a, b and c separately.

Table 3.6: Index Comparison for Feeder #2

Feeder #2	**Voltage Imbalance Index**	**Current Imbalance Index**
W/O SOP	1.75 %	709.9
W/SOP	2.1m %	1.769

According to Table 3.6, a clear improvement in the operational performance of feeder #2 brought by the ASP SOP is exhibited. Initially, without the SOP, feeder #2 operates with a voltage imbalance index of 1.75 and a current imbalance index of 709.9, suggesting a severe imbalance in the voltage and current distribution in feeder #2. After the placement of the SOP, the imbalance indexes of both voltage and current obtain a dramatic reduction of over 99%, referring to a near-perfect three-phase balance in feeder #2.

3.6 Conclusions

This chapter investigates the potential of a new type of SOP, named ASP-SOP, at the converter level of the flexible power electronics device.

Focusing on scenarios incorporating a neutral line in unbalanced ADNs, the 3P4W-B2B-VSC topology is applied for the topology of SOPs. Based on the new topology application, the ASP control scheme is developed for the ASP-SOP. Unlike the conventional SOPs, the terminal of the ASP-SOP, which is under the ASP control, can have three different current/power values in three phases. This innovation led to the development of a control strategy aiming to address two critical challenges of the distribution network: (1) the load imbalance between connected feeders and (2) the phase imbalance in the heavily loaded feeders. The results of simulations indicate that in the unbalanced network, the 3P4W-B2B-VSC based ASP-SOP can achieve load balancing between feeders and phase imbalance compensation in the heavily loaded feeder.

Chapter 4

Operational Optimisation of Active Distribution Networks based on All-Switching-Phase Soft Open Points

4.1 Introduction

Based on the device-level research on the topology and control of SOP in Chapter 3, this chapter explores the potential of the new 3P4W-B2B-VSC based phase-changing SOP in the system-level optimisation of ADN, combining two perspectives: ADN optimisation and power-electronic implementation. The work and contributions of this research are summarised as follows:

- New Model of Phase-sharing SOP: The proposed ASP-SOP, based on the 3P4W-B2B-VSC topology, is modelled in detail and the integration of energy storage into ASP-SOP is also considered.

- New System-Level Optimisation Strategy & Approach: An optimal operation strategy based on developed ASP- SOPs is proposed for unbalanced ADNs, with the aims of power loss reduction and voltage imbalance mitigation. To efficiently solve the three-phase OPF, the symmetrical SDP method is applied to convert the original non-convex nonlinear model into an SDP model.
- Mutual Verification: Time-domain simulations of power electronic devices and system-level optimisation can be employed to mutually validate and corroborate each other's results, which can guide the practical operation of DSO.

4.2 Mathematical Modelling of Different All-Switching-Phase Soft Open Points

For the traditional SOP, the control objectives usually be the power input/output at the terminals of SOP, causing that in the modelling of SOP-based optimisation, the control variables of SOP often be the active power absorbed/supplied at the two terminals. However, the terminal of the one-side ASP-SOP, which is under the ASP control, can have three different current/power values in three phases. Meanwhile, in the two-side ASP-SOP, all six AC phases can be regulated independently and have different values of the current/power. In the two-side ASP-SOP with ES, the ES is integrated into the DC side of SOP. That's why in the ASP-SOP, the control variables are the active power values of the phases at the terminals under all-switching-phase control. Four types of SOPs, as listed in Table 4.1, will be modelled and compared.

Table 4.1: Different Types of SOPS

SOP Types	**Control of SOP**	
	Side #1	**Side #2**
Traditional SOP	Vdc/Q	P/Q
One-side ASP-SOP	Vdc/Q	ASP
Two-side ASP-SOP	ASP	ASP
Two-side ASP-SOP with ES [152]	ASP	ASP

Equation (4.1) and (4.2) are the power loss constraints of the SOP at the terminal of bus i and bus j, respectively.

$$P_{SOP,Loss}^{\varphi,i,t} = A_{SOP}\sqrt{\left(P_{SOP}^{\varphi,i,t}\right)^2 + \left(Q_{SOP}^{\varphi,i,t}\right)^2} \tag{4.1}$$

$$P_{SOP,Loss}^{\varphi,j,t} = A_{SOP}\sqrt{\left(P_{SOP}^{\varphi,j,t}\right)^2 + \left(Q_{SOP}^{\varphi,j,t}\right)^2} \tag{4.2}$$

where $P_{SOP,Loss}^{\varphi,i,t}$, $P_{SOP,Loss}^{\varphi,j,t}$ are power losses of SOP on phase φ of node i/j at the time t; A_{SOP} is the power loss coefficient of SOP; $P_{SOP}^{\varphi,i,t}$, $P_{SOP}^{\varphi,j,t}$ are the active power injections by the SOP on phase φ of node i/j at the time t; $Q_{SOP}^{\varphi,i,t}$, $Q_{SOP}^{\varphi,j,t}$ are the reactive power injections by SOP on phase φ of node i/j at the time t; φ refers to phases a, b and c.

The capacity constraints of the SOP, installed between bus i and bus j, are described as follows.

$$\sqrt{\left(P_{SOP}^{\varphi,i,t}\right)^2 + \left(Q_{SOP}^{\varphi,i,t}\right)^2} \leq \frac{S_{SOP}^{Capacity,\ i}}{3} \tag{4.3}$$

$$\sqrt{\left(P_{SOP}^{\varphi,j,t}\right)^2 + \left(Q_{SOP}^{\varphi,j,t}\right)^2} \leq \frac{S_{SOP}^{Capacity,j}}{3} \tag{4.4}$$

where $S_{SOP}^{Capacity,i}$, $S_{SOP}^{Capacity,j}$ are the capacity of the SOP at the node i/j.

The basic active power constraint of SOPs is as below.

$$\sum_{\varphi=a}^{c}\left(P_{SOP}^{\varphi,i,t} + P_{SOP,Loss}^{\varphi,i,t}\right) + \sum_{\varphi=a}^{c}\left(P_{SOP}^{\varphi,j,t} + P_{SOP,Loss}^{\varphi,j,t}\right) = 0 \tag{4.5}$$

4.2.1 Traditional SOP Constraints

In traditional SOPs, as the two sides are usually under the control of either V_{dc}/Q or P/Q, equation (4.5), (4.6) and (4.6) can guarantee that all three phases at one side of either input or output always have the same active/reactive power.

$$P_{SOP}^{a,i,t} = P_{SOP}^{b,i,t} = P_{SOP}^{c,i,t} \tag{4.6}$$

$$P_{SOP}^{a,j,t} = P_{SOP}^{b,j,t} = P_{SOP}^{c,j,t} \tag{4.7}$$

4.2.2 One-Side ASP-SOP Constraints

If the terminal at node i is under the control of V_{dc}/Q and the one at node j is under the ASP control, the constraint (4.5) should be replaced by (4.8) and (4.9).

$$P_{SOP}^{a,i,t} = P_{SOP}^{b,i,t} = P_{SOP}^{b,i,t} \tag{4.8}$$

$$3P_{SOP}^{a,i,t} + \sum_{\varphi=a}^{c} P_{SOP,\ \ Loss}^{\varphi,i,t} + \sum_{\varphi=a}^{c} \left(P_{SOP}^{\varphi,j,t} + P_{SOP,\ \ Loss}^{\varphi,j,t} \right) = 0 \tag{4.9}$$

Otherwise, if the side at node *j* is under the control of V_{dc}/Q and at node *i* is under the ASP control, the constraints will be (4.10) and (4.11).

$$P_{SOP}^{a,j,t} = P_{SOP}^{b,j,t} = P_{SOP}^{c,j,t} \tag{4.10}$$

$$\sum_{\varphi=a}^{c} \left(P_{SOP}^{\varphi,i,t} + P_{SOP,\ \ Loss}^{\varphi,i,t} \right) + 3P_{SOP}^{a,j,t} + \sum_{\varphi=a}^{c} P_{SOP,\ \ Loss}^{\varphi,j,t} = 0 \tag{4.11}$$

4.2.3 Two-Side ASP-SOP Constraints

The constraints of the two-side ASP-SOP are the same as the basic constraint (4.5).

4.2.4 Constraints for Two-Side ASP-SOP with Energy Storage

In the two-side ASP-SOP with energy storage (ES), the overall constraint for this type of SOP is in equation (4.12).

$$\sum_{\varphi=a}^{c}\left(P_{SOP}^{\varphi,i,t}+P_{SOP,\ \ Loss}^{\varphi,i,t}\right)+\sum_{\varphi=a}^{c}\left(P_{SOP}^{\varphi,j,t}+P_{SOP,\ \ Loss}^{\varphi,j,t}\right)+P_{t}^{ES}+P_{t}^{ES,Loss}=0 \tag{4.12}$$

where P_t^{ES} is the input/output power of the ES and $P_t^{ES,Loss}$ is the power loss of the ES. When the ES is discharged, $P_t^{ES} \geq 0$; vice versa, $P_t^{ES} \leq 0$.

Equations (4.13)-(4.16) are the constraints for the ES system integrated into the two-side ASP-SOP. Constraint (4.13) determines that the stored energy of the ES at the time $(t+1)$ is obtained from the previous state of ES, the input/output power of the ES at time t, and the time interval Δt.

$$E_{t+1}^{ES}=E_{t}^{ES}-(P_{t}^{ES}+P_{t}^{ES,Loss})\Delta t \tag{4.13}$$

where E_t^{ES} and E_{t+1}^{ES} represent the stored energy in the ES at the time $t/t+1$;

The State of Charge (SoC) of an energy storage system quantifies the available energy as a percentage of the total capacity, serving as an indicator of its current charge level, typically between 0% (completely discharged) and 100% (fully charged) [153]. To enhance lifespan, the energy storage seldom charges or discharges to its full capacity. The upper limit is often set between 80% to 95% to prevent overcharging, while a lower limit is set between 5% to 20% to avoid deep discharges which are also detrimental to lifespan longevity [154]. Therefore, in all cases of this paper, constraint (4.14) limits SoC level between 10% to 90%.

$$\underline{E^{ES}} \leq E_t^{ES} \leq \overline{E^{ES}} \tag{4.14}$$

where $\underline{E^{ES}}$ and $\overline{E^{ES}}$ are the lower/upper limit of the stored energy in the ES.

Constraint (4.15) defines that the initial SoC and final SoC are kept constant.

$$E_{t=T}^{ES} = E_{t=0}^{ES} \tag{4.15}$$

The power loss of the ES is calculated in (4.16).

$$P_t^{ES,Loss} = A^{ES} P_t^{ES} \tag{4.16}$$

where A^{ES} is the power loss coefficient of the ES.

4.3 Optimal Operation Problem Formulation for Three-Phase Four-Wire Unbalanced Active Distribution Networks

In optimisation modelling, to analyse a power network, the methodology of Kron reduction (KR) is applied to replace the 3P4W system with three-phase conductor nodes but with the same terminal behaviour of voltages and currents at target vertices [155]. In practice, three-order Z and Y matrices are provided in standard IEEE PES feeders for 3P4W systems [156].

4.3.1 Objective Function

In optimisation problems, the multi-objective optimisation (MOO) [157,158] and the weighted sum method (WSM) [159] exhibit distinct approaches and outcomes in managing multiple objectives. The MOO identifies a range of solutions showing trade-offs between objectives, without prioritising any. In contrast, the WSM simplifies by combining objectives into one, using assigned weights to reflect their importance. MOO offers a comprehensive overview of potential solutions, whereas WSM, through careful weighting, can effectively capture priorities and facilitate optimal decision-making.

In this research, as both the total power loss and the voltage imbalance conditions are considered simultaneously, the WSM is utilised in the optimisation. Therefore, a weighted combination of minimising total power losses and mitigating the voltage imbalance condition is proposed as the objective function, as derived in (4.17). Different combinations of weight coefficients will be applied and compared in the case studies to draw up the relationship between these two parameters and the two objectives.

$$min f = W_L f^L + W_U f^V \tag{4.17}$$

where W_L is the weight coefficient of the total power losses; W_U is the weight coefficient of the voltage imbalance condition; the total power losses f^L and the voltage imbalance condition f^V are formulated as follows.

$$f^L = \sum_{t=1}^{24} \sum_{i=1}^{N} \sum_{\varphi=a}^{c} Re\left(Z_{ij} I_{ij,t}^2\right) + \sum_{t=1}^{24} P_{SOP,t}^{Loss} \tag{4.18}$$

$$f^V = \sum_{t=1}^{24} \sum_{i=1}^{N} \sum_{\varphi=a}^{c} \left| V_{i,t}^{\varphi} - \frac{V_{i,t}^{a} + V_{i,t}^{b} + V_{i,t}^{c}}{3} \right| \tag{4.19}$$

where Z_{ij} is the line impedance of branch ij; $I_{ij,t}$ is the line current vector of branch ij; $P_{SOP,t}^{Loss}$ is the total power losses of SOPs; $V_{i,t}^{a}$, $V_{i,t}^{b}$ and $V_{i,t}^{c}$ are the voltages on phases a, b and c of node i at time t; $V_{i,t}^{\varphi}$ is the voltage on phase φ of node i at time t.

The weight coefficients W_L and W_U are derived as follows.

$$W_L = \frac{\rho_L}{f_{Original}^{L}} \tag{4.20}$$

$$W_U = \frac{\rho_V}{f_{Original}^{V}} \tag{4.21}$$

$$\rho_L + \rho_V = 1 \tag{4.22}$$

where ρ_L and ρ_V are the weight indexes of the power loss objective and the voltage imbalance condition objective respectively; $f_{Original}^{L}$ and $f_{Original}^{V}$ are the values of f^L and f^V in the original network before optimisation. The sum of ρ_L and ρ_V is always one [160].

4.3.2 Three-Phase Four-Wire System Operational Constraints

The nodal voltage vectors and the related second-order decision variables are defined as follows.

$$V_{i,t} = \left[V_{i,t}^{a}, V_{i,t}^{b}, V_{i,t}^{c}\right]^T \tag{4.23}$$

$$v_{i,t} = V_{i,t} V_{i,t}^{H} \tag{4.24}$$

where the superscript H represents the Hermitian transpose; $V_{i,t}$ is the voltage vector of node i at time t; $V_{i,t}^{a}$, $V_{i,t}^{b}$ and $V_{i,t}^{c}$ are the voltages on phase A, B and C of node i at time t, separately; $v_{i,t}$ represents the second-order decision variable of the voltage on node i at time t.

Similarly, the vectors of line current and power and the related second-order decision variables are described as follows.

$$I_{ij,t} = \left[I^a_{ij,t}, I^b_{ij,t}, I^c_{ij,t} \right]^T \tag{4.25}$$

$$l_{ij,t} = I_{ij,t} I^H_{ij,t} \tag{4.26}$$

$$S_{ij,t} = V_{i,t} I^H_{ij,t} \tag{4.27}$$

where $I_{ij,t}$ is the current vector of branch ij at time t; $I^a_{ij,t}$, $I^b_{ij,t}$, and $I^c_{ij,t}$ are currents on phases a, b, and c of branch ij at time t, respectively; $l_{ij,t}$ is the second-order decision variable of the current on branch ij at time t; $S_{ij,t}$ is the second-order decision variable of power from node i to node j at time t.

The power flow balance constraint can be given as follows.

$$\sum diag\left(S_{ij,t} - Z_{ij} l_{ij,t}\right) + s_{j,t} + y_{j,t} v_{j,t} = \sum diag\left(S_{jk,t}\right) \tag{4.28}$$

where $s_{j,t}$ is the nodal injection at node j at time t; Z_{ij} is the line impedance of branch ij; $y_{j,t}$ is the nodal shunt capacitance; $v_{j,t}$ is the second-order decision variable of voltage at node j at time t; $S_{jk,t}$ represents the downstream power flows from node j at time t.

Equation (4.29) is derived from Kirchhoff's Voltage Law along the line ij. Equation (4.30) represents the lower and upper limits of the nodal voltage in the network and the voltage at the source node of the network is defined in (4.31).

$$v_{j,t} = v_{i,t} - \left(S_{ij,t} Z^H_{ij} + S^H_{ij,t} Z_{ij}\right) + Z_{ij} l_{ij,t} Z^H_{ij} \tag{4.29}$$

$$\underline{v_i} \leq diag\left(v_{i,t}\right) \leq \overline{v_i} \tag{4.30}$$

$$v_0 = V_0^{ref} \left(V_0^{ref} \right)^H \tag{4.31}$$

where the superscript H indicates the Hermitian transpose. $\underline{v_i}$ and $\overline{v_i}$ represent the lower and upper limits of voltage at node i respectively; V_0^{ref} is the nodal voltage vector at the source node; v_0 is the second-order decision variable at the source node.

In the power distribution grid, the step-voltage regulators, fundamentally functioning as tap-changing transformers, are routinely installed and employed to Keep the system voltages within the required ranges. When considering three single-phase step-voltage regulators positioned at a three-phase bus, the rated voltage ratios, between the primary side and the secondary side of the step-voltage regulators, can be presented as followings.

$$ratio = [r_a, r_b, r_c]^T \tag{4.32}$$

$$\left[V_{sec,t}^a, V_{sec,t}^b, V_{sec,t}^c\right]^T = \left[r_a V_{pri,t}^a, r_b V_{pri,t}^b, r_c V_{pri,t}^c\right]^T \tag{4.33}$$

$$r_a = 1 + 0.00625 \times Tap_a \tag{4.34}$$

$$r_b = 1 + 0.00625 \times Tap_b \tag{4.35}$$

$$r_c = 1 + 0.00625 \times Tap_c \tag{4.36}$$

where, $V_{pri,t}^a$, $V_{pri,t}^b$ and $V_{pri,t}^c$ are the voltage on phase A, B and C of the primary side of the step-voltage regulators at time t, respectively; $V_{sec,t}^a$, $V_{sec,t}^b$ and $V_{sec,t}^c$ are the voltage on phase A, B and C of the secondary side of the step-voltage regulators at time t, separately; r_a, r_b and r_c and the individual voltage ratios on phase A, B and C of the step-voltage regulators; Tap_a, Tap_b and Tap_c are the integers, typically between -16 and 16, for the phase A, B and C of the step-voltage regulators.

When the impedance of the step-voltage regulator is taken into consideration, the voltage relationship between the primary side and the secondary side of a regulator can be defined as follows.

$$v_{sec}^{abc} = \left(v_{pri}^{abc} - \left(S_{re} z_{re}^{H} + S_{re}^{H} z_{re} \right) + z_{re} l_{re} z_{re}^{H} \right) \times R \tag{4.37}$$

$$R = ratio \times ratio^{T} \tag{4.38}$$

where z_{re} is the impedance of the voltage regulator; v_{pri}^{abc} and v_{sec}^{abc} are the second-order variables of the primary voltage and the second voltage of the regulators respectively; l_{re} is the second-order variables of current of regulator; S_{re} is the power flowing through the regulator.

4.3.3 Distributed Generation Operational Constraints

Constraint (4.39) defines that the active power output of a distributed generation (DG) unit is equal to the given reference value. The reactive power output of a DG unit is expressed in (4.40) and the capacity constraint is (4.41).

$$P_{\varphi,i}^{DG} = P_{\varphi,i}^{DG,\ ref} \tag{4.39}$$

$$Q_{\varphi,i}^{DG} = P_{\varphi,i}^{DG} \tan\left(\theta_{\varphi,i}^{DG} \right) \tag{4.40}$$

$$\sqrt{\left(P_{\varphi,i}^{DG} \right)^{2} + \left(Q_{\varphi,i}^{DG} \right)^{2}} \leq S_{\varphi,i}^{DG} \tag{4.41}$$

where $P_{\varphi,i}^{DG,ref}$ is the given active power generated by DG on phase φ at node i; $P_{\varphi,i}^{DG}$, $Q_{\varphi,i}^{DG}$ are the active/reactive power output of DG on phase φ at node i; $\theta_{\varphi,i}^{DG}$ is the power factor angle of DG on phase φ at node i; $S_{\varphi,i}^{DG}$ is the capacity of DG installed on phase φat node i.

4.4 Modelling and Algorithm Process of Symmetrical Semidefinite Programming

All constraints listed above require conversion to the symmetrical SDP model.

4.4.1 System Operational Constraints

The three-phase system can be decoupled by the symmetrical component transformation, which has been proved in [85]. As a result, the three-phase voltages as the phase components are converted into symmetrical components as follows:

$$V_{i,t}^{abc} = AV_{i,t}^{012} \tag{4.42}$$

$$A = \begin{bmatrix} 1 & 1 & 1 \\ 1 & a^2 & a \\ 1 & a & a^2 \end{bmatrix}, \; A^H = A^{-1} \tag{4.43}$$

where the superscript *abc* represents the phase components; the superscript 012 indicates the symmetrical components; $a = 1\angle 120$.

Then, three-phase variables and impedance parameters can be described in the form of symmetrical components.

$$v_{i,t}^{abc} = V_{i,t}^{ABC} V_{i,t}^{ABC,H} = AV_{i,t}^{012} \left(AV_{i,t}^{012}\right)^H = Av_{i,t}^{012} A^H \tag{4.44}$$

$$l_{i,t}^{abc} = Al_{i,t}^{012} A^H \tag{4.45}$$

$$S^{abc}_{i,t} = AS^{012}_{i,t}A^{H} \tag{4.46}$$

$$z^{abc}_{i,t} = Az^{012}_{i,t}A^{H} \tag{4.47}$$

$$y^{abc}_{i,t} = Ay^{012}_{i,t}A^{H} \tag{4.48}$$

The power loss function and the power flow constraints can be transformed as follows.

$$f^{L} = \sum diag(A(l^{012}_{i,t} z^{012}_{i,t})A^{H}) + \sum P^{Loss}_{SOP} \tag{4.49}$$

$$\sum diag\left(A\left(S^{012}_{ij,t} - z^{012}_{ij,t} l^{012}_{ij,t}\right) A^{H}\right) + s_{j,t} + y^{012}_{i,t} v^{012}_{i,t} = \sum diag\left(AS^{012}_{jk,t}A^{H}\right) \tag{4.50}$$

$$v^{012}_{j,t} = v^{012}_{i,t} - \left(S^{012}_{ij,t} z^{012,H}_{ij,t} + S^{012,H}_{ij,t} z^{012}_{ij,t}\right) + z^{012}_{ij,t} l^{012}_{ij,t} z^{012,H}_{ij,t} \tag{4.51}$$

$$\underline{v_i} \leq diag(Av^{012}_{i,t}A^{H}) \leq \overline{v_i} \tag{4.52}$$

$$v^{012}_{0} = V^{012,ref}_{0} (V^{012,ref}_{0})^{H} \tag{4.53}$$

$$\begin{bmatrix} v^{012}_{i} & S^{012}_{ij} \\ S^{012,H}_{ij} & l^{012}_{ij} \end{bmatrix} \succcurlyeq 0 \quad i \rightarrow j \tag{4.54}$$

For all three-phase nodes which are connected with single-phase or two-phase feeders, the second-order decision variable in (4.55) is introduced to convert symmetrical component variables back to phase component variables.

$$v^{abc}_{i,t} = Av^{012}_{i,t}A^{H} \tag{4.55}$$

In terms of the symmetrical components, the constraint for the step-voltage regulator becomes:

$$v_{sec}^{012} = \left(v_{pri}^{012} - \left(S_{re}^{012} z_{re}^{012,H} + S_{re}^{012,H} z_{re}^{012}\right) + z_{re}^{012} l_{re}^{012} z_{012,re}^{H}\right) \times R \tag{4.56}$$

4.4.2 SOP Constraints

As the constraints of SOPs (4.1)-(4.16) must be converted into the symmetrical SDP model for optimization, (4.57)-(4.60) are derived to fulfil that.

$$\begin{bmatrix} \frac{S_{SOP}^{Capacity,\ i}}{3} & P_{SOP}^{\varphi,i,t} + jQ_{SOP}^{\varphi,i,t} \\ P_{SOP}^{\varphi,i,t} - jQ_{SOP}^{\varphi,i,t} & \frac{S_{SOP}^{Capacity,\ i}}{3} \end{bmatrix} \succcurlyeq 0 \tag{4.57}$$

$$\begin{bmatrix} \frac{S_{SOP}^{Capacity,j}}{3} & P_{SOP}^{\varphi,j,t} + jQ_{SOP}^{\varphi,j,t} \\ P_{SOP}^{\varphi,j,t} - jQ_{SOP}^{\varphi,j,t} & \frac{S_{SOP}^{Capacity,j}}{3} \end{bmatrix} \succcurlyeq 0 \tag{4.58}$$

$$\begin{bmatrix} P_{SOP,\ Loss}^{\varphi,i,t}/A_{SOP} & P_{SOP}^{\varphi,i,t} + jQ_{SOP}^{\varphi,i,t} \\ P_{SOP}^{\varphi,i,t} - jQ_{SOP}^{\varphi,i} & P_{SOP,\ Loss}^{\varphi,i,t}/A_{SOP} \end{bmatrix} \succcurlyeq 0 \tag{4.59}$$

$$\begin{bmatrix} P_{SOP,\ Loss}^{\varphi,j,t}/A_{SOP} & P_{SOP}^{\varphi,j,t} + jQ_{SOP}^{\varphi,j,t} \\ P_{SOP}^{\varphi,j,t} - jQ_{SOP}^{\varphi,j,t} & P_{SOP,\ Loss}^{\varphi,j,t}/A_{SOP} \end{bmatrix} \succcurlyeq 0 \tag{4.60}$$

4.4.3 DG Constraints

The capacity constraint of DG is also converted into the symmetrical SDP model.

$$\begin{bmatrix} S_{\varphi,i}^{DG} & P_{\varphi,i}^{DG} + jQ_{\varphi,i}^{DG} \\ P_{\varphi,i}^{DG} - jQ_{\varphi,i}^{DG} & S_{\varphi,i}^{DG} \end{bmatrix} \succcurlyeq 0 \tag{4.61}$$

4.4.4 Flow Chart of Operational Optimisation

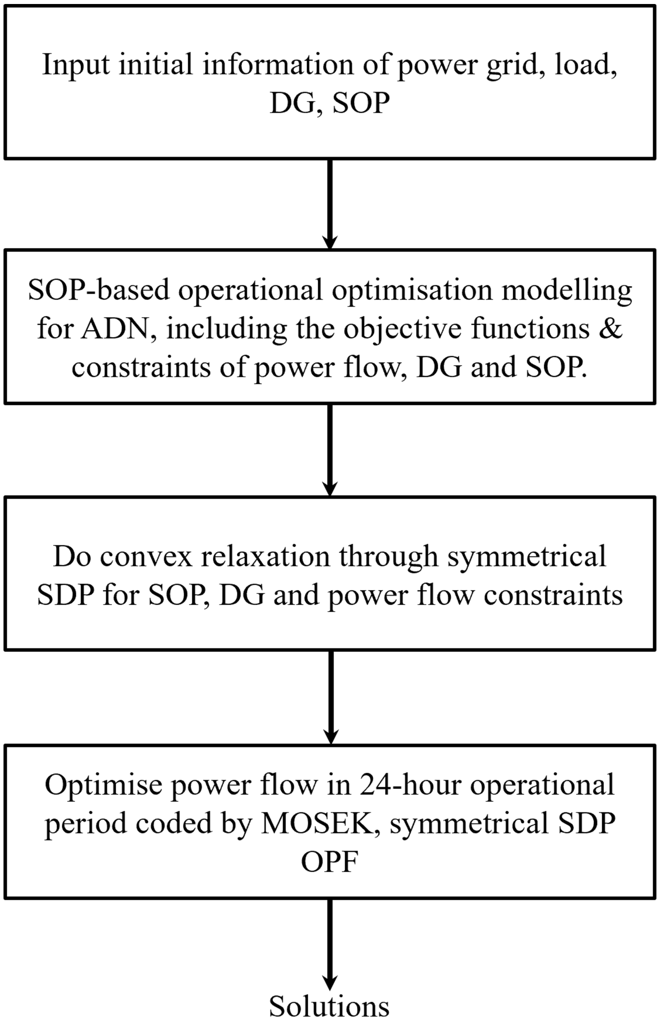

Figure 4.1: Flow Chart of SOP-based Operation Optimisation for ADN

The implementation process of the proposed model is depicted in Figure 4.1. Initially, essential data, including grid parameters, profiles of load and DG, locations and capacities of SOPs, are inputted. Subsequently, the constraints associated with SOPs, DG, and power flow are relaxed using the symmetrical SDP algorithm. This adjustment enables the transformation of the original non-convex optimisation problem into a symmetrical SDP model, which is then solved over a 24-hour simulation period.

A key limitation of the proposed approach is that the optimisation results depend on the initial information inputted. Therefore, future work is required to create further strategies to tackle the stochastic issues caused by the variable outputs of REGs, fluctuating consumer demands and unexpected faults in the power network.

4.5 Case Study

The optimisation program for case studies in this section was coded in YALMIP [161] and solved by MOSEK in MATLAB R2018a, with an operational environment of Windows 10 Intel i7-7700HQ CPU @2.80 GHz, 16.0 GB RAM.

4.5.1 Modified IEEE 123-Node System

In this section, a modified IEEE 123-node test feeder system is used to verify the effectiveness and efficiency of the proposed method, which aims to mitigate the unbalanced condition and minimise the total power losses of the unbalanced ADNs. The rated voltage is 4.16 kV while the minimum and maximum voltage limits are set as 0.95 p.u. and 1.05 p.u., respectively. The total active and reactive power of the loads in the network is 3,490 kW and 1,920 kVar, respectively. The profiles of loads and the PV generation are from [162] and shown in Fig 4.3.

The original system operates under significantly unbalanced loading conditions where branches are asymmetrically configurated and the maximum power differences among three phases can be up to tens of kilowatts [90].

To further investigate additional impacts of imbalance from DG, ten single-phase PV units are integrated into the network and are operated with a constant power factor of 1.0. The location information and the capacity parameters of PV units are from [87] and shown in Table 4.2.

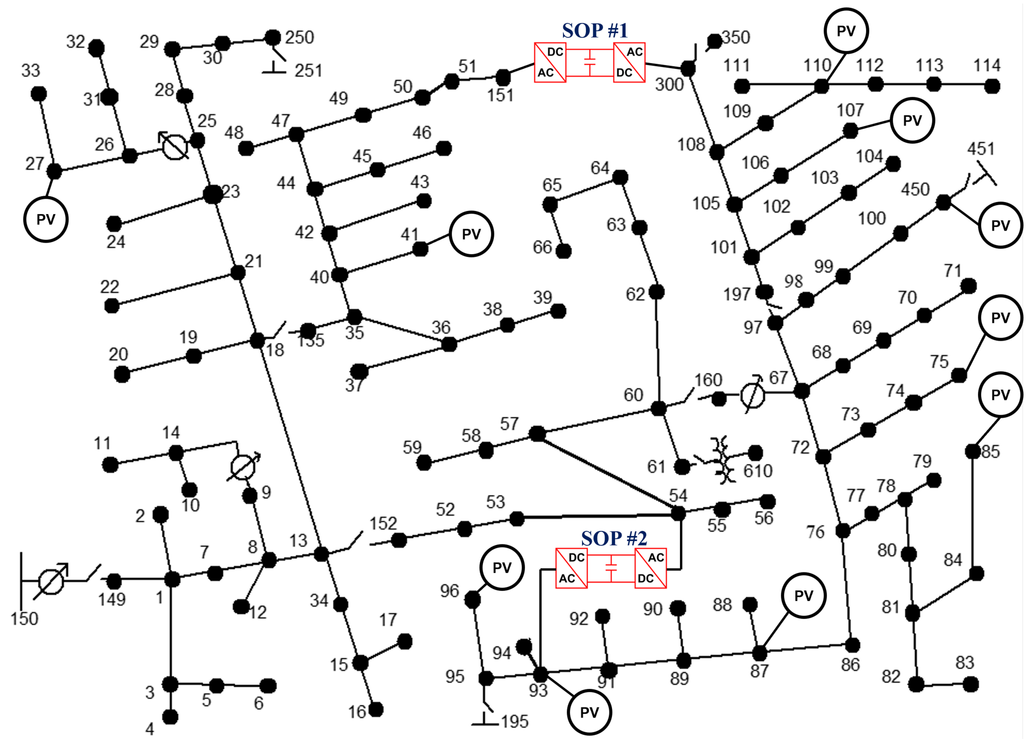

Figure 4.2: Modified IEEE 123-Node System

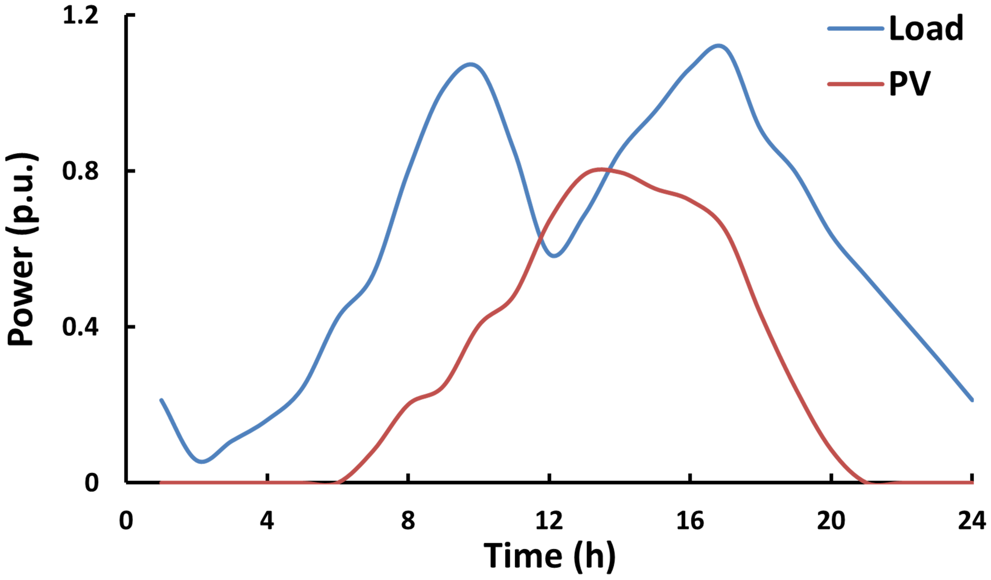

Figure 4.3: Load and Individual PV Generation Profiles [162]

Table 4.2: Parameters of Installed PV Units

PV	1	2	3	4	5	6	7	8	9	10
Location (Node #)	27	41	75	85	87	93	96	107	110	450
Phase Installed	A	C	C	C	B	B	B	B	A	C
Capacity (kVA)	200	200	300	150	300	150	300	150	150	200

Five scenarios are designed to analyse the benefits.

- Scenario I: The original unbalanced system with PV units and without SOPs.
- Scenario II: The system with traditional SOPs.
- Scenario III: The system with one-side ASP-SOPs.
- Scenario IV: The system with two-side ASP-SOPs.
- Scenario V: The system with two-side ASP-SOPs equipped with ES.

Scenario I serves as the baseline, instrumental in understanding the base performance of the ADN and providing a foundational comparison for the impacts of technological integrations in subsequent scenarios. Scenario II is designed to show how the most widely used SOPs can improve the operational efficiency of ADN and to demonstrate the improvements that can be achieved through the implementation of the proposed ASP-SOPs by comparing with the last three scenarios. The purposes of Scenarios III, IV and V are not only to assess the full potential of ASP-SOPs in the system-level power loss reduction and voltage imbalance mitigation, but also to explore the benefits from comprehensive application of ASP-SOP across the system.

Two SOPs are designed and installed in the system. The first is between nodes #151 and #300 and the second is between nodes #54 and #93. The maximum capacity on each phase of SOPs is 500 kVA. The loss coefficient of SOPs is set as 0.02.

In Scenarios II, III and IV, the topology of SOPs is the two-terminal 3P4W-B2B-VSC. In Scenario V, the SOPs are the two-terminal 3P4W-B2B-VSCs with an ES system (1000 kWh) coupled in the DC-link through DC/DC converters.

In Scenario II, the traditional control of the B2B converter is applied to both SOPs, i.e, one side of the SOP is under the V_{dc}/Q control and the other side is under the P/Q control. In Scenario III, one side of the SOP is under the V_{dc}/Q control and the other side is under the ASP control. Because each side of the SOP can be switched between the V_{dc}/Q and the ASP control, four combinations of control schemes, as described in Table 4.3, will be simulated and compared in Scenario III. In Scenarios IV and V, both sides of the SOPs are under the new ASP control.

Table 4.3: Combinations of Controlling for One-Side ASP-SOPs

	SOP #1		**SOP #2**	
COMB	**Node 151**	**Node 300**	**Node 54**	**Node 93**
#1	ASP	Vdc/Q	Vdc/Q	ASP
#2	ASP	Vdc/Q	ASP	Vdc/Q
#3	Vdc/Q	ASP	ASP	Vdc/Q
#4	Vdc/Q	ASP	Vdc/Q	ASP

4.5.2 Optimisation Results and Analysis

In the original unbalanced systems of Scenario I, the total power loss is 1.131 MWh and the imbalance index of voltage is 1380.60. The power losses can be obtained from equation (4.18), while the imbalance index is used to evaluate the voltage imbalance of the whole network and can be calculated from equation (4.19), in which the absolute value of the difference between the phase voltage and the three-phase average voltage will be calculated.

Fig 4.4, 4.5 and 4.6 show the optimised results of Scenarios II, IV, and V, when the combinations of the weight index between the power loss and the voltage imbalance are varying between 0% and 100%. It is shown in Fig 5 (a) that in Scenario II, the power loss drops rapidly when its weight is either below 15% or between 50% and 60%.

According to Fig 4.5 and Fig 4.6, in Scenarios IV and V, compared with all other weight values, the power loss reduces rapidly when its weight is below 20%, while the change slope of the imbalance index is increasingly steep when the weight of power loss is between 80% and 100%. In both scenarios, the result curves of either the power loss or the imbalance index keep a constant changing rate when the weight of power loss is between 20% and 80%, meaning that the optimization results (points on the curve) are evenly distributed in this weight range.

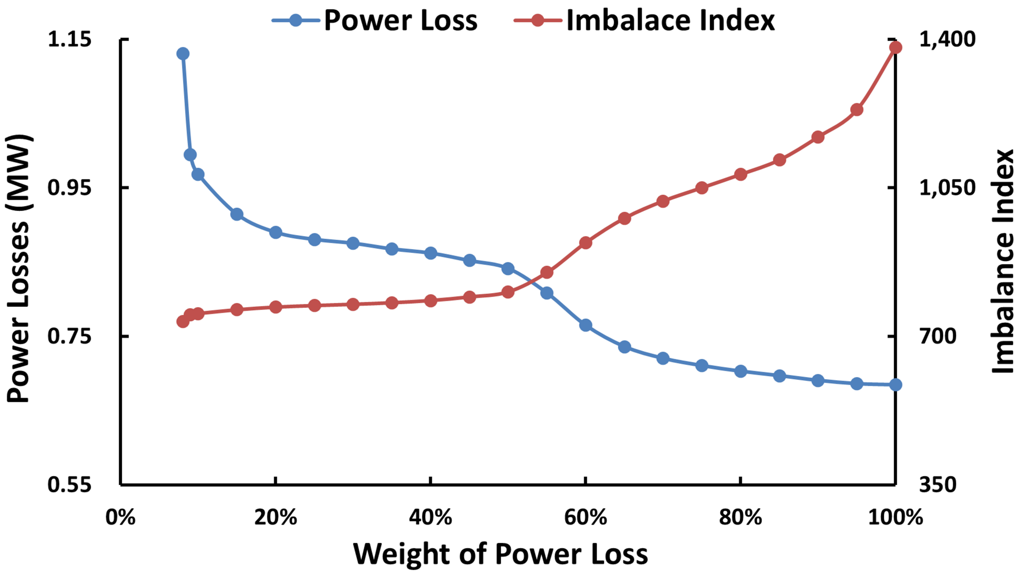

Figure 4.4: Results of Scenario II with SOPs under Conventional Control

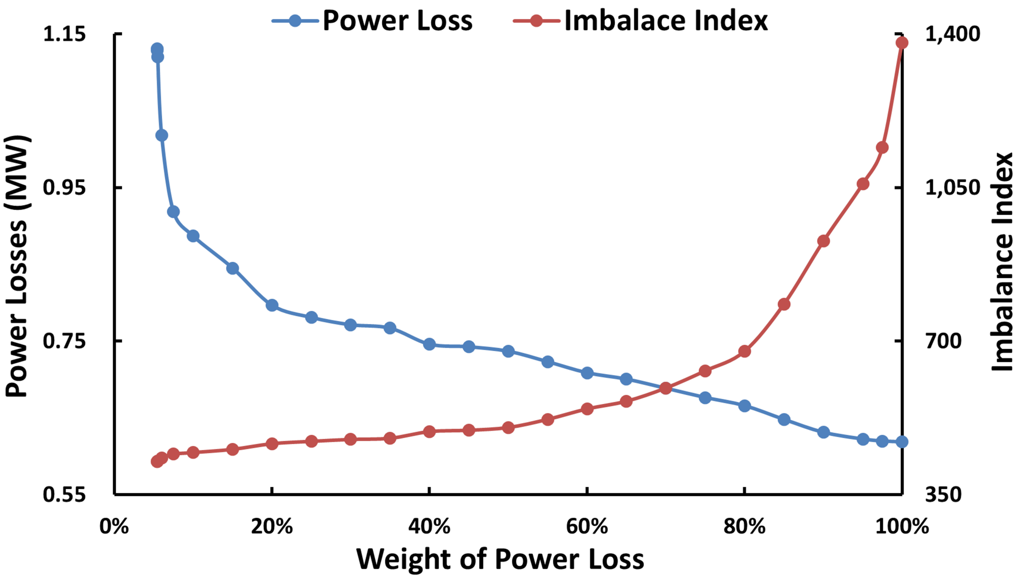

Figure 4.5: Results of Scenario IV with Two-Side ASP-SOPs

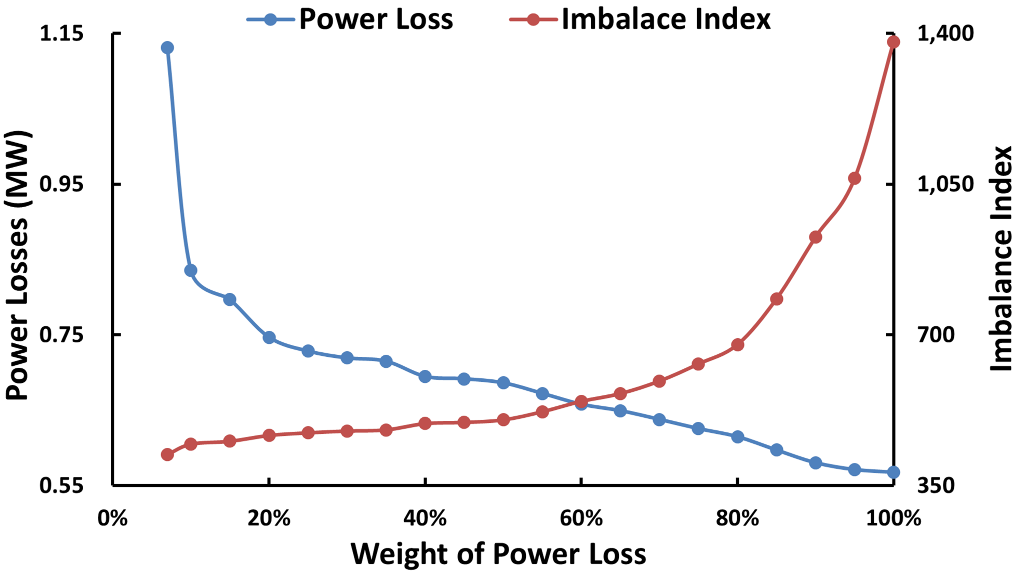

Figure 4.6: Results of Scenario V with Two-Side ASP-SOPs and ESs

Result curves of the four combinations in Scenario III are shown in Fig 4.7. According to these curves, the minimum power losses, from the optimizations for all four control combinations, are almost the same at about 0.63 MW.

However, COMB #3 can achieve the lowest imbalance index (459.434) out of the four combinations. When COMB #3 is applied, the optimization results (points on the curve) are relatively evenly distributed with changes in the weight coefficients of the power loss and the imbalance index. Therefore, COMB #3 is recognized as the optimal choice among all four combinations in Scenario III. Thus, in the rest of the paper, COMB #3 will be used for further analysis.

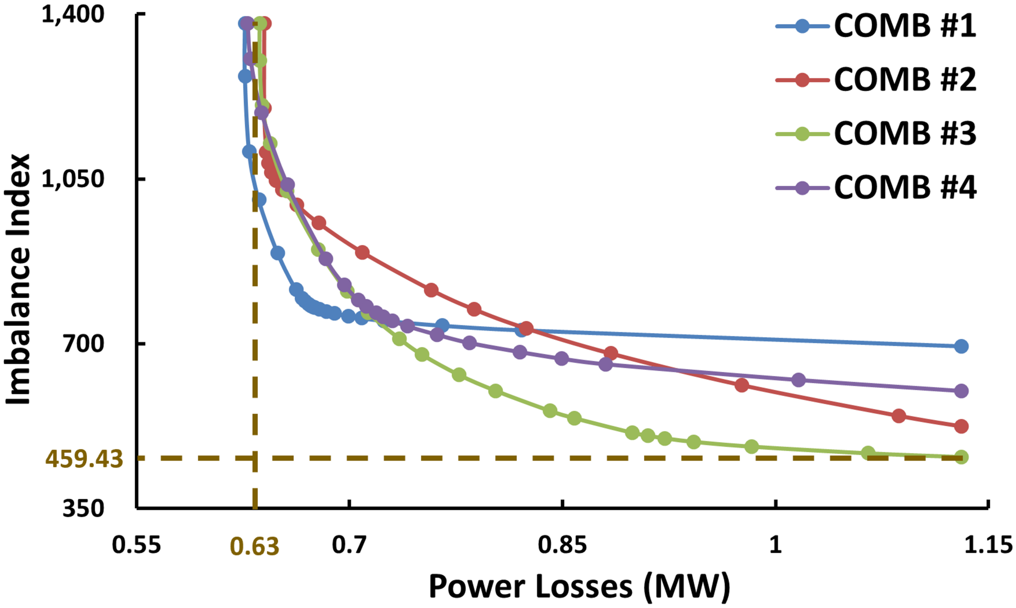

Figure 4.7: Comparison of Control Combinations in Scenario III

In Scenarios II and III, one side of the SOPs is under the same control – V_{dc}/Q, while the other side has a different control which can be the P/Q control or the ASP control. As shown in Fig 4.8, compared to the results of Scenario II, the optimization based on one-side ASP-SOPs in Scenario III obtains less total power losses and a lower imbalance index.

The difference between Scenario III and IV is that in Scenario III, all SOPs are the two-side ASP-SOP. It is shown in Fig 4.8 that the optimised results of Scenario IV have lower power losses and a better-mitigated imbalance index than those of Scenario III.

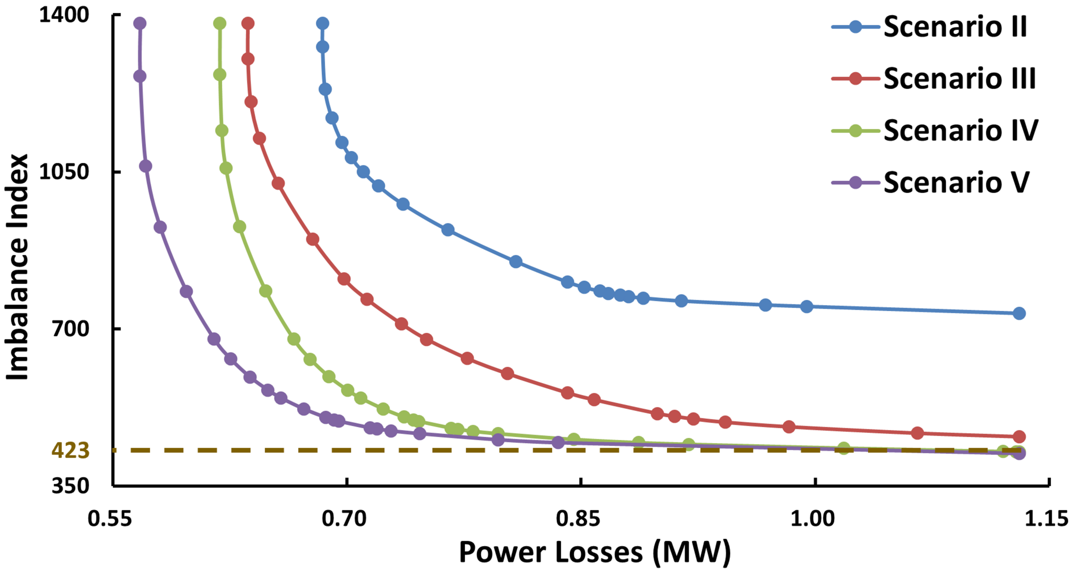

Figure 4.8: Comparison of Optimised Results of Different Scenarios

Above all, from the comparison of Scenarios II, III, and IV, it is demonstrated that the more sides of SOPs are under the ASP control, the better results the optimal operation can achieve. Thus, the benefits of the ASP control, which are the reduction of power losses and the mitigation of imbalance, are proven.

The optimal results in Scenario V have almost the same minimum imbalance index (about 423) as in Scenario IV. However, the power loss reduction in Scenario V is greater than that in Scenario IV, especially when the power loss is below 0.70 MW. This is caused by the integration of the ES system in the DC-link of the SOPs. The integrated ES system can play an important role in reducing power losses of the network, as they fulfill the function of the peak load shaving through optimized charging and discharging operations.

In Table 4.4, for all scenarios, the weight coefficients of the power loss and the voltage imbalance are set as 70% and 30%. It is shown in the comparison of Scenarios I, II, III, and IV that the greater the number of SOP sides that are under the ASP control, the lower total power losses and the less voltage imbalance can be achieved. According to the comparison of

Table 4.4: Comparison of Scenarios under a Set of the Same Weight Coefficient

	Weight of Power Loss: 70%		**Weight of Imbalance Index: 30%**	
Scenario	**Power Loss (MW)**	**Reduction Ratio of Power Loss (%)**	**Imbalance Index**	**Reduction Ratio of Imbalance (%)**
I	1.131	N/A	1380.60	N/A
II	0.720	36.33%	1018.555	26.22%
III	0.713	36.96%	765.646	44.54%
IV	0.689	39.08%	593.205	57.03%
V	0.638	43.61%	592.799	57.06%

Scenarios IV and V results, the same effect on the reduction of imbalance is achieved, while 43.61%-39.08%=4.53% more reduction of the total power losses is accomplished in Scenario V than in Scenario IV, meaning that the ES integrated into the ASP-SOPs in Scenario V can further improve the efficiency of ADNs.

Table 4.5: Comparison of the Optimal Results in Different Scenarios

I	**(Max) Imbalance Index: 1380.60**		**(Max) Power Loss: 1.131 MW**	
Scenario	**Min Power Loss (MW)**	**Max Reduction of Power Loss (%)**	**Min Imbalance Index**	**Max Reduction of Imbalance (%)**
II	0.684	39.48%	734.506	46.80%
III	0.626	44.62%	459.434	66.72%
IV	0.619	45.30%	425.677	69.17%
V	0.567	49.83%	422.156	69.42%

In Table 4.5, one-side ASP-SOPs in Scenario III achieve 44.62%-39.48%=5.1% more maximum reduction of total power losses than traditional SOPs in Scenario II, and 45.30%-44.62% = 0.68% less than two-side ASP-SOPs in Scenario IV. Two-side ASP-SOPs with ES in Scenario V obtain 49.83%-45.30%=4.53% more maximum reduction of total power losses than two-side ASP-SOPs in Scenario IV. For the maximum reduction of imbalance, one-side ASP-SOPs in Scenario III achieve 66.72%-46.80%=19.92% more than transitional SOPs in Scenario II, and 69.17%-66.72%=2.45% less than two-side ASP-SOPs in Scenario IV. Two-side ASP-SOPs with ES in Scenario V (69.17%) obtain almost the same results of the maximum reduction of imbalance as two-side ASP-SOPs in Scenario IV (69.42%).

Similar application benefits of ASP-SOPs are observed through the comparisons in Table IV and Table V that for either the power loss or the voltage imbalance, the more sides of ASP-SOPs that are ASP controlled, the better performance of the optimal operation can be implemented.

4.5.3 Comparison with Published Studies

In order to quantitatively compare with other studies, 4 Scenarios are designed as follows.

- Scenario 1: The ADN operates without SOPs [87].
- Scenario 2: The ADN operates with single-phase SOPs [87].
- Scenario 3: The ADN operates with the phase-to-phase SOPs [163].
- Scenario 4: The ADN operates with the proposed two-side ASP-SOP.

All Scenarios mentioned above are conducted in the IEEE-123-node test system. To fulfil an effective comparison, the optimisation in all Scenarios runs for one same time point, unlike the 24-hour operation in Section A and B. Also, the voltage imbalance (VI) is calculated by (57).

$$\lambda_{VI} = \sum_{i=1}^{N} \left(\frac{|V_{i,-}|^2}{|V_{i,+}|^2} \right) \tag{4.62}$$

where $V_{i,-}$ and $V_{i,+}$ are the negative and positive of the voltage on each node, respectively.

In Scenarios 2, 3, and 4, all the systems are designed and equipped with two SOPs. The first

SOP is installed between nodes 151 and 300, while the second SOP is situated between nodes 54 and 93. Each phase of the SOP has a capacity of 500 kVA, and the loss coefficient is set as 0.02. The comparative analysis of optimisation results for various Scenario, presented in Fig 4.9, demonstrates that in Scenario 4 with the proposed 3P4W-B2B-VSC based two side ASP-SOP, both the network losses and voltage imbalance index in the ADN is further reduced compared to Scenarios 1, 2, and 3. In Scenario 4, the power loss is reduced to 52.91 kW, a 17.24% decrease from 63.93 kW in Scenario 3. Additionally, the voltage imbalance index of Scenario 4 is reduced to 0.081%, a 19.0% decrease from that of Scenario 3.

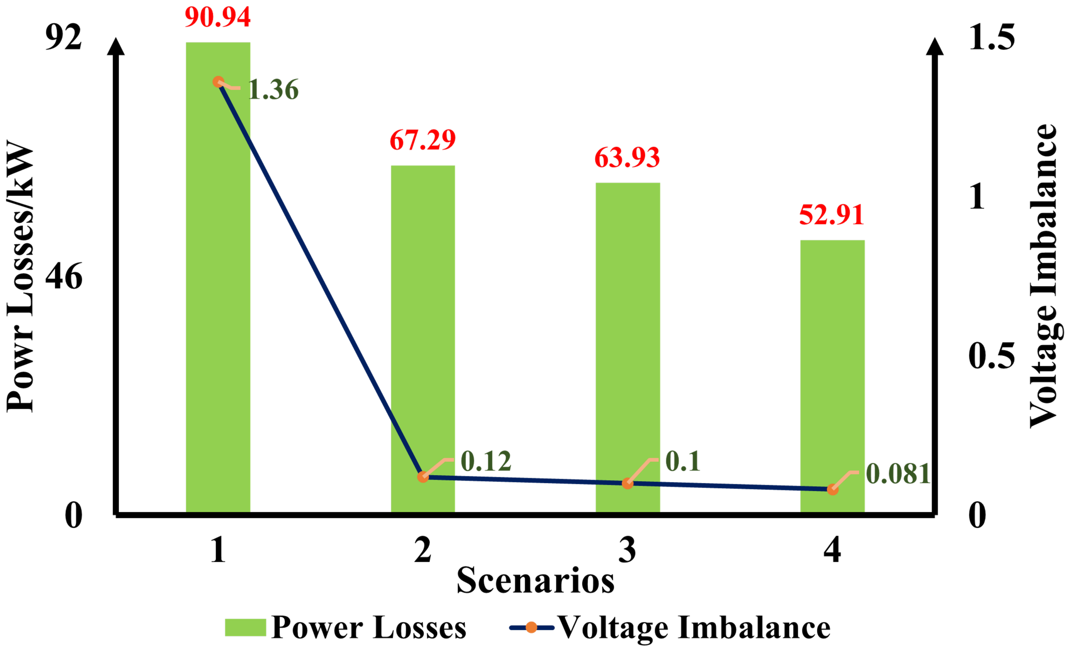

Figure 4.9: Optimal Results of Four Scenarios

Unlike Scenario 4, three single-phase SOPs are employed in Scenario 2, enabling power exchange only between corresponding AC sides of the SOP (i.e., from phase A to phase A, phase B to phase B, and phase C to phase C). In Scenario 3, the phase-to-phase SOPs is used to facilitate power exchange between designated AC phases (i.e., from phase A to phase B, phase B to phase C, and phase C to phase A). In Scenario 4, the proposed two-side ASP-SOP allows each phase on either side of the SOPs to be independently controlled. This capability enables the three phases to individually input or output power at different values. Therefore, the ASP-SOP can flexibly achieve power exchange between the two sides of the SOP compared with three single-phase SOPs and phase-to-phase SOPs.

4.5.4 Operational Performance of ASP-SOPs

Operational Strategies of ASP-SOPs

The operational results of SOPs in Scenarios II, III, IV, and V at hour 12 are shown in Fig 4.10 . In the traditional SOP, shown in Fig 4.10(a), the phase power of the input side (-18.5 kW) is exactly the negative value of the phase power of the output side, because constraint 4.5 determines the total input power is equal to the total output power. Equations 4.6 and 4.7 ensure that all three phases at one terminal of the traditional SOP run at the same power. In the one-side ASP-SOP, presented in Fig 4.10(b), the terminal of Node 151, under the control of Vdc/Q, has the same power for all three phases, while the terminal of Node 300, under the ASP control, has three different power values. In the two-side ASP-SOP, shown in Fig 4.10(c), the phase power can reach nearly 80 kW and the power difference in the same terminal can be almost 100 kW.

In Fig 4.10(d), two dashed red lines indicate the maximum (80) and minimum (-80) y-axis coordinate values of 4.10 (a), (b) and (c), respectively. In the two-side ASP-SOP with ES, presented in 4.10(d), only phase C of the terminal at Node 151 is supplying power, while other phases are absorbing the power from the grid, according to the references from the optimization calculation. The ES is being charged with a power of 322.9 kW. The maximum

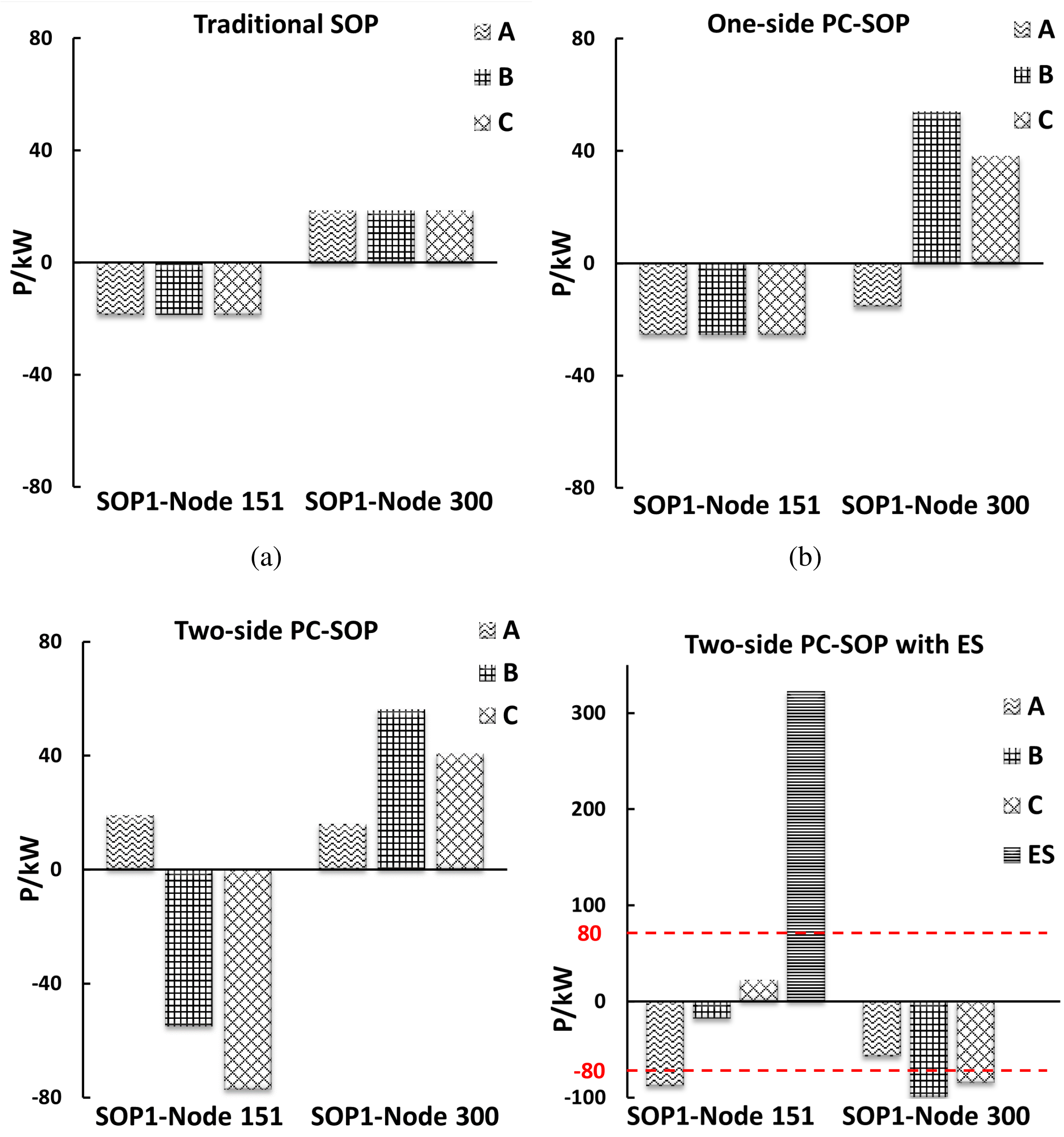

(a) (b)

(c) (d)

Figure 4.10: Operational Strategies (a) Traditional SOP (b) One-Side ASP-SOP (c) Two-Side ASP-SOP (d) Two-Side ASP-SOP with ES

phase power of the two-side ASP-SOP with ES is nearly 100 kW, about 20 kW more than the power (nearly 80 kW) of the two-side ASP-SOP without ES.

As shown from the analysis and the operational performance comparison of these four types of SOP, it is demonstrated that at the same moment and under the same system circumstance, the ASP control can enable more flexible power flows of SOPs.

Power-Electronic Simulation of the ASP-SOP

To demonstrate the effectiveness of the proposed ASP control for the 3P4W-B2B-VSC based two-side ASP-SOP in Scenario IV of Section A, the operational performance of the ASP SOP in the system-level optimisation is validated through the time-domain power electronics simulation.

The operational data at hour 12 of the SOP 2 in Fig 4.2 is applied in this simulation. In Fig 4.11 (a), the terminal #1 refers to Node 54 of the system in Fig 4.2 and the terminal #2 refers to Node 93.

Table 4.6: Parameters of the ASP-SOPs

Parameters	Value
Rated voltage	4.16 kV
DC-link capacitor C	800 μF
DC-link voltage	8 kV
Capacity (each phase)	500 kVA
Filter inductor	10 mH

The test model is established and simulated in Simulink/Matlab 2018a. The parameters of the ASP-SOP device are shown in Table 4.6. The simulation results are shown in Fig 4.11, where (b) is the line-to-line voltages of the system (maximum value: 5.88 kV).

It is demonstrated by the phase current waveforms, in Fig 4.11 (c) and (d), and the phase power values, in (g) and (h), that the current and power in each phase of the ASP-SOP can be regulated independently. It is presented in Fig 4.11 (c) and (d) that the current waveform of every phase of the SOP has a different maximum value. As shown in Fig 4.11 (g), all three

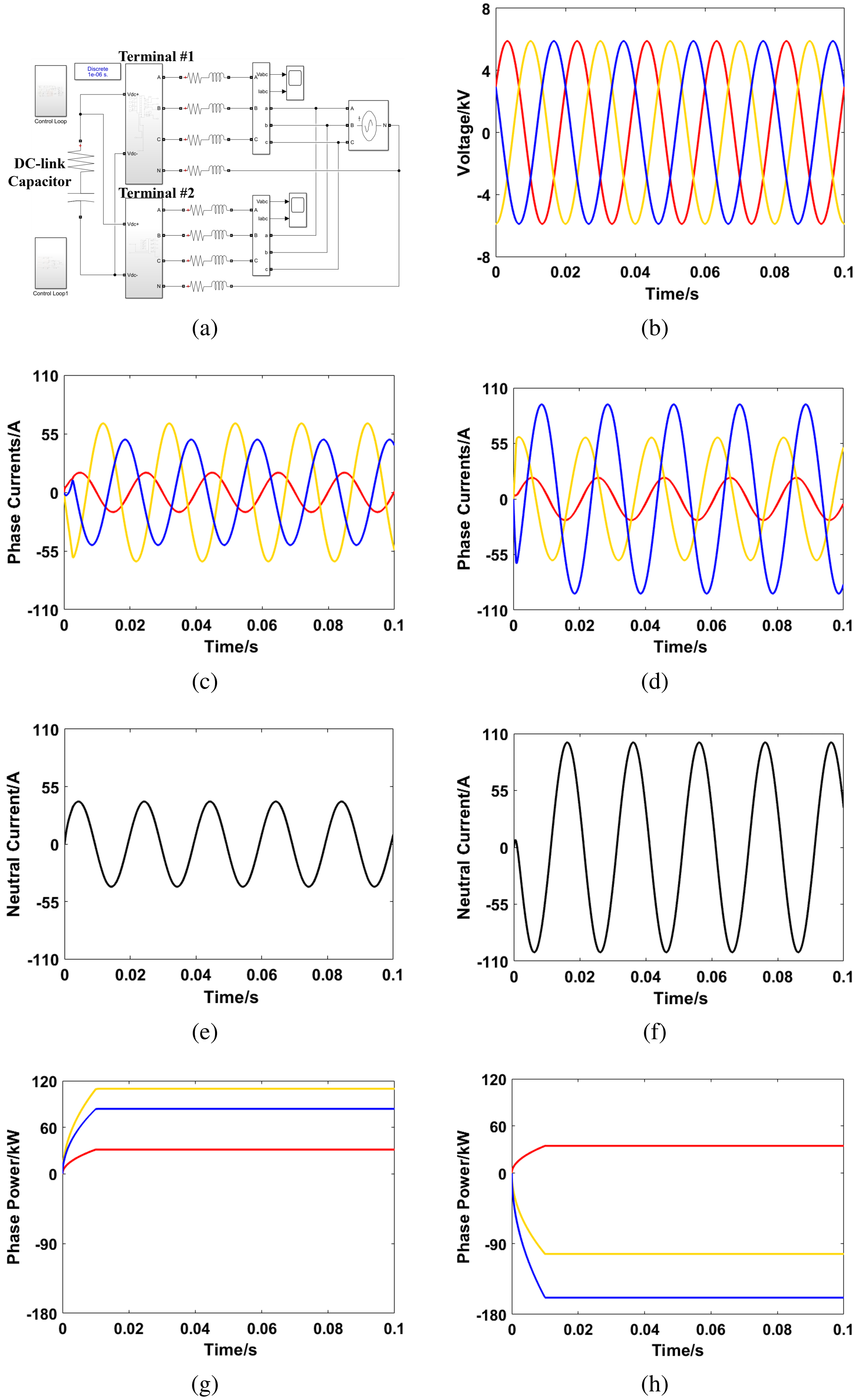

(a) (b)

(c) (d)

(e) (f)

(g) (h)

Figure 4.11: (a) Simulation Model in Matlab/Simulink. (b) Line-to-Line Voltages. (c) Phase Currents at Terminal #1. (d) Phase Currents at Terminal #2. (e) Neutral Line Current at Terminal #1. (f) Neutral Line Current at Terminal #2. (g) Phase Powers at Terminal #1. (h) Phase Powers at Terminal #2.

phases, at terminal #1, release power to the grid: 32.2 kW at phase A (red line), 112.4 kW at phase B (yellow line), and 81.6 kW at phase C (blue line). As shown in Fig 4.11 (h), at terminal #2, phase A releases the power of 38 kW, while phase B and phase C absorb the powers of 110 kW and 154.4 kW respectively.

Meanwhile, in Fig 4.11 (e) and (f), it is shown that the neutral line current of the ASP-SOP is controlled according to the three-phase power at each terminal. The maximum value of the neutral line current at terminal #2 in Fig 4.11 (f) is about twice the one at terminal #1 in Fig 4.11 (e).

Considering the results, it can be concluded that the performance of the proposed ASP-SOPs is greatly improved from traditional SOPs, and the time-domain power-electronic simulation proves their feasibility.

4.5.5 Further Verification in a 380V ADN

As illustrated in Fig 4.12, the performance of the ASP-SOP in a low-voltage ADN is evaluated using a modified 380V three-phase four-wire 21-node system [164, 165].

Modified 21-Node System

This network comprises 21 nodes and a substation transformer, having a total active load power of 247.92 kW and a reactive load power of 81.49 kVA. The PV units, each with a capacity of 20 kW, are installed at nodes 6, 13, 14, 15, and 21. Two 3P4W-B2B-VSC based two side ASP-SOP, with each SOP phase capability of 15 kVA, is incorporated in the network. The profiles of loads and PV, referenced from [165], are detailed in Fig 4.13.

The analysis of the benefits derived from ASP-SOPs is conducted through two scenarios:

- Scenario I: The original system, with the integration of PV units and without the operation of ASP-SOPs.
- Scenario II: The system with two-side ASP-SOPs.

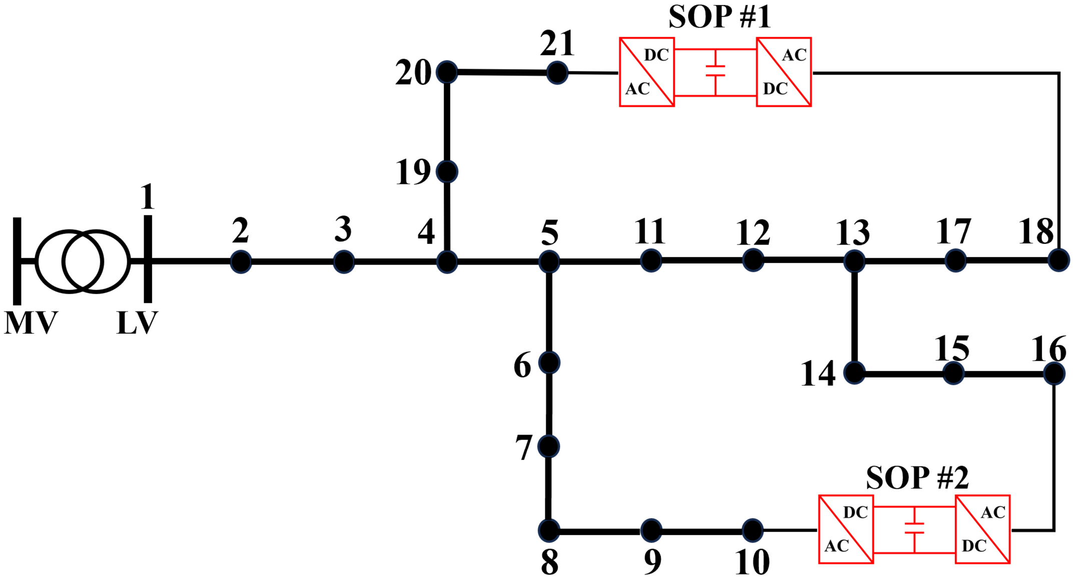

Figure 4.12: 21-Node 380V ADN

Analysis of Optimal Results

In Table 4.7, a notable distinction is observed between Scenarios I and II in the results of power losses and imbalance index. In Scenario I, which serves as a baseline, the value of power losses is 126.18 MWh, and the imbalance index is 43.11. Compared with Scenario I, with the operation of the two-side ASP-SOPs in Scenario II, the value of power losses is reduced to 64.99 MWh, a 48.49% decrease, and the imbalance index plummets from 43.11 in Scenario I to 9.62 in Scenario II, marking a 77.68% decline.

This substantial decrease highlights the effectiveness of ASP-SOP in system-level optimisa-

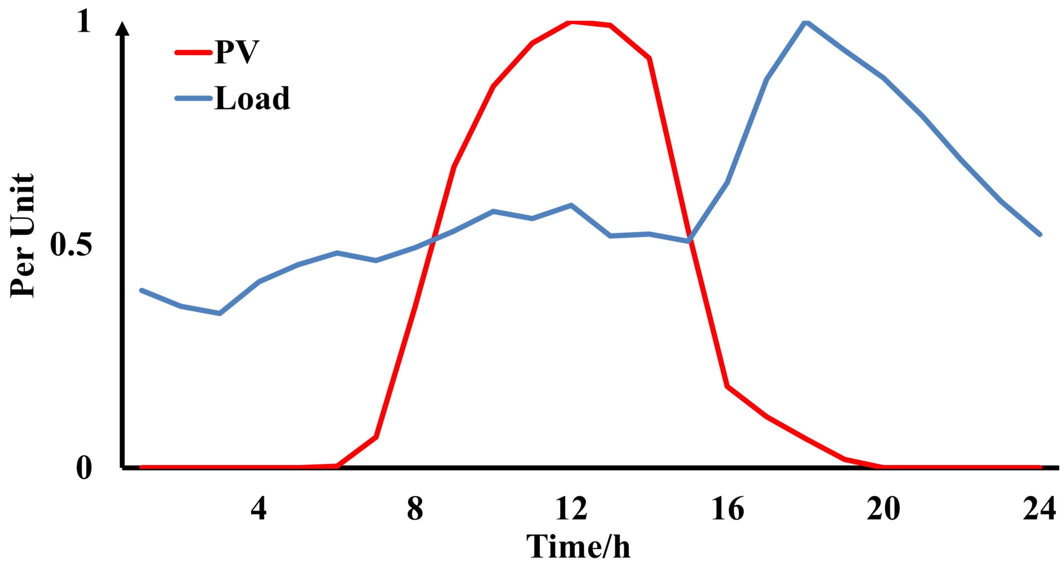

Figure 4.13: Profiles of Loads & PV

Table 4.7: Optimal Results of Two-Side ASP-SOPs for 380V ADN

Scenario	Power Losses /MWh	Reduction /%	Imbalance Index	Reduction /%
I	126.18	N/A	43.11	N/A
II	64.99	48.49%	9,62	77.68

tion optimisation of the 380V ADN. Together with the optimal results in IEEE-123 test node system, it is proven that the proposed ASP-SOP can achieve the optimisation and improvements in power losses and voltage imbalance.

4.5.6 Algorithm Verification and Comparison

To validate the numerical accuracy and computational efficiency of the symmetrical SDP, the optimisation results of the different optimisation algorithms are compared with those of the OpenDSS.

OpenDSS serves as a simulator for electric power distribution systems and its simulation results can be used to verify the accuracy of optimisation outcomes. In simulations, the built-in IEEE-123 node test system package within OpenDSS is employed and further enhanced by integrating models of SOP and PVs. Thus, a comparison can be made between simulation results obtained from OpenDSS and optimisation outputs from other software.

Through Equation (4.63), the absolute percentage of the voltage error, between the optimisation outcomes and the OpenDSS simulations, can be calculated and then compared.

$$Error_v^{\varphi} = \left| \frac{v^{\varphi} - v_{OpenDSS}^{\varphi}}{v_{OpenDSS}^{\varphi}} \right| * 100\% \tag{4.63}$$

where $Error_v^{\varphi}$ represents the voltage error of phase φ; $v_{OpenDSS}^{\varphi}$ denotes the voltage of phase φ in the results of OpenDSS; v^{φ} is the the voltage of phase φ in the optimisation results of various algorithms.

Table 4.8: Comparison of Numerical Accuracy and Solution Time for Different Algorithms

Algorithm (Solver)	**Voltage Error%**			**Solution Time/s**
	Phase A	**Phase B**	**Phase C**	
DC OPF (MOSEK)	12.423	14.033	11.037	12.96
SOCP (MOSEK)	5.923	6.012	4.467	31.87
BFM-SDP (SeDuMi)	1.055	2.422	1.445	219.53
BFM-SDP (MOSEK)	—			
Symmetrical SDP (SeDuMi)	0.014	0.029	0.018	198.71
Symmetrical SDP (MOSEK)	0.014	0.029	0.018	66.93

From the comparative analysis of different algorithms for optimisation, as shown in Table VI, the DC OPF with MOSEK solver and SOCP with MOSEK solver demonstrate lower solution times (32.96s and 51.87s, respectively) but exhibit higher voltage errors. Although DC OPF and SOCP have simpler mathematical mechanisms, making them easier to solve and thus reducing the solution time, DC OPF neglects reactive power, and SOCP overlooks the coupling between three phases, leading to varying degrees of inaccuracy in the optimisation results.

The symmetrical SDP can be solved by either SeDuMi or MOSEK, while the BFM-SDP can only be run under the solver of SeDuMi. Meanwhile, compared to the optimal results of BFM-SDP, the symmetrical SDP can achieve a voltage error of less than 0.1%. For the solution, as the convexification of the symmetrical SDP reduces the solving complexity, the symmetrical SDP is far more efficient than BFM-SDP. This creates possibilities for modelling larger test feeders (e.g. IEEE 8500-node test feeder).

4.6 Conclusions

In this chapter, the phase imbalance mitigation and power loss reduction are the targeted challenges in the operation of ADNs. An operational optimisation strategy based on the ASP-SOP is proposed to minimise both total power losses and the voltage imbalance, considering the integration of single-phase DG, for unbalanced three-phase four-wire ADNs. To achieve the optimal operation of SOPs, the ASP SOP and control strategy are developed with detailed mathematical models. In addition, an innovative application of the symmetrical SDP relaxation method is exploited to convert the three-phase non-convex nonlinear ADN model into a symmetrical SDP model.

To guide the practical operation of DSO, the performance of ASP-SOP in the system-level optimisation can be mutually validated by the time-domain simulations of power electronics devices. Compared with the conventional SOPs, the case study results of the operational optimisation strategy, in the unbalanced ADN of both 380V and 11kV, demonstrate that the ASP-SOP can enable more flexible power flows and achieve optimisation and improvements in both power losses and voltage imbalance.

Chapter 5

Multi-Energy Systems: Operational Coordination of Active Distribution Networks with All-Switching-Phase Soft Open Points and Natural Gas Networks Considering Power-to-Gas

5.1 Introduction

To augment the accommodation of REG and leverage the MES as a pivotal solution, this chapter proposes an operational optimisation strategy for the electricity-gas MES (EGMES). The strategy concentrates on concurrently minimising the total operational costs, the curtailment of installed REG, the voltage imbalance in the three-phase power system, and substantially lowering overall carbon emissions. This model progresses from the ADN framework discussed in the preceding chapter, extending its application to the EGMES context.

In this Chapter, the following work and contributions are presented:

1. A holistic operational coordination optimisation approach is proposed for the electricity and natural gas MES, with bi-directional energy flows through P2G units and GFUs. The closed energy conversion loop formed within the multi-energy systems can trigger the carbon cycle.
2. A comprehensive model is built integrating three-phase unbalanced power systems with natural gas networks. The phase imbalance of the electricity distribution system and the line pack dynamics of the natural gas pipelines are considered simultaneously.
3. The symmetrical SDP method is introduced to convert the above non-convex nonlinear model into an SDP model which commercial solvers can solve.
4. A modified IEEE 123-node power distribution system with a 6-node natural gas network is established. Results with the proposed method achieved minimised total operational cost, reduced curtailment of the installed REG, improved voltage imbalance of the three-phase power system, and lower overall carbon emissions.

5.2 Strategies and Benefits of Electricity and Natural Gas Multi-Energy System

The interdependency between the electric power system and the natural gas network is illustrated in Fig 5.1. The P2G unit produces natural gas from electricity, which means that it serves as a gas source in the natural gas network and as a flexible electric load in the electric power system. The GFU generates electricity from the combustion of natural gas, resulting in it working as a power source in the electric power system and as a gas load in the natural gas network. These two synergies physically link the EGMESs.

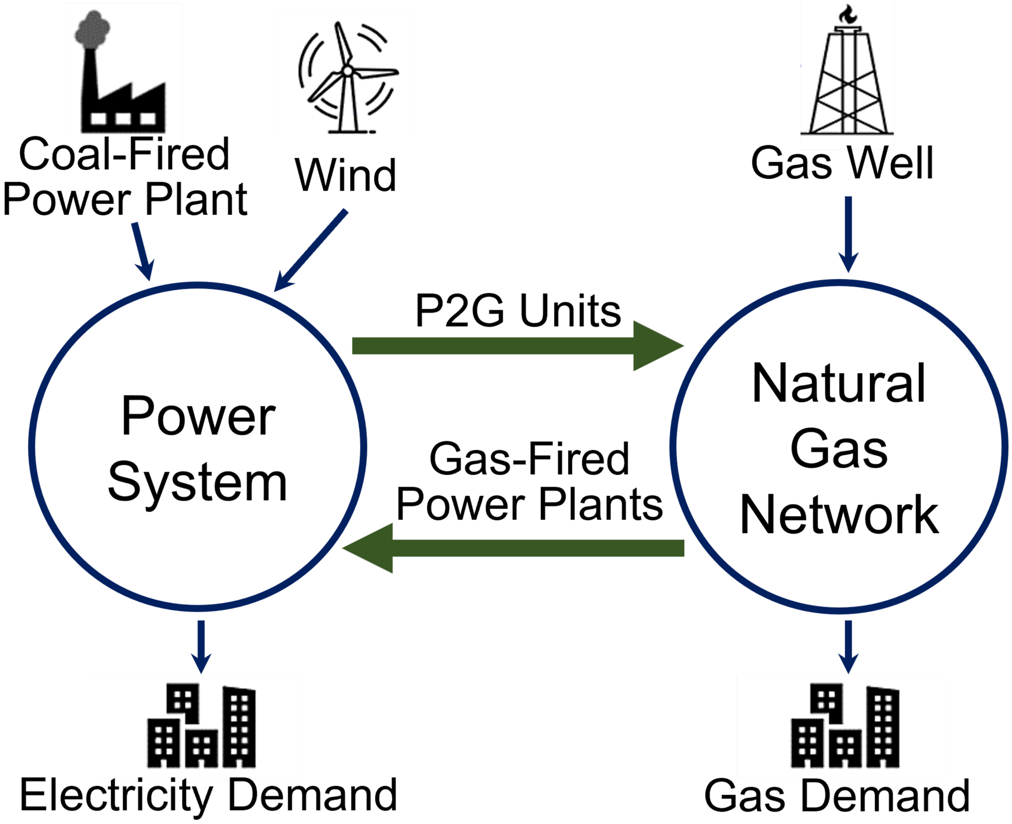

Figure 5.1: Interdependent Electricity and Natural Gas System

The P2G can largely contribute to decarbonising the electricity-gas multi-energy system and improving the integration of REG, as the application of P2G units can fully explore the following advantages of low/negative-carbon technologies [28, 99–103, 166–169].

- Firstly, the existing infrastructure can ensure the utilisation of P2G products. The direct product, hydrogen, is a premium energy source and can be widely used in chemicals, power generation, transportation and fuel cells. Furthermore, the hydrogen can either be injected into the natural gas pipelines within certain limits or be converted into natural gas and then injected into the pipelines. P2G can effectively utilise the capacity of the gas network to mitigate the limitations of the power grid, thereby facilitating the creation of a flexible, multi-energy complementary system.

- Secondly, due to the dynamic line pack of the natural gas pipeline network, P2G units can convert the unused electricity generated from renewable sources into natural gas and store natural gas in pipelines. Thus, the natural gas network can serve as an energy storage system for the electric power system.

- Compared with traditional battery energy storage, P2G units have the advantages of larger storage capacity and higher energy conversion efficiency (60%-70%). As a result, a P2G unit can work as a large-capacity controllable load in the electricity network to consume the excess electricity from REG without being constrained by the capacity of conventional energy storage systems. The produced natural gas from P2G can be directly utilised by natural gas load or GFU. As both the GFUs and the P2G units have fast response characteristics, they can be deployed as coupling points to realise the bidirectional energy flows in integrated electricity-natural gas systems.

5.3 Operational Coordination Problem Formulation of Multi-Energy System

5.3.1 Objective Functions

The proposed operational coordination optimisation aims at minimising the total operational cost F^{Cost}, the curtailment of wind power generation F^{Wind} and the carbon emission F^{C}.

$$F = min\sum_{t=0}^{T}(W_{Cost}F^{Cost} + W_{Wind}F^{Wind} + W_{C}F^{C}) \tag{5.1}$$

$$F^{Cost} = \sum_{t=0}^{T} (C^{grid} P_t^{grid} + \sum_{n=1}^{N} C^{gas} g_{u,t}) \tag{5.2}$$

$$F^{Wind} = \sum_{t=0}^{T} \sum_{k=1}^{K} (P_{k,t}^{Avail} - P_{k,t}^{Wind}) \tag{5.3}$$

$$F^{C} = \sum_{t=0}^{T} (\alpha^{grid} P_t^{grid} + \sum_{n=1}^{N} \alpha^{gas} g_{u,t} - \alpha^{P2G} P_{P2G}) \tag{5.4}$$

where, W_{Cost}, W_{Wind} and W_C are the weight coefficients of three objectives;C^{grid} and C^{gas} are the costs of electricity and natural gas respectively; P_t^{grid} is the electric power from the higher level (upstream) power grid at the time t; $g_{u,t}$ is the natural gas supply of the gas well unit u at the time t; $P_{k,t}^{Avail}$ is the available wind power generation of the wind power unit k at the time t; $P_{k,t}^{Wind}$ is the actual power output of the wind power unit k at the time t.

The weighted sum method (WSM) [159] is utilised in this multi-objective optimisation problem. The weight coefficients W_{Cost}, W_{Wind} and W_C are derived as follows.

$$W_{Cost} = \frac{\rho_{Cost}}{f_{Orig}^{Cost}} \tag{5.5}$$

$$W_{Wind} = \frac{\rho_{Wind}}{f_{Orig}^{Wind}} \tag{5.6}$$

$$W_C = \frac{\rho_C}{f_{Orig}^{C}} \tag{5.7}$$

$$\rho_{Cost} + \rho_{Wind} + \rho_C = 1 \tag{5.8}$$

where f_{Orig}^{Cost}, f_{Orig}^{Wind} and f_{Orig}^{C} are the values of F^{Cost}, F^{Wind} and F^{C} before the optimization; ρ_{Cost}, ρ_{Wind} and ρ_C are the weight indexes of the total operational cost, the curtailed wind power generation and the overall carbon emission respectively. The sum of ρ_{Cost}, ρ_{Wind} and ρ_C should always be one [160].

5.3.2 Three-Phase Power System Constraints

Optimisation modelling involves using the Kron reduction (KR) method to analyse power networks. This method replaces the three-phase four-wire system with three-phase conductor nodes while maintaining the same terminal behaviour of voltages and currents at the desired vertices [155]. In general practices, e.g. Standard IEEE PES test feeders, three-order Z and Y matrices are provided for three-phase four-wire systems [156].

The three-phase power distribution system is taken into account. The power flow balance constraint is in (5.9) and the voltage is described in (5.10) and (5.11). Equation (5.12) defines the voltage at the source node of the network, while the node voltage vectors, branch current vectors, and related second-order decision variables are in (5.13).

$$\sum diag\left(S_{ij,t}-Z_{ij}l_{ij,t}\right)+s_{j,t}+y_{j,t}v_{j,t}=\sum diag\left(S_{jk,t}\right) \tag{5.9}$$

$$v_{j,t}=v_{i,t}-\left(S_{ij,t}Z_{ij}^{H}+S_{ij,t}^{H}Z_{ij}\right)+Z_{ij}l_{ij,t}Z_{ij}^{H} \tag{5.10}$$

$$\underline{v_i}\leq diag\left(v_{i,t}\right)\leq\overline{v_i} \tag{5.11}$$

$$v_0=V_0^{ref}\left(V_0^{ref}\right)^{H} \tag{5.12}$$

$$\begin{cases} V_{i,t}=\begin{bmatrix}V_{i,t}^{a} & V_{i,t}^{b} & V_{i,t}^{c}\end{bmatrix} \\ v_{i,t}=V_{i,t}V_{i,t}^{H} \\ I_{ij,t}=\begin{bmatrix}I_{ij,t}^{a} & I_{ij,t}^{b} & I_{ij,t}^{c}\end{bmatrix} \\ l_{ij,t}=I_{ij,t}I_{ij,t}^{H} \\ S_{ij,t}=V_{i,t}I_{ij,t}^{H} \end{cases} \tag{5.13}$$

where $S_{ij,t}$ is the second-order decision variable of power from node i to node j at time t; $l_{ij,t}$

is the second-order decision variable of current from node i to node j at time t; $s_{j,t}$ is the nodal power injection at node j at time t; $y_{j,t}$ is the nodal shunt admittance; $v_{j,t}$ is the second-order decision variable of voltage at node j at time t; $S_{jk,t}$ represents the downstream power flows from node j at time t. $v_{i,t}$ is the second-order decision variable of voltage at node i at time t; the superscript H indicates the Hermitian transpose. $\underline{v_i}$ and $\overline{v_i}$ represent the lower and upper limits of voltage at node i respectively;V_0^{ref} is the nodal voltage vector at the source node; v_0 is the second-order decision variable at the source node; $V_{i,t}$ is the voltage vector of node i at time t; $I^a_{ij,t}$, $I^b_{ij,t}$, and $I^c_{ij,t}$ are currents on phases a, b, and c of branch ij at time t, respectively.

5.3.3 Natural Gas Network Constraints

The natural gas network is modelled by applying the steady-state natural gas flow model considering the line pack in the pipelines.

The gas supply capacity of the gas well unit μ is imposed as:

$$0 \leq g_{u,t} \leq \bar{g_u} \tag{5.14}$$

where $\bar{g_u}$ is the upper limit of the gas supply.

The pressure at each gas node is described as:

$$\underline{pr_m} \leq pr_{m,t} \leq \overline{pr_m} \tag{5.15}$$

where $pr_{m,t}$ is the pressure of gas node m at time t; $\underline{pr_m}$ and $\overline{pr_m}$ are the lower and upper limits of $pr_{m,t}$ respectively.

In (5.16), the natural gas flow is given by the Weymouth equation. Also, the natural gas flow can be calculated by the average inflow and outflow along a pipeline in (5.17).

$$Q_{m,n,t} = \begin{cases} k_{m,n}\sqrt{{pr_{m,t}}^2 - {pr_{n,t}}^2} & pr_{m,t} \geq pr_{n,t} \\ k_{m,n}\sqrt{{pr_{n,t}}^2 - {pr_{n,t}}^2} & pr_{m,t} < pr_{n,t} \end{cases} \tag{5.16}$$

$$Q_{m,n,t} = \frac{Q^{in}_{m,n,t} + Q^{out}_{m,n,t}}{2} \tag{5.17}$$

where $pr_{n,t}$ is the pressure of gas node n at time t; $k_{m,n}$ is the natural gas flow constant of the pipeline from node m to node n (kcf/psig); $Q_{m,n,t}$ is the natural gas flow in pipeline mn at time t (kcf/h); $Q^{in}_{m,u,t}$ is inflow natural gas flow of pipeline mn at time t; $Q^{out}_{m,u,t}$ is outflow natural gas flow of pipeline mn at time t.

The line pack storage is balanced by the inflow and the outflow of the pipeline in (5.18). Meanwhile, as shown in (5.19), the line pack is related to the pressures at both ends of the pipeline. Constraint (5.20) defines that the initial line pack at the beginning of the optimisation is equal to that at the end of the optimisation.

$$H_{m,n,t} = H_{m,n,(t-1)} + (Q^{in}_{m,n,t} - Q^{out}_{m,n,t}) \tag{5.18}$$

$$H_{m,n,t} = S_{m,n}\frac{pr_{m,t} + pr_{n,t}}{2} \tag{5.19}$$

$$H^0_{m,n} \leq H_{m,n,T} \tag{5.20}$$

where $H_{m,n,t}$ and $H_{m,n,(t-1)}$ are the stored mass of natural gas (line pack) in pipeline mn at time t and $t-1$; $S_{m,n}$ is the line pack constant of pipeline mn. $H^0_{m,n}$ is the initial line pack of pipeline mn; $H_{m,n,T}$ is the line pack of pipeline mn at the end of the planning time period.

5.3.4 Gas-Fired Unit Constraints

The capacity constraint of GFU is shown as (5.21). As the GFUs inject power into the three-phase power system, constraints (5.22) and (5.23) guarantee that the outputs of three phases share the same values of both active power and reactive power.

$$\sqrt{\left(P_{i,t}^{GFU}\right)^2+\left(Q_{i,t}^{GFU}\right)^2} \leq S_i^{GFU} \tag{5.21}$$

$$P_{a,i,t}^{GFU}=P_{b,i,t}^{GFU}=P_{b,i,t}^{GFU} \tag{5.22}$$

$$Q_{a,i,t}^{GFU}=Q_{b,i,t}^{GFU}=Q_{b,i,t}^{GFU} \tag{5.23}$$

where $P_{i,t}^{GFU}$ and $Q_{i,t}^{GFU}$ are the active power and reactive power of GFU at node i at time t respectively.

5.3.5 P2G Unit Constraints

The capacity constraint of the P2G unit is expressed as (5.24). Constraint (5.25) defines the relation between active power input and reactive power input of the P2G unit.

$$\sqrt{\left(P_{i,t}^{P2G}\right)^2+\left(Q_{i,t}^{P2G}\right)^2} \leq S_i^{P2G} \tag{5.24}$$

$$Q_{i,t}^{P2G}=P_{i,t}^{P2G}\tan\left(\theta_{i,t}^{P2G}\right) \tag{5.25}$$

where $P_{i,t}^{P2G}$ and $Q_{i,t}^{P2G}$ are the active power and the reactive power of P2G at node i at time t respectively; S_i^{P2G} is the capacity of power input of P2G; $\theta_{i,t}^{P2G}$ is the power factor of P2G.

As the P2G unit takes the electric energy from the three-phase power system, constraint (5.26) imposes that the power inputs from three phases have the same value. As in (5.27), the natural gas output of P2G is proportional to its active power input.

$$P_{a,i,t}^{P2G} = P_{b,i,t}^{P2G} = P_{b,i,t}^{P2G} = \frac{P_{i,t}^{P2G}}{3} \tag{5.26}$$

$$G_{n,t}^{P2G} = \eta^{P2G} \emptyset^{P2G} P_{i,t}^{P2G} \tag{5.27}$$

where $P_{a,i,t}^{P2G}$, $P_{b,i,t}^{P2G}$ and $P_{b,i,t}^{P2G}$ are the active power of P2G unit in phase a, b and c of node i at time t respectively. $G_{n,t}^{P2G}$ is the natural gas output of P2G at node n of the natural gas network at the time t; $\emptyset^{P2G}$ is the energy conversion factor of natural gas and electric power (kcf/MWh); η^{P2G} is the energy efficiency of P2G.

5.4 Reformulated Constraints for Symmetrical Semidefinite Programming

The constraints listed above require conversion to the symmetrical SDP model.

Unbalanced three-phase systems can be decoupled by the symmetrical component transformation. In (5.28), The three-phase voltages as the phase components are converted into symmetrical components. Then, three-phase variables and impedance parameters can be described in the form of symmetrical components as in (5.29).

$$\begin{cases} v_{i,t}^{abc} = A v_{i,t}^{012} A^H \\ l_{i,t}^{abc} = A l_{i,t}^{012} A^H \\ S_{i,t}^{abc} = A S_{i,t}^{012} A^H \\ z_{i,t}^{abc} = A z_{i,t}^{012} A^H \\ y_{i,t}^{abc} = A y_{i,t}^{012} A^H \end{cases} \tag{5.28}$$

$$A = \begin{bmatrix} 1 & 1 & 1 \\ 1 & a^2 & a \\ 1 & a & a^2 \end{bmatrix}, \ A^H = A^{-1} \tag{5.29}$$

where the superscript *abc* represents the phase components; the superscript 012 indicates the symmetrical components; $a = 1\angle 120$.

Also, the constraints of (5.16), (5.24) and (5.21) must be reformulated into the symmetrical SDP model as followings.

$$\begin{bmatrix} pr_{m,t} - pr_{n,t} & Q_{m,n,t}/k_{m,n} \\ Q_{m,n,t}/k_{m,n} & pr_{m,t} + pr_{n,t} \end{bmatrix} \succcurlyeq 0 \tag{5.30}$$

$$\begin{bmatrix} S_i^{GFU} & P_{i,t}^{GFU} + jQ_{i,t}^{GFU} \\ P_{i,t}^{GFU} - jQ_{i,t}^{GFU} & S_i^{GFU} \end{bmatrix} \succcurlyeq 0 \tag{5.31}$$

$$\begin{bmatrix} S_i^{P2G} & P_{i,t}^{P2G} + jQ_{i,t}^{P2G} \\ P_{i,t}^{P2G} - jQ_{i,t}^{P2G} & S_i^{P2G} \end{bmatrix} \succcurlyeq 0 \tag{5.32}$$

5.5 Case Study

The optimisation program for case studies in this section was coded in YALMIP [161] and solved by MOSEK in MATLAB R2018a, with an operational environment of Windows 10 Intel i7-7700HQ CPU @2.80 GHz, 16.0 GB RAM.

5.5.1 Test Case and Scenarios

As shown in Fig 5.2, a muti-energy system, consisting of a modified IEEE 123-node test feeder power network coupling with a 6-node natural gas network through two GFUs and a P2G device, is built to verify the effectiveness of the proposed method, which aims to minimise the total operational cost, maximise the utilisation of the installed wind power and reduce the overall carbon emissions.

In the electric power network, the rated voltage is 4.16 kV with the minimum and maximum voltage limits set as 0.95 p.u. and 1.05 p.u., respectively. The total active and reactive power of the electric loads in the network are 3,490 kW and 1,920 kVar, respectively [90].

To further investigate the role of P2G in the accommodation of wind power, six wind power units are integrated into the electric power network and operated with a constant power factor of 1.0. Each wind power unit has a capacity of 600 kVA and the location information is shown in Fig 5.2.

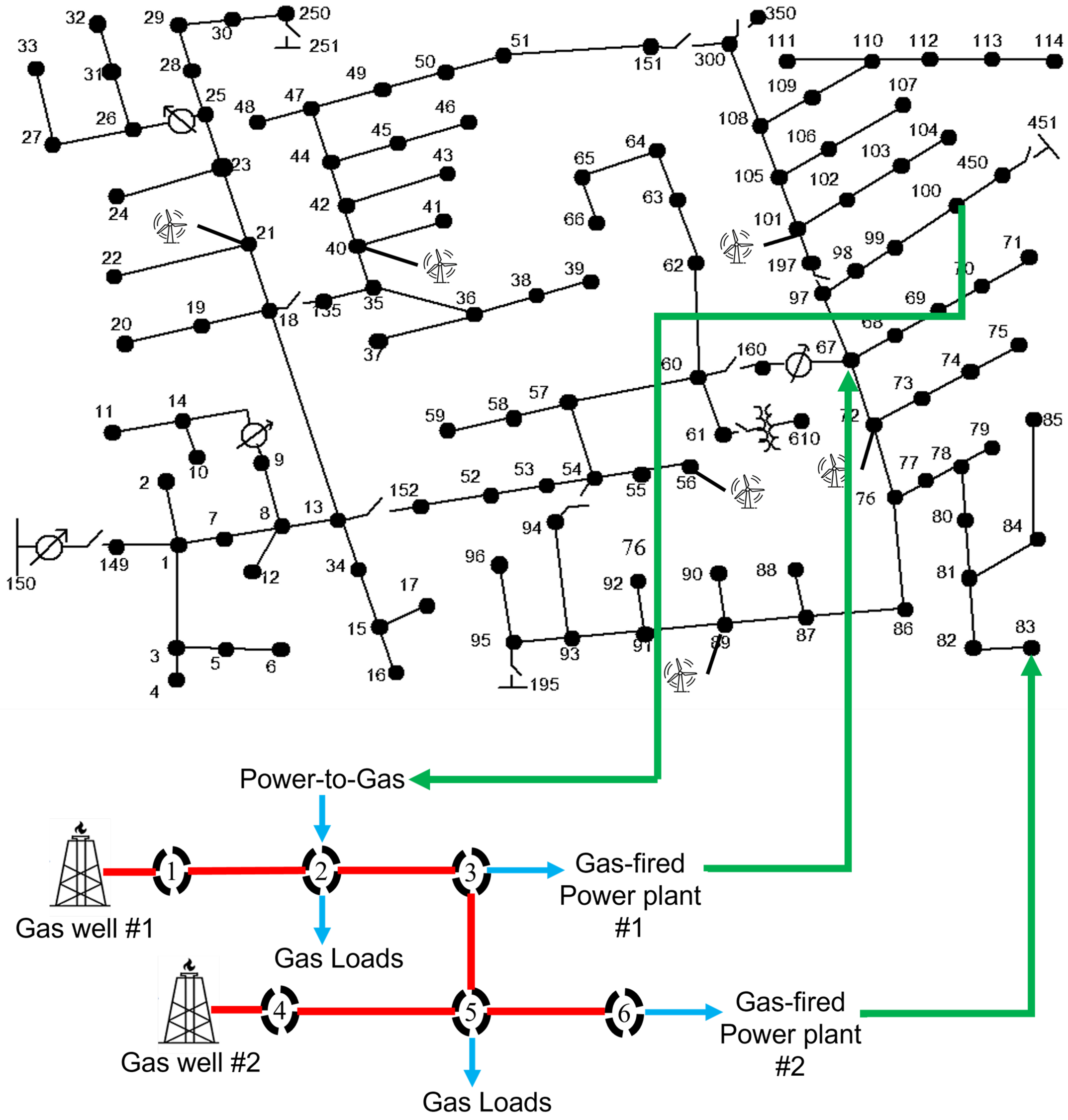

Figure 5.2: Illustration of Multi-Energy System for Case Studies

An essential assumption is that all the power from the upstream power grid (node 150) is generated by coal-fired power plants.

In the natural gas network, natural gas is provided by two gas wells and the P2G device; the gas loads are connected to node 2 and node 5; two GFUs take natural gas as fuel from node 3 and node 6 respectively. The natural gas network is modified from the parameters of [112].

The profiles of electric power loads, natural gas loads and wind power generation are shown in

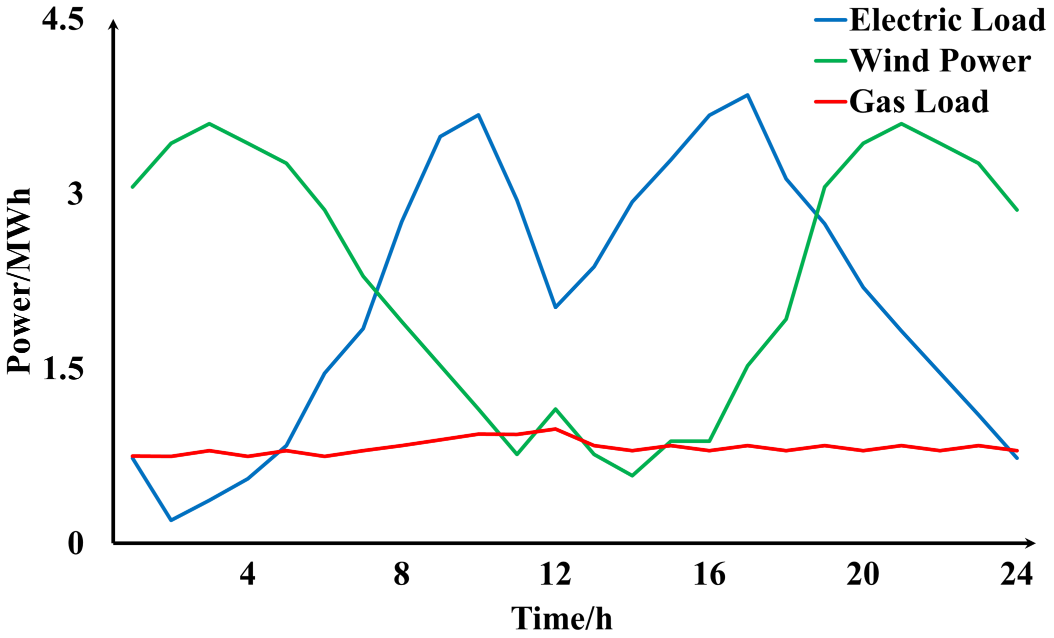

Figure 5.3: Profiles of Electric Loads, Gas Loads and Wind Power Generation

Fig 5.3. The per-unit curve of the electric loads is from [162]. The gas loads' profile is created based on the data of [112]. According to the realistic wind power curves in [170], the wind power output is generated to create the scenario of this case study, where the peak output of wind power occurs at night, whereas the peak electricity demand is during the daytime.

Four scenarios are designed and implemented in the case studies to analyse the benefits of the proposed method. Scenario I is the foundational base case, reflecting the traditional energy management practices, where each system is optimised separately without consideration for potential efficiencies gained from coordination. In Scenario II, the system includes coordinated operations involving GFUs, to explore the initial steps towards the electricity and gas MES by examining the impacts of GFUs through the comparison with the independent operations of Scenario I. Scenario III is designed for the full coordination operation of MES by enabling both GFUs and P2G. This scenario focuses on highlighting the role of P2G technology in the electricity and gas MES. In Scenario IV, following the SOP-based optimisation researched in

Chapter 4 for the operational efficiency of ADNs, the emphasis is on evaluating the impact of the ASP-SOP on enhancing the overall system performance of the MES which comprises ADNs as electric power vectors and the natural gas network.

- Scenario I: Independent operations of the electricity network and the natural gas network; no participation of the GFUs and the P2G device.
- Scenario II: Coordination operation only with the GFUs.
- Scenario III: Coordination operation, considering bidirectional energy flow through the GFUs and the P2G device.
- Scenario IV: Based on Scenario III, the SOP is installed and operated in the electric power network.

In Scenario I, as the coupling components are not operated, the energy flow between the electricity network and the natural gas network does not exist.

In Scenarios II and III, GFU #1 takes natural gas as fuel from node 3 of the natural gas network and injects electricity to node 67 of the electric power network, while GFU #2 takes natural gas as fuel from node 6 of the natural gas network and injects electricity to node 83 of the electric power network. Each GFU has a capacity of 500 kW.

In Scenario III, the P2G device converts the electric power, taken from node 100 of the electricity network, to the natural gas which is injected into node 2 of the natural gas network.

In Scenario IV, two ASP-SOPs are installed in the electric power network. The first is between nodes #151 and #300 and the second is between nodes #54 and #93. The maximum capacity on each phase of SOPs is 500 kVA. The loss coefficient of SOPs is set as 0.02.

5.5.2 Analysis of Optimisation Results

The numerical results of the case studies are shown in Table 5.1 and Table 5.2. The comparison of the results is presented in Fig 5.4.

Table 5.1: Results of Objectives for Scenarios

Scenario	**Operational Cost /$**	**Curtailed Wind Power /MWh**	**Carbon Emission /Tons**
I	1299.14	24.17	16.67
II	1160.39	24.21	12.34
III	1019.85	1.35	11.07
IV	1015.82	1.51	11.01

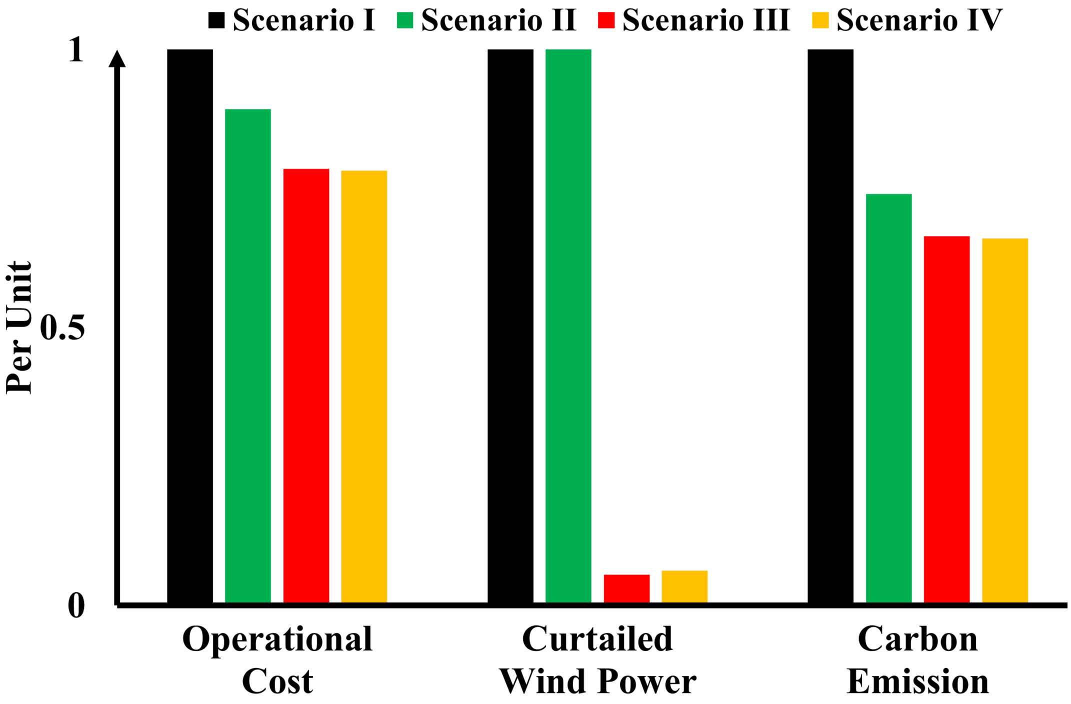

Figure 5.4: Comparison of Optimal Results in Scenarios

In Scenario I, the curtailed wind power generation (24.17 MWh) is up to 44.24% of the available wind power generation (54.63 MWh). The total operational cost is $1299.14 and the overall carbon emission is 16.67 Tons.

In Scenario II, where the GFUs are employed to generate electricity using natural gas, the curtailed wind power, amounting to 24.21 MWh, remains almost unchanged from Scenario I. However, a notable reduction in the total operational cost is observed, decreasing by 10.68% from \$1299.14 in Scenario I to \$1160.39 in Scenario II. Additionally, the overall carbon emissions in Scenario II become lower, showing a 25.96% reduction from 16.67 Tons in Scenario I to 12.34 Tons. This indicates that while the GFUs do not contribute to the increase in the accommodation of wind power, they can play a pivotal role in reducing both operational costs and carbon emissions. This is attributed to the cost-effectiveness and lower environmental impact of natural gas compared to the electric power from the superior power grid. In Scenario III, a marked improvement is obtained in several key areas when compared to Scenarios I and II. Specifically, the curtailment of wind power generation is significantly reduced by 94.40%, illustrating a substantial increase in the utilisation of wind power generation. The total operational cost in Scenario III is also lower, being 21.50% less than in Scenario I and 12.11% less than in Scenario II. Furthermore, the overall carbon emissions in Scenario III show a considerable decrease, being 33.59% lower than in Scenario I and 10.29% lower than in Scenario II. These improvements, especially in the reduction of curtailed wind power, highlight the

Table 5.2: Electricity and Gas Status for Scenarios

Scenario	**I**	**II**	**III**	**IV**
Power from Upper Grids /MWh	21.93	11.02	11.37	11.30
Power Loss of Electric Network /MWh	0.56	0.37	0.65	0.34
Three-Phase Voltage Unbalanced Factor	4.97	4.79	4.67	3.14
Gas Well Output /kcf	67.47	203.13	150.52	150.26
Gas-Fired Units' Output /MWh	N/A	10.72	10.38	10.37
P2G Gas Output /kcf	N/A	N/A	48.29	48.43

significant impact of P2G technology in enhancing the integration of wind power generation.

In Scenario IV, with the engagement of the ASP-SOP, a further refinement over Scenario III is observed, evidenced by the minimal operational costs of $1015.82 and the lowest carbon emissions of 11.01 tons. Despite a slight increase in the curtailed wind power by 0.16 MWh relative to Scenario III, it remains substantially lower than the numbers reported in Scenarios I (24.17 MWh) and II (24.21 MWh).

5.5.3 Technical Benefit Comparison of Three Scenarios from Electricity Profiles

The hourly profiles of electricity in the power distribution network for the three scenarios of the case studies are shown in Fig 5.5, 5.6, 5.7 and 5.8.

In Scenario I, as the electricity network and the natural gas network operate independently, the electricity demand of loads is satisfied by the power from both the upper grids and the generation of wind power in the distribution network. As shown in Fig 5.5, during the hours 1-7 and hours 19-24, all the electric loads are powered by wind power generation, while during the hours 8-18, due to insufficient generation of wind power, power is required from the upper grids to meet the demand of electric loads together with the low wind power generation in that period. When the wind power generation is greater than the electric loads, as assumed that no energy storage system is installed in the electric distribution network, the surplus wind power generation can only be curtailed and thus wasted.

In Scenario II, according to Table 5.2 and Fig 5.6, with the engagement of the GFUs, the electricity demand is covered by both the power from the upper girds (50.69%) and the power

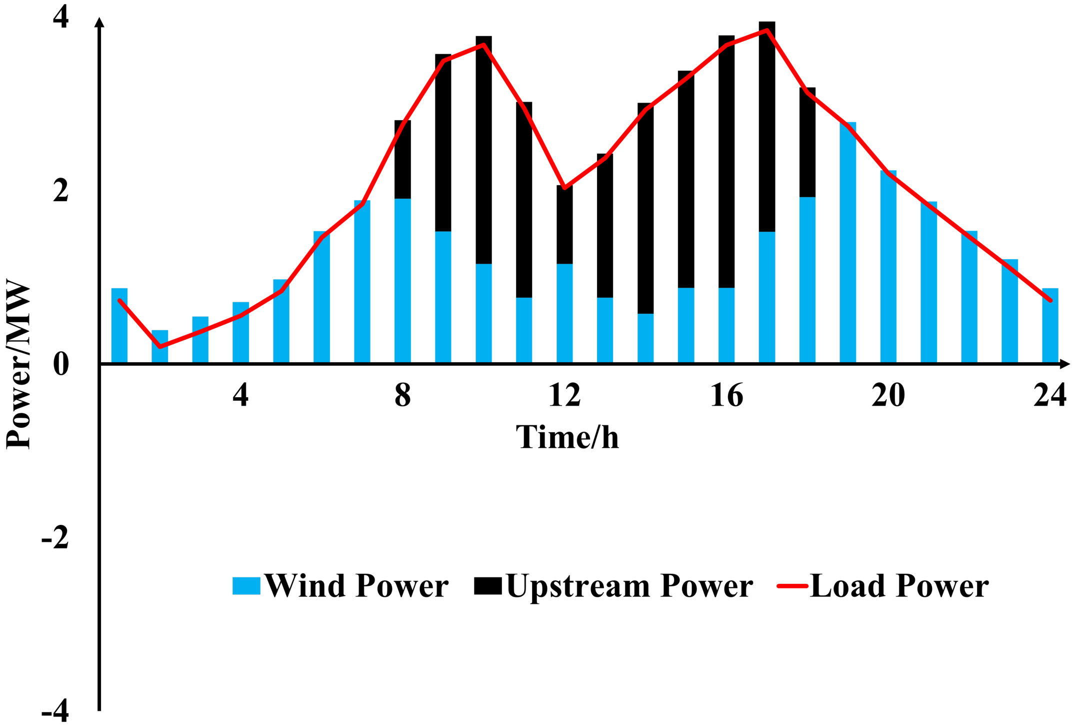

Figure 5.5: Hourly Profiles of Electricity for Scenario I

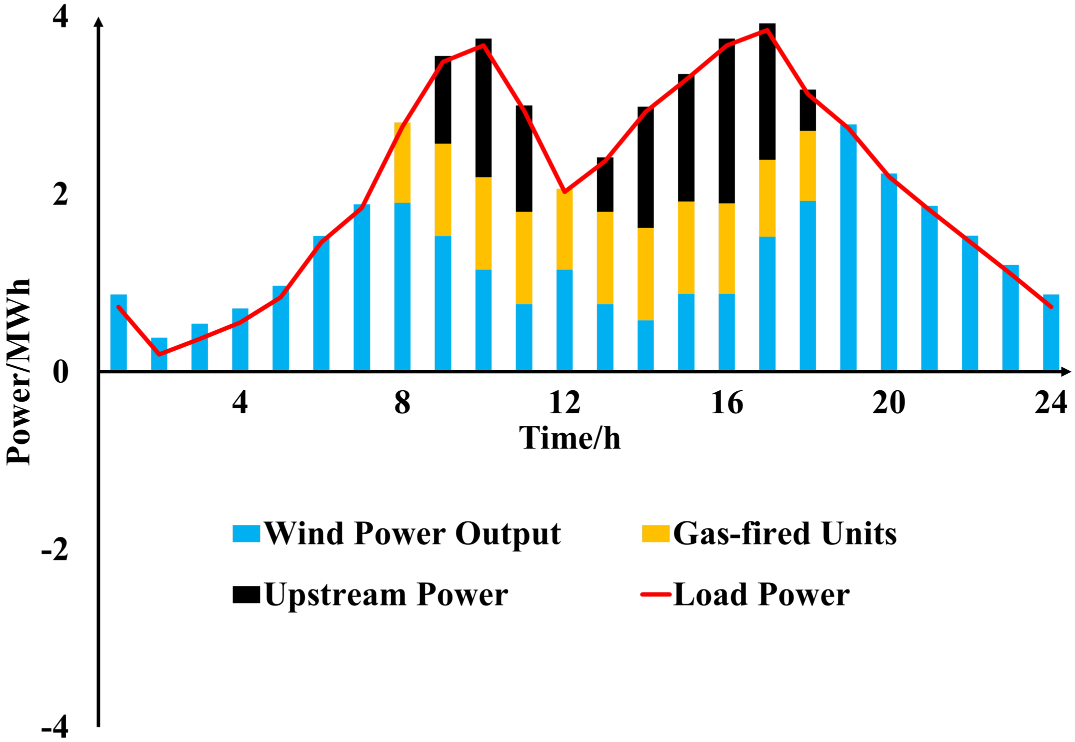

Figure 5.6: Hourly Profiles of Electricity for Scenario II

generation of GFUs (49.31%). The power from the upper girds is reduced from 21.93 MWh to 11.02 MWh. Meanwhile, the output of the gas wells increases by 201.07% from 67.47 kcf to 203.13 kcf. The increased amount of natural gas is used as the fuel of GFUs. As shown in Fig 5.6, during the hours 1-7 and hours 19-24, all the electric loads are also supplied by the wind power generation as the same in Scenario I. However, during the hours 8-18, compared with Scenario I of Fig 5.5, nearly half of the power from upper girds (black bars) is replaced by the power generation of GFUs (orange bars).

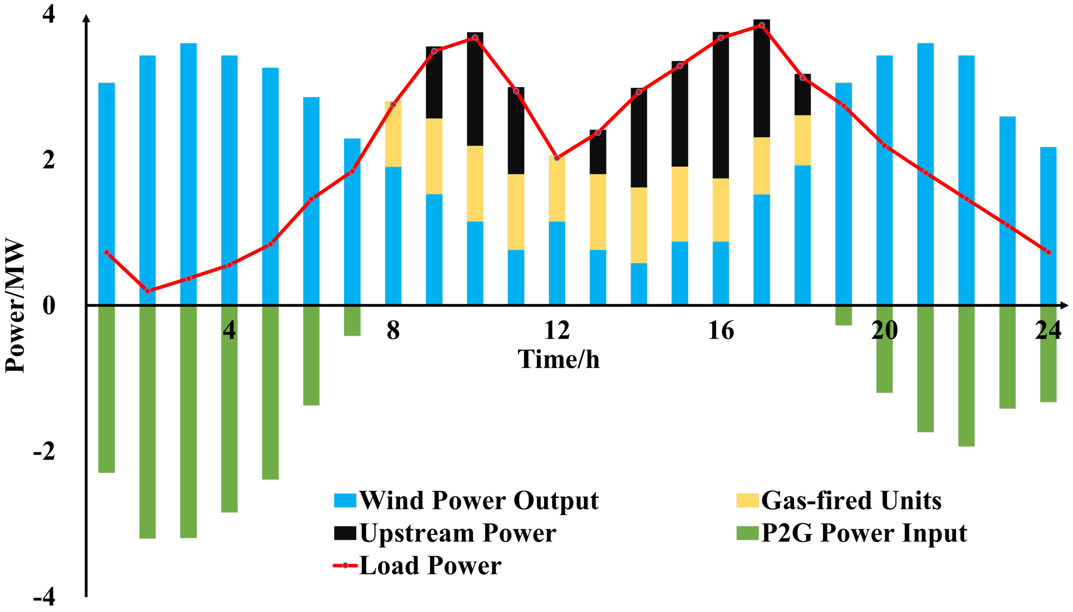

Figure 5.7: Hourly Profiles of Electricity for Scenario III

In Scenario III, the power from the upper girds and the generation of GFUs are the same as in Scenario II. However, from the comparison of Fig 5.6 and 5.7, the wind power output (blue bars) in Scenario III is largely greater than those in Scenario II, which is also shown by the data of the curtailed wind power in Table II. In Fig 5.7, during the hours 1-7 and hours 19-24 when the wind power generation is excessive, the P2G device is deployed to operate; while during the hours 8-18 when the power generation of the wind power is insufficient to meet the demand of electricity, the P2G device stops working.

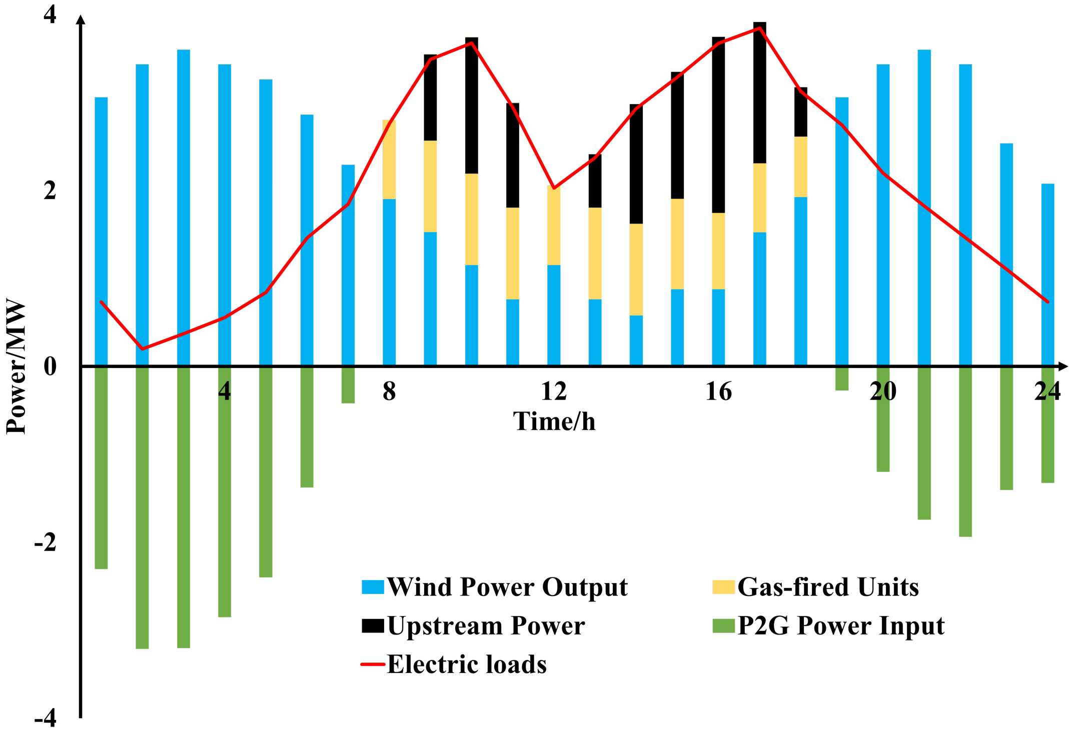

Figure 5.8: Hourly Profiles of Electricity for Scenario IV

Scenario IV exhibits an hourly electricity profile akin to that of Scenario V, as indicated in Fig 5.7 and 5.8. From Table 5.2, Scenario IV has the most efficient performance metrics across all scenarios, with the lowest power loss pf the electric power network at 0.34 MWh and a minimum three-phase voltage unbalance factor of 3.14. The primary distinction between Scenarios III and IV, within the electric power network of MES, lies in the operation of the ASP-SOP in Scenario IV, suggesting that the operational deployment of ASP-SOP contributes to the enhancement of power quality in the electricity grid.

Integration of Wind Power Generation

Fig 5.9 illustrates a comparative analysis of hourly wind power integration across four different scenarios. In Scenarios I and II, the hourly outputs of wind power generation exhibit a

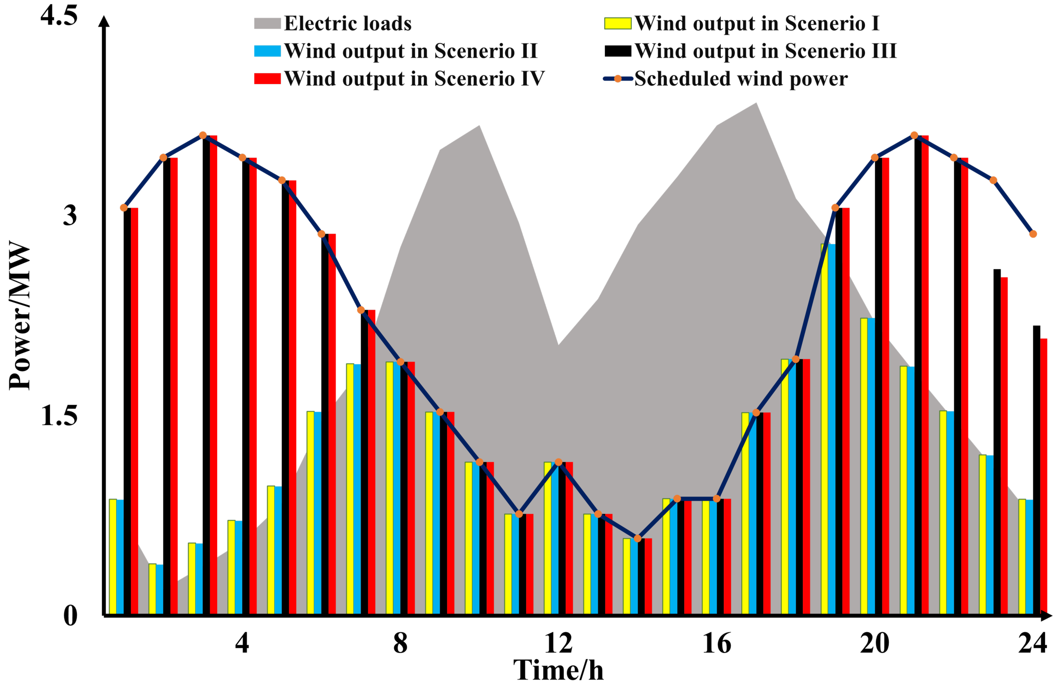

Figure 5.9: Integration of Wind Power generation

similar pattern with a notable level of wind power curtailment. In contrast, Scenarios III and IV demonstrate a close alignment between the wind power generation output and the available wind power curve. This is because the P2G unit, which works as a controllable load in the electric power network, can efficiently convert excess wind power into natural gas, subsequently storing it in gas pipelines.

The data from Fig 5.9 and Table 5.2 reveal that approximately 1.35 MWh of available wind power is curtailed during hours 23 and 24 in Scenario III, compared to 1.51 MWh at the same time in Scenario IV. Constrained by equation (5.20), the line pack of the natural gas pipelines at the end of the optimisation period is equal to that at the beginning, resulting that despite the P2G device significantly reducing the amount of curtailed wind power, there may be still a certain amount of wind power generation that goes wasted.

The P2G unis is operated in both Scenarios III and IV. Furthermore, the additional operation of ASP-SOPs in Scenario IV does not lead to a further reduction in wind power curtailment compared with in Scenario III. Therefore, it is primarily the P2G system that facilitates the utilisation of surplus wind power, which would otherwise be curtailed due to the capacity constraints of the power system. This mechanism significantly enhances the overall integration of wind power generation into the MES.

Three-Phase Voltage Imbalance

The hourly condition three-phase voltage condition for each scenario is presented in Fig 5.10 and the numerical value of VUF is shown in Table 5.2.

As the three-phase unbalanced power distribution system is modelled in the case studies, the unbalanced condition of the three-phase voltage at each node is also evaluated here by using the voltage unbalanced factor (VUF). The calculation of VUF is shown as follows.

$$VUF = \sum_{t=0}^{T}\sum_{i=1}^{N}\left(\frac{|V_{i,t,-}|^2}{|V_{i,t,+}|^2}\right) \tag{5.33}$$

$$V_{i,t,+} = \frac{1}{3}\left(V_{i,t}^{a} + \alpha^2 V_{i,t}^{b} + \alpha V_{i,t}^{c}\right) \tag{5.34}$$

$$V_{i,t,-} = \frac{1}{3}\left(V_{i,t}^{a} + \alpha V_{i,t}^{b} + \alpha^2 V_{i,t}^{c}\right) \tag{5.35}$$

where $V_{i,t,+}$ is the positive sequence voltage at node i at time t; $V_{i,t,-}$ is the negative sequence voltage at node i at time t; $\alpha = 1\angle 120$.

In Scenarios I, II, and III, during peak electricity load times (from 8 to 18 hours), the VUF, illustrated in Fig 5.10, indicates a deterioration in the condition of three-phase voltage balance. This trend reverses during non-peak times. Scenario II exhibits a notable mitigation of the three-phase voltage imbalance during peak hours in comparison to Scenario I. This improvement is primarily due to the operation of GFUs, which introduce a balanced three-phase power supply into the electric grid.

In Scenario III, the incorporation of the P2G unit causes a further improvement in the condition of voltage balance compared to Scenario II. This improvement is particularly evident during hours 1 to 8 and 19 to 23. The reason for this improvement is twofold: the P2G unit evenly draws electric energy from all three phases of the power system and operates during these hours to utilise excess wind power generation.

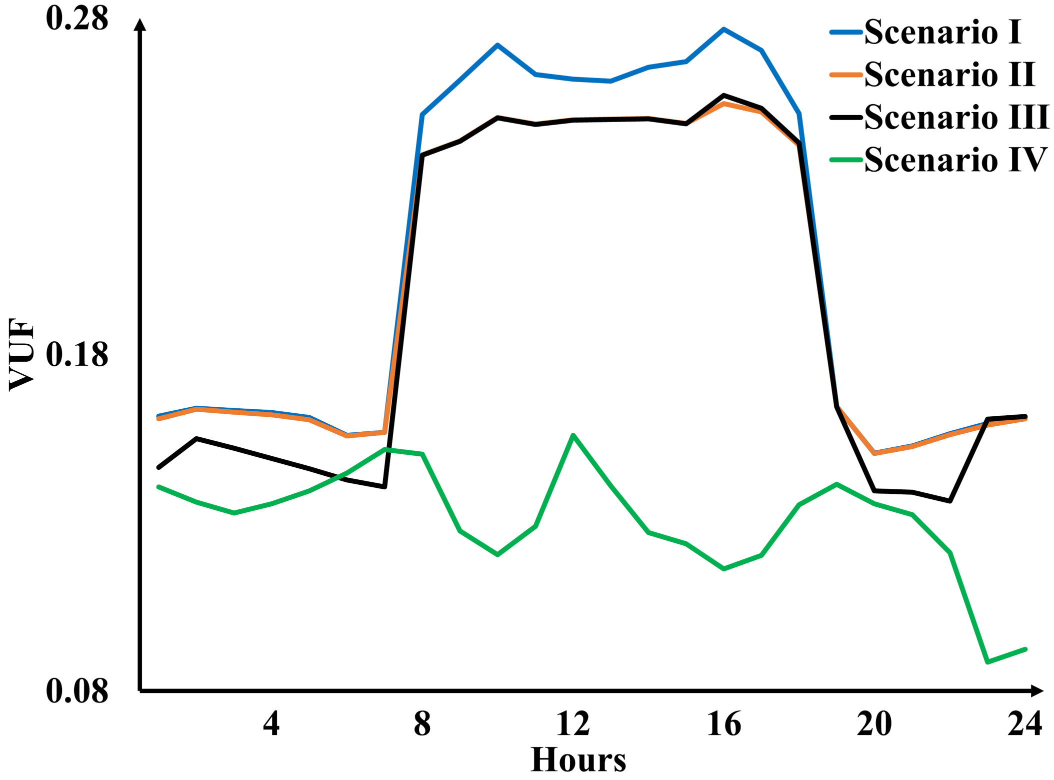

Figure 5.10: Three-Phase Voltage Imbalance Condition in All Scenarios

The implementation and operation of the ASP-SOP, in Scenario IV, results in a substantial reduction in the VUF by 32.76% (decreasing from 4.67 to 3.14) compared to Scenario III. This is because the ASP-SOP facilitates a three-phase power exchange, allowing the power from heavily loaded feeders to be shifted to lighter-loaded feeders, thus reducing the condition of three-phase voltage imbalance.

Overall, the creation of an electricity-gas MES can contribute to reducing the three-phase voltage imbalance in the electric grid. Additionally, the ASP-SOP plays a pivotal role in further alleviating this imbalance by optimising the distribution of power across the three phases.

5.5.4 Technical Benefit Comparison of Three Scenarios from Various Natural Gas Profiles

Fig 5.11 shows the hourly profiles of natural gas in Scenarios II and III. In Scenario II, from hours 1 to 9, the two gas wells inject the natural gas into the pipelines; during the daytime of the peak load period, the GFUs generate power. Also, some natural gas is injected into pipelines near the end of the day (hours 22-24). This late-day injection is to fulfil the operational constraint: ensuring that the stored mass of natural gas initially stored in the pipelines at the beginning of the optimisation period is equal to the amount at the end.

According to Table 5.2 and Fig 5.11, the operation of the P2G device, as indicated by the green line, causes a significant reduction in the output of the gas wells in Scenario III. Specifically, the gas wells' output in Scenario III is 150.52 kcf, which is 25.90% lower than the 203.13 kcf in Scenario II.

Also, the gas wells in Scenario III do not have gas generation near the end of the day (hours 22-24) as shown in Scenario II, attributed to that during the evening time of hours 19-24, the P2G converts the surplus wind power generation to natural gas, reducing the need for additional gas generation from the gas wells during these hours. Furthermore, the gas output profile of

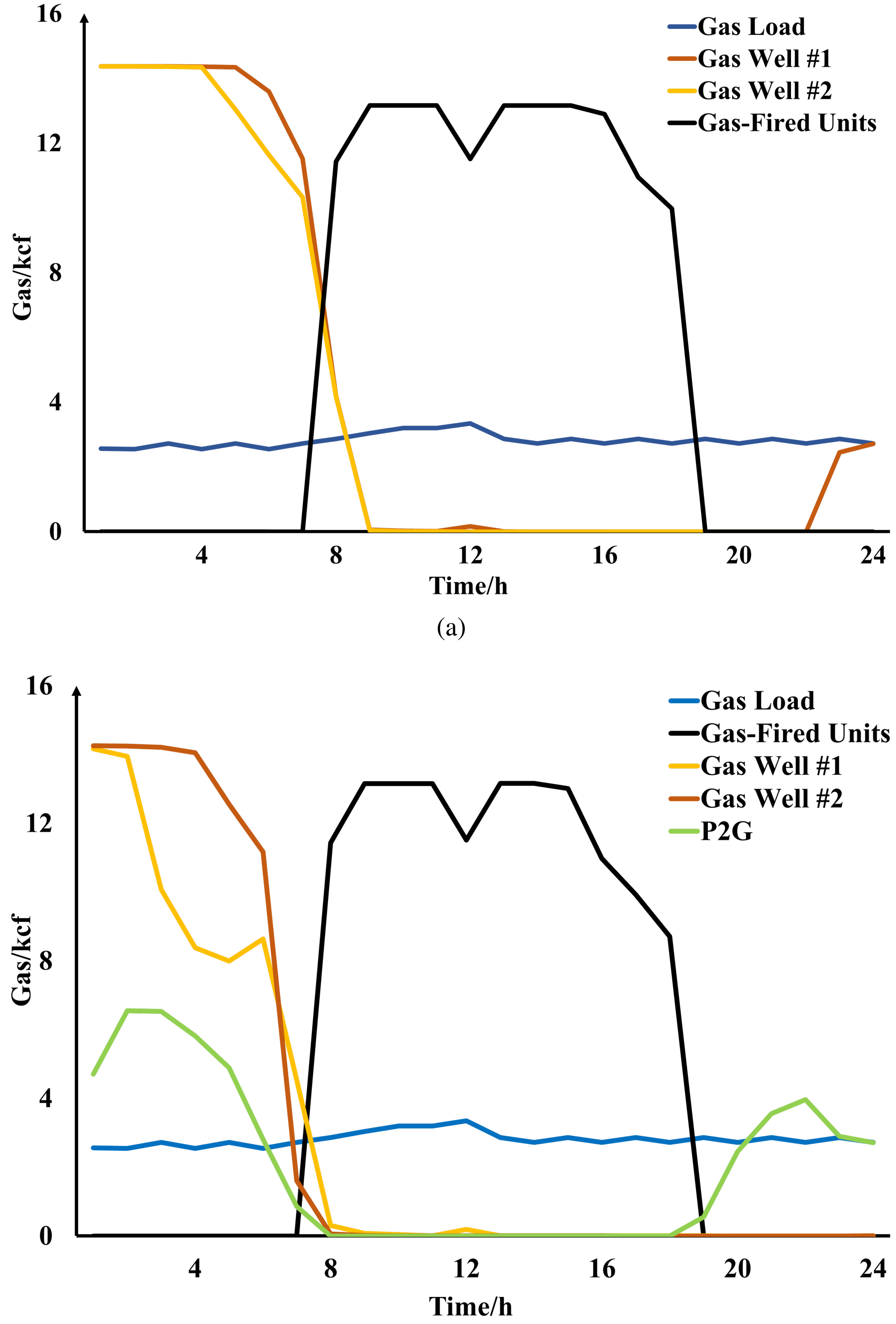

(a)

(b)

Figure 5.11: Hourly Profiles of Natural Gas: (a) Scenario II; (b) Scenario III

the P2G device in Scenario III, as depicted by the green line in Fig 5.11 (b), directly correlates with the electricity input profile of the P2G device which is illustrated in the green bars of Fig 5.7.

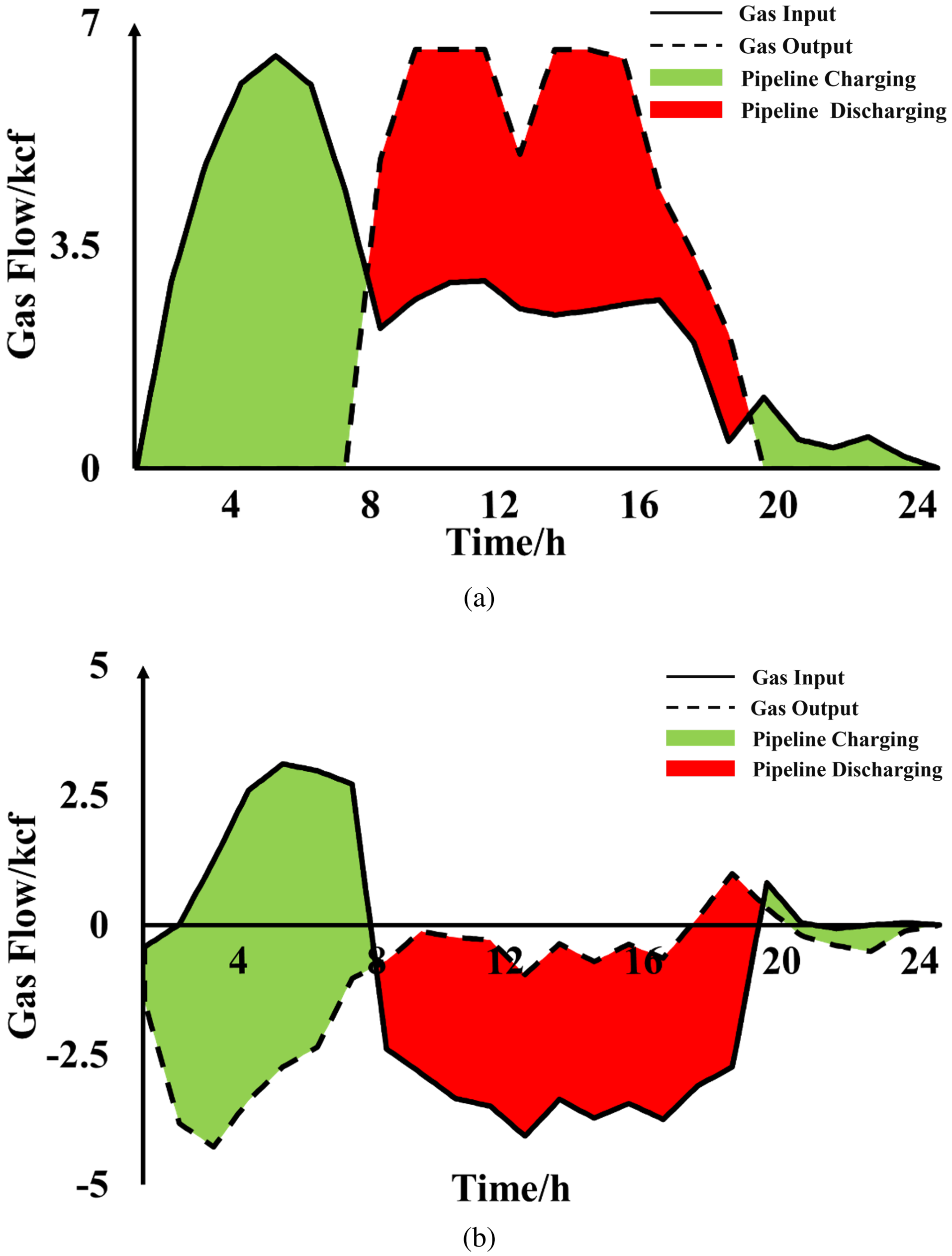

Figure 5.12: Dynamics of Natural Gas Pipeline: (a) between Nodes 5 and 6; (b) between Nodes 3 and 5

The dynamic profiles of the natural gas pipelines are shown in Fig 5.12. According to Fig 5.3, in both Fig 5.12 (a) and (b), the charging periods of the pipelines align with times when the wind power generation exceeds electric loads. During these intervals, the P2G unit converts the excess wind power into natural gas, which is then stored in the pipeline. Conversely, when the wind power generation falls short of the electric loads, the P2G device ceases operation, and GFUs are activated to generate electricity using natural gas as fuel, resulting in the discharge of natural gas from the pipelines.

As illustrated in Fig 5.12 (a), both the curve of pipeline charging (solid line) and discharging (dash line) always remain non-negative, meaning that all the natural gas in the pipeline, between nodes 5 and 6, is only charged from node 5 and discharged through node 6. In contrast, in the pipeline, between nodes 3 and 5, in Fig 5.12 (b), both two nodes can conduct the charging and discharging of the natural gas.

By converting surplus renewable energy sources into natural gas and storing it in the pipelines, the P2G unit can charge the natural gas pipelines due to the dynamic line pack of the pipeline. Meanwhile, GFUs can generate electricity for the electric power system using the natural gas stored in pipelines. As a result, the natural gas network can serve as an energy storage system for electric power.

5.6 Conclusions

In this chapter, an operational optimisation method for the electricity and gas MESs, having bi-directional energy flows through P2G facilities and GUFs, is designed and developed to minimise the operational cost, wind power curtailment, the imbalance condition of voltage and the overall carbon emission. The symmetrical SDP method is applied to convert the original non-convex nonlinear model into an SDP model via convex relaxation.

The results of the case studies indicate that the proposed strategy is effective in jointly minimising the operational cost, limiting the curtailment of wind power, mitigating the voltage imbalance and reducing the emission of carbon. Also, it is proven in this paper that the P2G technology can release system flexibility and benefit the economy by economically managing the carbon footprint of the entire system, via converting excess 'green' electricity into natural gas injected into pipelines.

One limitation of the proposed method is that its effectiveness relies on the initial input information, meaning that all data, including the power grid, gas network, loads and REG, should be given at the first step of optimisation. Consequently, this optimisation method may struggle in dealing with operational uncertainties, e.g. fluctuation of REG and loads and unexpected gird faults. In the future, additional methodologies need to be developed to address the stochastic challenges arising from the fluctuating outputs of REGs and variable load demands.

Chapter 6

Graph-Based Two-Stage Stochastic Parallel Nonlinear Optimisation for Multi-Energy Systems

6.1 Introduction

In this chapter, the graph-structured modelling is manipulated to maintain the natural characteristics of nonlinear functions or constraints in the electricity & natural gas MES. Meanwhile, to handle stochastic problems in the MES, a two-stage optimal operation strategy is proposed. Overall, the major tasks achieved in this area can be summarised as follows.

- 1. New modelling methods for MES: The graph-structured modelling is developed to address nonlinear optimisation problems in MES. This approach enables the direct modelling and solving of nonlinear constraints associated with gas pipelines and electric power flow, without the need for linearisation or convex relaxation.
- 2. New optimal strategy: To tackle the stochastic challenges posed by REGs in MES,

a two-stage stochastic operational optimisation strategy is proposed. In the first stage, the individual controllable equipment is constrained to fulfil the same power output at each time point in each scenario, while in the second stage, variables are the states of the power lines and natural gas pipelines.

- 3. The case studies, conducted in the MES of a modified IEEE-123 power grid and a 20-node gas network over 20 distinct scenarios, prove that the proposed MES optimisation strategy can reduce operational costs and curtailed wind power generation. Also, graph-based optimisation offers benefits, including the preservation of the nonlinear model without relaxation, the capability of visualisation and the reduction of solving time.

6.2 Graph-Structured Modelling & Solution of Optimisation Problems

In graph-structured nonlinear modelling, as shown in Fig 6.1, a general modelling abstraction is named Opti-Graph which is an abstract object provided by an undirect hypergraph and consists of multiple Opti-Nodes and Opti-Edges. Each Opti-Node can encapsulate a unique optimisation model and usually includes components of local variables, internal constraints, objective functions, and relevant data. In addition, the Opti-Edge, signifying the interrelations between two or more Opti-Nodes, contains the linking constraints to connect the variables between Opti-Nodes.

Two software packages, Plasmo.jl and MadNLP.jl, are utilised to apply the graph-based modelling and solution.

- Plasmo.jl is employed to construct and model optimisation problems in a graph-based framework.
- The graph-based model generated by Plasmo.jl is transferred to MadNLP.jl, which is a nonlinear programming solver applied in the Julia language.

MadNLP.jl is deployed to interact with the Opti-Graph model established by Plasmo.jl. This interfacing can yield several advantages:

- Plasmo.jl facilitates the creation of a graph-based model which contains and stores the structural information of the optimisation problem. This structural information can subsequently be efficiently leveraged by MadNLP.jl, enabling the application of specialised algorithms for solutions.
- The modular configuration of the Opti-Graph model allows the parallel evaluations of functions and derivatives. When integrated with Plasmo.jl, MadNLP.jl can at recognise and utilise the partitions as designed by Plasmo.jl.

6.2.1 Graph-Structured Modelling in Plasmo.jl

A model of a graph-structured nonlinear Optimisation problem can be described in (6.1)-(6.3). The Opti-Graph $G(N, \varepsilon)$ consists of a set of Opti-Nodes N and a set of Opti-Edges ε. N(n) represents the neighbourhood of any Opti-Node n, while $N(e)$ is the set of Opti-Nodes supporting the Opti-Edge e.

$$\min_{\{\mathbf{x}_n\}_{n\in N}} \sum_{n\in N} f_n(\mathbf{x}_n) \tag{6.1}$$

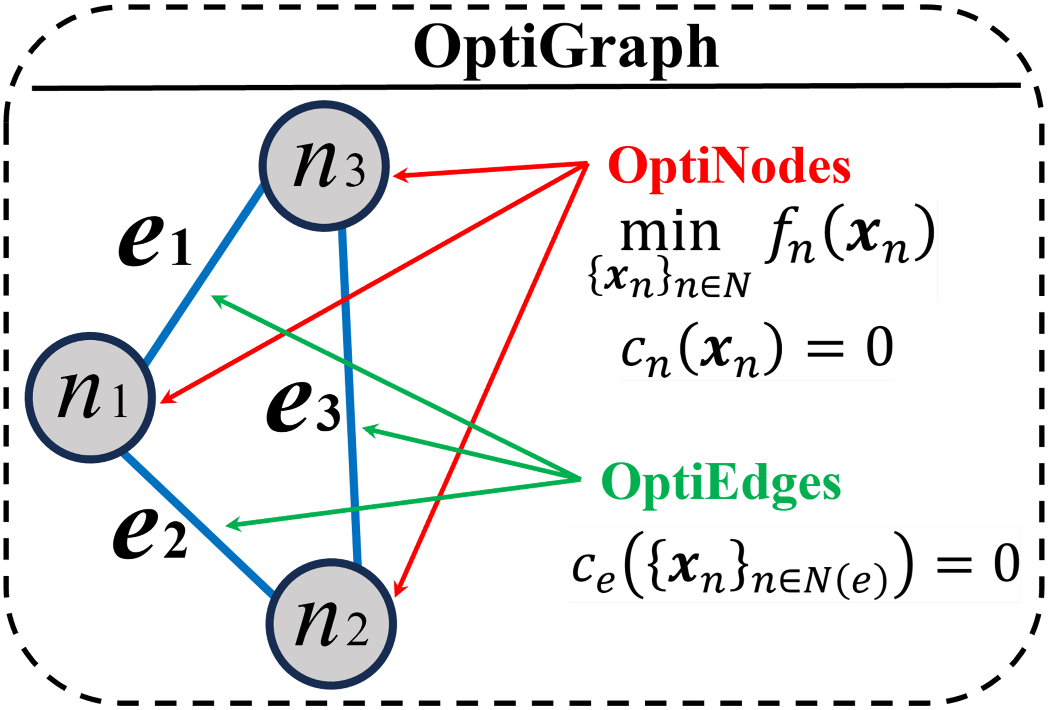

Figure 6.1: Illustration of A Graph-Structured Model

$$c_n(\mathbf{x}_n) = 0,\ n \in N \tag{6.2}$$

$$c_e(\{\mathbf{x}_n\}_{n\in N(e)}) = 0,\ e \in \varepsilon \tag{6.3}$$

where, $\mathbf{x}_n$ refers to the decision variables on the Opti-Node n and all objective functions over Opti-Nodes N is in (6.1). The constraints within an Opti-Node n are shown in (6.2), while equation (6.3) defines the linking constraints of the Opti-Edge e which may connect variables in multiple Opti-Nodes.

6.2.2 Decomposition Strategy in MadNLP.jl

As shown in Fig 6.2, the graph-structured modelling can deploy the decomposition strategy, where the Opti-Nodes can be recognised as subproblems whose solutions are used to discover

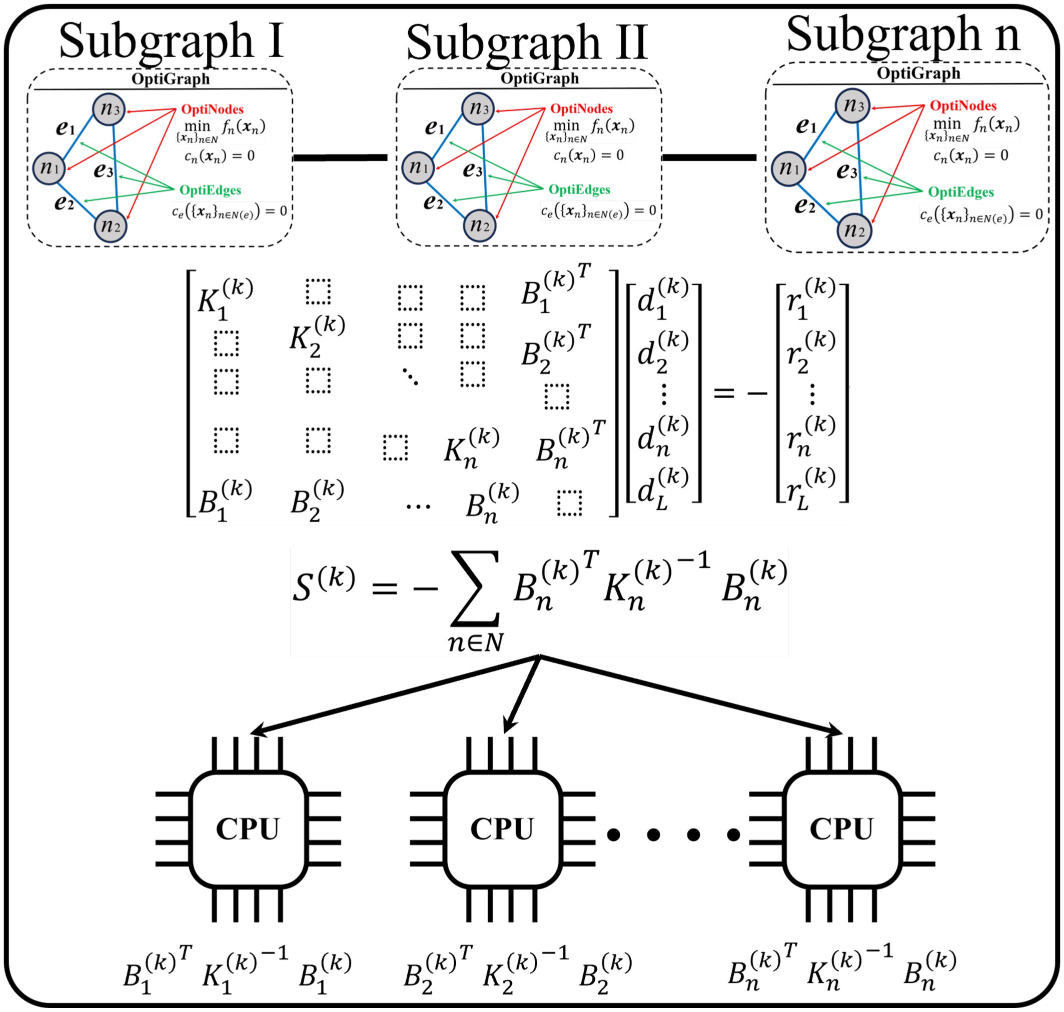

Figure 6.2: Decomposition Strategy to Parallelize Function and Derivative Evaluations

the optimal solution of the whole Opti-Graph. The Karush-Kuhn-Tucker (KKT) conditions of the graph-structured nonlinear modelling are expressed as follows.

$$\nabla_{\mathbf{x}_n} f_n(\mathbf{x}_n) + \mu \mathbf{X}_n^{-1}\mathbf{1} + \nabla_{\mathbf{x}_n} c_n(\mathbf{x}_n)\lambda_n + \sum_{e\in\varepsilon(n)} \nabla_{\mathbf{x}_n} c_e(\{\mathbf{x}_n\}_{n\in N(e)})\lambda_e = 0 \tag{6.4}$$

$$c_n(\mathbf{x}_n) = 0,\ n \in N \tag{6.5}$$

$$c_e(\{\mathbf{x}_n\}_{n\in N(e)}) = 0,\ e \in \varepsilon \tag{6.6}$$

where $\mathbf{X}_n = \mathrm{diag}(\mathbf{x}_n)$ and $\mathbf{1} := [1, 1, \cdots, 1]$; $\varepsilon(n)$ refers to the set of Opti-Edges supported by Opti-Node n; μ is the parameter of penalty; λ_n and λ_e are the variables related to the Opti-Node constraints and the linking constraints separately.

For further deduction, $\mathbf{z}_n$, $\mathbf{Z}_n$ and $\sum_n^{(k)}$ are defined as follows.

$$\mathbf{z}_n := \mu \mathbf{X}_n^{-1} \mathbf{1} \tag{6.7}$$

$$\mathbf{Z}_n := \mathrm{diag}(\mathbf{z}_n) \tag{6.8}$$

$$\sum_n^{(k)} := X_n^{(k)-1} Z_n^{(k)} \tag{6.9}$$

$$\begin{bmatrix} K_1^{(k)} & & & & {B_1^{(k)}}^T \\ & K_2^{(k)} & & & {B_2^{(k)}}^T \\ & & \ddots & & \\ & & & K_n^{(k)} & {B_n^{(k)}}^T \\ B_1^{(k)} & B_2^{(k)} & \cdots & B_n^{(k)} & \end{bmatrix} \begin{bmatrix} d_1^{(k)} \\ d_2^{(k)} \\ \vdots \\ d_n^{(k)} \\ d_L^{(k)} \end{bmatrix} = - \begin{bmatrix} r_1^{(k)} \\ r_2^{(k)} \\ \vdots \\ r_n^{(k)} \\ r_L^{(k)} \end{bmatrix} \tag{6.10}$$

where $d_n^{(k)} := (\Delta d_{n,k}, \Delta\lambda_n)$ are the primal-dual steps for the variables and constraints of Opti-Node n; $\Delta d_{n,k}$ are the primal steps and $\Delta\lambda_n$ are the dual steps corresponding to λ_e; the definitions of $K_n^{(k)}$, $B_n^{(k)}$, $r_n^{(k)}$, and $r_L^{(k)}$ are given as follows.

$$K_n^{(k)} := \begin{bmatrix} W_n^{(k)} + \sum_n^{(k)} & {J_n^{(k)}}^T \\ J_n^{(k)} & 0 \end{bmatrix} \tag{6.11}$$

$$B_n^{(k)} := \begin{bmatrix} Q_n^{(k)} & 0 \end{bmatrix} \tag{6.12}$$

$$Q_n^{(k)} := \nabla_{x_n} \left\{ c_e \left(x_n^{(k)} \right) \right\}_{n \in N(e)} \tag{6.13}$$

$$r_n^{(k)} := \begin{bmatrix} \nabla_{x_n} f_n(x_n) \\ c_n(x_n) \end{bmatrix} \tag{6.14}$$

$$r_L^{(k)} := \left\{ c_e\left(x_n^{(k)}\right) \right\}_{n \in N(e)} \tag{6.15}$$

where, $J_n^{(k)} := \nabla_{x_n} c_n(x_n^{(k)})$ is the Jacobian form of constraints of Opti-Node n; $W_n^{(k)}$ is the Hessian of the Langrangian of equation (6.1); $Q_n^{(k)}$ is the Jacobian of the linking constraints.

The Schur decomposition approach can be triggered by the block-bordered structure in (6.10). Meanwhile, the size of the matrices $K_n^{(k)}$ and $B_n^{(k)}$ can be varied according to the construction of the model and the number of the linking constraints. Given the block-bordered structure, the decomposition method is carried out by constructing the Schur complement:

$$S^{(k)} = -\sum_{n \in N} {B_n^{(k)}}^T {K_n^{(k)}}^{-1} B_n^{(k)} \tag{6.16}$$

$$S^{(k)} d_L^{(k)} = \sum_{n \in N} {B_n^{(k)}}^T {K_n^{(k)}}^{-1} r_n^{(k)} - r_L^{(k)} \tag{6.17}$$

$$K_n^{(k)} d_n^{(k)} = B_n^{(k)} d_L^{(k)} - r_n^{(k)} \tag{6.18}$$

The computation of ${B_n^{(k)}}^T$, ${K_n^{(k)}}^{-1}$ and $B_n^{(k)}$ is parallelised as each block can be run independently. In equation (6.16), ${B_n^{(k)}}^T$, ${K_n^{(k)}}^{-1}$ and $B_n^{(k)}$ are integrated into matrix $S^{(k)}$. Then, the dual-step direction for the linking constraints can be obtained through (6.17). As a result, the parallel computation of the block steps can be conducted in (6.18).

6.3 Optimal Operational Coordination Problem Formulation of Electricity-Gas Multi-Energy System

Applying the above-described model, a graph-based two-stage stochastic operational optimisation strategy is proposed for a multi-scenario MES. In the first stage, all controllable equipment is required to have the same performance at each time point in each scenario, while in the second stage, the variables are the states of the electric power flows and the natural gas pipeline flows. Each scenario has a different output profile of REG.

In this section, L_c and L_p represent the set of all natural gas network compressors and pipelines respectively. $T := \{1,...,N_t\}$ is a set of time points; S refers to the set of all scenarios; $X := \{1,...,N_x\}$ describes a set of equal spatial points of pipelines.

6.3.1 Objective Functions

The objective functions, described in (6.19)-(6.21), are to simultaneously minimise the total operational costs and the curtailment of the wind power generation. In the operation of MES, the stakeholders often prioritise operational costs and the integration of REGs due to economic considerations. Also, it is important to note that reducing operational costs often correlates with decreasing carbon emissions. This is because cost reductions in MES often result from improved operational efficiency and increased use of REGs, both of which naturally lead to lower emissions. Thus, by focusing on the two objectives, the research indirectly contributes to reducing carbon footprints, despite not including carbon emissions in the objective functions.

$$\min \sum_{t\in T,\ s\in S} (\alpha F^{C} + \beta F^{W}) \tag{6.19}$$

$$F^{C} = \sum_{l\in L_c, t\in T, s\in S} [C^{grid} P^{grid}_{t,s} + C^{gas} f^{gas}_{t,s}] \tag{6.20}$$

$$F^{W} = \sum_{t\in T,\ s\in S} \left(P^{Avail}_{t,s} - P^{Wind}_{t,s} \right) \tag{6.21}$$

where α and β are the weight of the two objectives; C^{grid} and C^{gas} are the costs of electricity and natural gas respectively; $P^{grid}_{t,s}$ is the electricity injection from the upstream power grid at time t in scenario s; $f^{gas}_{t,s}$ is the gas supply at time t in scenario s; $P^{Avail}_{t,s}$ is the available wind power generation at time t in scenario s; $P^{Wind}_{t,s}$ is the real-time wind power output at time t in scenario s.

6.3.2 Natural Gas Network Constraints

In this section, the complete gas network constraints are listed with descriptions including those for the compressors and pipelines.

Compressor Constraints

All the constraints of the compressor are for $l \in L_c$, $t \in T$ and $s \in S$. The power consumption of the compressor is computed in (6.22) and the relation, between the suction pressure and the discharge pressure, is expressed in (6.23).

$$P^{comp}_{l,t,s} = c_p \cdot T^{gas} \cdot f^{comp}_{l,t,s} \left[\left(\frac{p^{dis}_{l,t,s}}{p^{suc}_{l,t,s}} \right)^{\frac{\gamma-1}{\gamma}} - 1 \right] \tag{6.22}$$

$$p^{dis}_{l,t,s} = p^{suc}_{l,t,s} + \Delta p^{comp}_{l,t,s} \tag{6.23}$$

where $p^{suc}_{l,t,s}$, $p^{dis}_{l,t,s}$ and $\Delta p^{comp}_{l,t,s}$ are the pressure of suction, discharge and boost in the compressor l at time t for scenario s; $P^{comp}_{l,t,s}$ is the power consumption of the compressor l at time t for scenario s; $f^{comp}_{l,t,s}$ is the gas flow through the compressor l at time t for scenario s; c_p, T_{gas} and γ are the natural gas parameters of heating capacity, temperature and isentropic efficiency respectively.

Equation (6.24) requires that in the compressor, the input of gas flow is equal to the output.

$$f^{comp}_{l,t,s} = f^{in}_{l,t,s} = f^{out}_{l,t,s} \geq 0 \tag{6.24}$$

where $f^{in}_{l,t,s}$ and $f^{out}_{l,t,s}$ are the input and output flow of the compressor l at time t in scenario s, separately.

The limits for the pressure of suction, discharge and boost are in (6.26), (6.27) and (6.28), respectively.

$$0 \leq P^{comp}_{l,t,s} \leq P^{comp}_{Max} \tag{6.25}$$

$$p^{suc}_{Min} \leq p^{suc}_{l,t,s} \leq p^{suc}_{Max} \tag{6.26}$$

$$p^{dis}_{Min} \leq p^{dis}_{l,t,s} \leq p^{dis}_{Max} \tag{6.27}$$

$$0 \leq \Delta P^{comp}_{l,t,s} \leq \overline{\theta}_{boost} \tag{6.28}$$

where P^{suc}_{Max} and P^{suc}_{Min} are the upper and lower limits for the suction pressure of the compressor; p^{dis}_{Max} and P^{dis}_{Min} are the maximum and minimum discharge pressure of the compressor; $\overline{\theta}_{boost}$ is the maximum limit for the pressure of boost in the compressor.

Pipeline Constraints

All pipeline constraints are for $l \in L_p$, $t \in T$, $k \in X$ and $s \in S$. Equations (6.29) and (6.30) are the mass and momentum dynamics of the pipeline. The starting steady state is defined in (6.31) and (6.32). The line pack of pipelines is calculated in (6.33), while equation (6.35) requires that the line pack at the end of the time period is not less than the initial amount.

$$\frac{p^{gas}_{l,t,k,s} - p^{gas}_{l,t-1,k,s}}{\Delta t} + c_{1,l}\frac{f^{gas}_{l,t,k+1,s} - f^{gas}_{l,t,k,s}}{\Delta x_l} = 0 \tag{6.29}$$

$$\frac{f^{gas}_{l,t,k,s} - f^{gas}_{l,t-1,k,s}}{\Delta t} + c_{2,l}\frac{P^{gas}_{l,t,k+1,s} - P^{gas}_{l,t,k,s}}{\Delta x_l} + c_{3,l}\frac{f^{gas}_{l,t,k,s}\left|f^{gas}_{l,t,k,s}\right|}{P^{gas}_{l,t,k,s}} = 0 \tag{6.30}$$

$$\frac{f^{gas}_{l,t,k+1,s} - f^{gas}_{l,t,k,s}}{\Delta x_l} = 0 \tag{6.31}$$

$$c_{2,l}\frac{P^{gas}_{l,1,k+1,s} - P^{gas}_{l,1,k,s}}{\Delta x_l} + c_{3,l}\frac{f^{gas}_{l,1,k,s}\left|f^{gas}_{l,1,k,s}\right|}{P^{gas}_{l,1,k,s}} = 0 \tag{6.32}$$

$$S_{l,t,s} = \frac{1}{c_{1,l}}\sum_{k=1}^{N_x} P^{gas}_{l,t,k,s}\Delta x_l \tag{6.33}$$

$$S_{l,N_t,s} \geq S_{l,1,s} \tag{6.34}$$

$$f^{gas}_{l,t,1,s} = f^{in}_{l,t,s} \tag{6.35}$$

$$f^{gas}_{l,t,N_x,s} = f^{out}_{l,t,s} \tag{6.36}$$

$$P^{gas}_{l,t,1,s} = P^{in}_{l,t,s} \tag{6.37}$$

$$P^{gas}_{l,t,N_x,s} = P^{out}_{l,t,s} \tag{6.38}$$

where $p^{gas}_{l,t,k,s}$ and $f^{gas}_{l,t,k,s}$ represent the pressure and flows at the spatial point k of the pipeline l in time t of scenario s, separately; $f^{gas}_{l,t,1,s}$ and $f^{in}_{l,t,s}$ are the input flow at the spatial point k of the pipeline l in time t of scenario s; $f^{gas}_{l,t,N_x,s}$ and $f^{out}_{l,t,s}$ are the output flow at the spatial point k of the pipeline l in time t of scenario s; $P^{gas}_{l,t,1,s}$ and $P^{in}_{l,t,s}$ are the pressure at the start of the pipeline l in time t of scenario s; $P^{gas}_{l,t,N_x,s}$ and $P^{out}_{l,t,s}$ are the pressure at the end of the pipeline l in time t of scenario s; Δt is the time interval and Δx_l is the spatial interval; $S_{l,t,s}$ is defined as the link pack of the pipeline l at time t in scenario s; $c_{1,l}$, $c_{2,l}$ and $c_{3,l}$ are the constants of the natural gas pipelines.

6.3.3 Electric Power System Constraints

This section details the electric power system constraints to entail the power flow details.

The power flow constraints of active and reactive power are in (6.39) and (6.40).

$$\sum_{i \to j} (P_{ij,t,s} - r_{ij} I^2_{ij,t,s}) = \sum_{j \to k} P_{jk,t,s} \tag{6.39}$$

$$\sum_{i \to j} (Q_{ij,t,s} - x_{ij} I^2_{ij,t,s}) = \sum_{j \to k} Q_{jk,t,s} \tag{6.40}$$

where $P_{ij,t,s}$ and $Q_{ij,t,s}$ are the active power and reactive power along branch ij at time t in scenario s respectively; $P_{jk,t,s}$ and $Q_{jk,t,s}$ represent the downstream power flows of node j at time t in scenario s.

The constraint of the voltage is in (6.41).

$$U_{i,t,s}^2 - U_{j,t,s}^2 - 2\left(r_{ij}P_{ij,t,s} + x_{ij}Q_{ij,t,s}\right) + \left(r_{ij}^2 + x_{ij}^2\right) I_{ij,t,s}^2 = 0 \tag{6.41}$$

$$I_{ij,t,s}^2 U_{i,t,s}^2 = P_{ij,t,s}^2 + Q_{ij,t,s}^2 \tag{6.42}$$

where r_{ij} and x_{ij} refer to the resistance and impedance of the branch ij; $I_{ij,t,s}$ is the current of branch ij at time t in scenario s; $U_{i,t,s}$ and $U_{j,t,s}$ are the voltage at node i and j at time t in scenario s.

The lower and upper limits for the node voltage and the branch current are in (6.43) and (6.44).

$$(\underline{U})^2 \leq U_{i,t}^2 \leq (\overline{U})^2 \tag{6.43}$$

$$I_{ij,t,s}^2 \leq (\overline{I_{ij}})^2 \tag{6.44}$$

where $\underline{U}$ and $\overline{U}$ are the lower and upper limits for the node voltage; $\overline{I_{ij}}$ is the maximum value for the current of branch ij.

6.3.4 Coupling Device Constraints

This section describes the constraints of the coupling device, including the P2G and the GFU.

Constraints of Power-to-Gas

The capacity constraint of the P2G unit is expressed in (6.45). Constraint (6.46) defines the relation between active power input and reactive power input of the P2G unit.

$$\sqrt{\left(P_{i,t,s}^{P2G}\right)^2 + \left(Q_{i,t,s}^{P2G}\right)^2} \leq S_i^{P2G} \tag{6.45}$$

$$Q_{i,t,s}^{P2G} = P_{i,t,s}^{P2G} \tan\left(\theta^{P2G}\right) \tag{6.46}$$

where $P_{i,t,s}^{P2G}$ and $Q_{i,t,s}^{P2G}$ are the active power and the reactive power of P2G in node i at time t of scenario s, respectively; S_i^{P2G} is the power capacity of P2G in node i; θ^{P2G} is the power factor of P2G.

As the P2G unit takes the electric energy from the three-phase power system, constraint (6.47) imposes that the power inputs from the three phases have the same value. The efficiency of energy conversion is in (6.48).

$$P_{a,i,t,s}^{P2G} = P_{b,i,t,s}^{P2G} = P_{c,i,t,s}^{P2G} = \frac{P_{i,t,s}^{P2G}}{3} \tag{6.47}$$

$$G_{n,t,s}^{P2G} = \eta^{P2G} \emptyset^{P2G} P_{i,t,s}^{P2G} \tag{6.48}$$

where $P_{a,i,\, t,s}^{P2G}$, $P_{b,i,\, t,s}^{P2G}$ and $P_{c,i,\, t,s}^{P2G}$ are the active power of P2G unit in phase a, b, and c of node i at time t of scenario s, respectively; $G_{n,t,s}^{P2G}$ is the natural gas output of P2G at node n at the time t of scenario s; $\emptyset^{P2G}$ is the energy conversion factor of natural gas and electricity; η^{P2G} is the energy efficiency of P2G.

Constraints of Gas-Fired Units

The capacity constraint of GFU is in (6.49). The power factor of GFU is in (6.50) to define the relation between the active power and the reactive power.

$$\sqrt{\left(P_{i,t,s}^{GFU}\right)^2+\left(Q_{i,t,s}^{GFU}\right)^2} \leq S_i^{GFU} \tag{6.49}$$

$$Q_{i,t,s}^{GFU}=P_{i,t,s}^{GFU}\tan\left(\theta^{GFU}\right) \tag{6.50}$$

where $P_{i,t,s}^{GFU}$ and $Q_{i,t,s}^{GFU}$ are the active power and reactive power of GFU at node i at time t of scenario s, respectively; S_i^{GFU} is the capacity of the GFU at node i; θ^{GFU} is the power factor of the GFU.

As the GFUs inject power into the three-phase power system, constraint (6.51) guarantees that the outputs of three phases share the same values of both active power and reactive power.

$$P_{a,i,t,s}^{GFU}=P_{b,i,t,s}^{GFU}=P_{c,i,t,s}^{GFU} \tag{6.51}$$

where $P_{a,i,t,s}^{GFU}$, $P_{b,i,t,s}^{GFU}$ and $P_{c,i,t,s}^{GFU}$ are the active power output of GFU unit in phase a, b, and c of node i at time t of scenario s, respectively.

6.3.5 Variables of Two-Stage Optimal Operation

In the first stage, the controllable units are compressors, P2G, GFU, and wind power generation. Therefore, the first-stage variables are given as follows.

$$\dot{P}_{l,t}^{comp} = P_{l,t,s}^{comp}, \;\; l \in \mathscr{L}_c, t \in \mathscr{T}, s \in \mathscr{S} \tag{6.52}$$

$$\dot{P}_{i,t}^{P2G} = P_{i,t,s}^{P2G}, \;\; t \in \mathscr{T}, s \in \mathscr{S} \tag{6.53}$$

$$\dot{P}_{i,t}^{GFU} = P_{i,t,s}^{GFU}, \;\; t \in \mathscr{T}, s \in \mathscr{S} \tag{6.54}$$

$$\dot{P}_{i,t}^{Wind} = P_{i,t,s}^{Wind}, \;\; t \in \mathscr{T}, s \in \mathscr{S} \tag{6.55}$$

where $\dot{P}_{l,t}^{comp}$, $\dot{P}_{i,t}^{P2G}$, $\dot{P}_{i,t}^{GFU}$, and $\dot{P}_{i,t}^{Wind}$ are the first-stage variables for the compressors, P2G unit, GFU units, and the wind power generation, respectively. $P_{i,t,s}^{Wind}$ is the real-time wind power output at node i in the electric power grid.

These first-stage variables are applied to guarantee uniformity in the power output of each controllable unit across all scenarios by mandating that specific units maintain consistent power policy at every time of each scenario. All other variables, as detailed in Section 6.3, are categorised as the second-stage variables.

6.4 Case Studies

The optimisation program for case studies in this section was coded in Julia and solved by MA57 in Visual Studio of Virtual Machine.

6.4.1 System Overview

In Fig. 6.3, an electricity-gas multi-energy system (EG-MES), consisting of a modified IEEE 123-node test feeder system and a 20-node natural gas network, is formulated in the case study to demonstrate the capability of the proposed two-stage stochastic optimisation strategy, which aims to minimise the overall operational cost and maximise the accommodation of the installed REG.

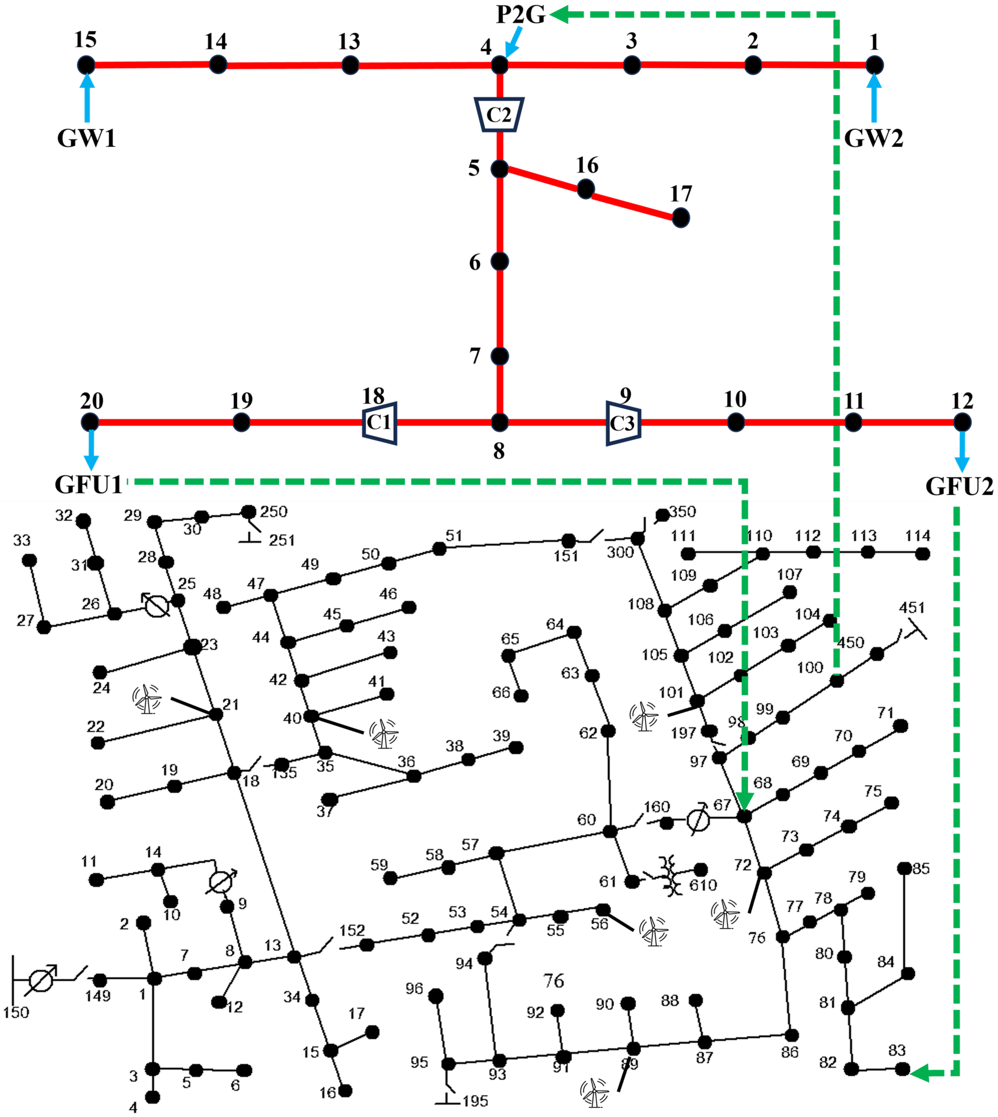

Figure 6.3: Illustration of the Case Study System - the Electricity & Natural Gas Multi-Energy System

In Fig. 6.3, the solid blue line represents the transmission of natural gas, indicating the direction of the gas flow. The green dashed line describes the power transmission, referring to the direction of the power flow.

In the electric power network, the rated voltage is 4.16 kV with the voltage limits set between 0.95 p.u. and 1.05 p.u. The active and reactive power of the electric loads in the network are 3,490 kW and 1,920 kVar, respectively [90]. An essential assumption is that all substation power (node 150) from the superior power grid is generated by coal-fired power plants.

To evaluate the potential of the P2G unit in improving the integration of REG, ten three-phase wind power generation units and two single-phase PV units have been installed within the electric power system. Each wind power unit has a capacity of 750 kW, while each unit has a capacity of 250 kW.

In the natural gas network, the GFUs are located at electric nodes 67, 83 and take natural gas as fuel from gas nodes 20, 12, respectively. The P2G unit gets electricity from electric node 100 and sends the produced natural gas to the gas network through gas node 4. Two gas wells (GWs) are located at gas nodes 1 and 15. Also, the natural gas network is equipped with three compressors: C1, C2, and C3. The parameters of the natural gas network are from [144].

The profiles of electric power loads and natural gas loads are shown in Fig 6.4. The electric power loads are generated based on the data from [90] and the gas loads' curves are modified from [144].

To demonstrate the effectiveness of the proposed stochastic optimisation model, as depicted in Fig 6.5, for both the unit of wind power and the PV, the daily stochastic profiles are applied in all the cases.

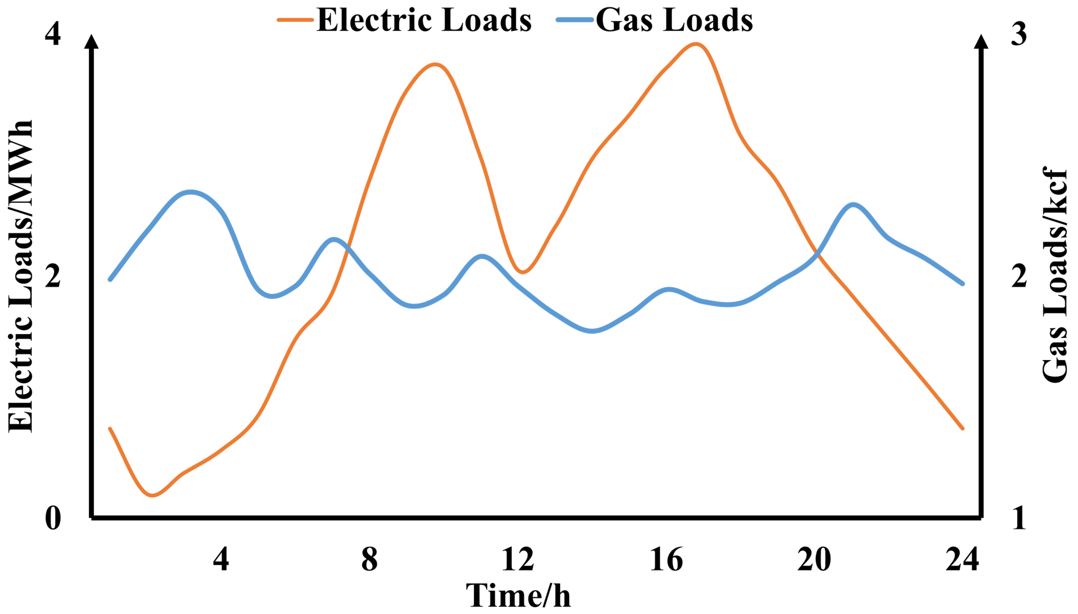

Figure 6.4: Profiles of Electric & Natural Gas Loads

Three distinct cases are designed to evaluate the advantages of the proposed method. In each of these cases, REGs are operated under 20 different scenarios.

- Case I: Independent operation of two energy vectors;
- Case II: the MES w/ GFUs, w/o P2G unit;
- Case III: the MES w/ GFUs and P2G unit

In the proposed two-stage stochastic optimisation approach, the configuration of the controllable units is determined in the first stage, while the varying variables are addressed in the second stage, as detailed in Table 6.1. In this model, the controllable units adhere to a consistent output power policy across all scenarios. However, the variables in the second stage are adjusted in response to the diverse energy demand profiles characteristic of each scenario.

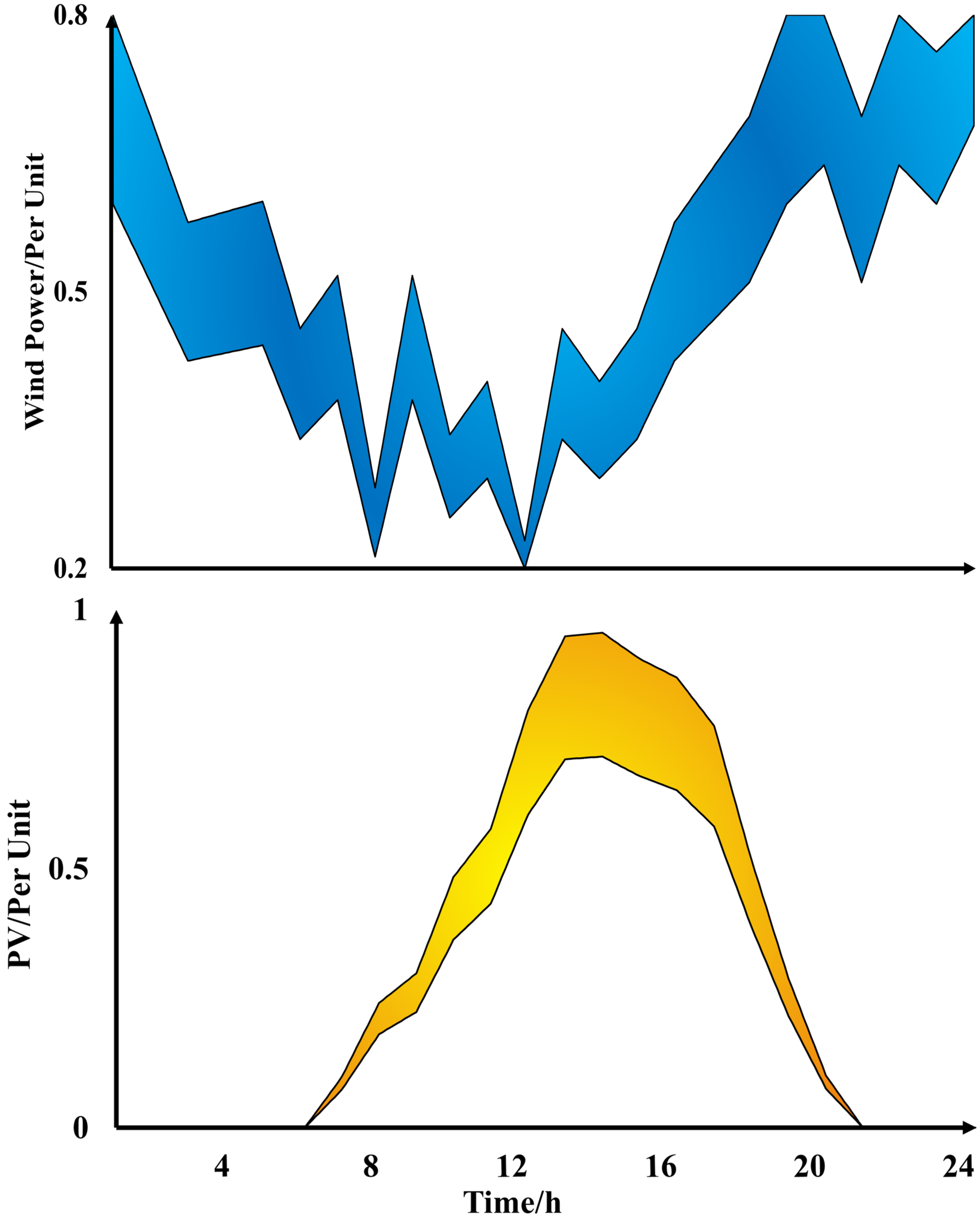

Figure 6.5: Stochastic Daily Profiles of Wind Power & PV

6.4.2 Analysis of Optimal Results

The numerical results of the case studies, along with a comparative analysis between the cases, are presented in Fig 6.6. In Case I, characterised by the independent operation of two energy vectors, the highest operational costs of $6523.30 and the lowest integration of REG (32.74

Table 6.1: Configuration of Two-Stage Stochastic Optimisation Model

	Electric Grid	**Gas Network**
First-Stage Controllable Units	Wind Power, GFUs, P2G	Compressor
Second-Stage Varying Variables	Upstream Power, Voltage, Current, Power Flow	Pressure, Gas Flow, Line Pack

MWh) are incurred.

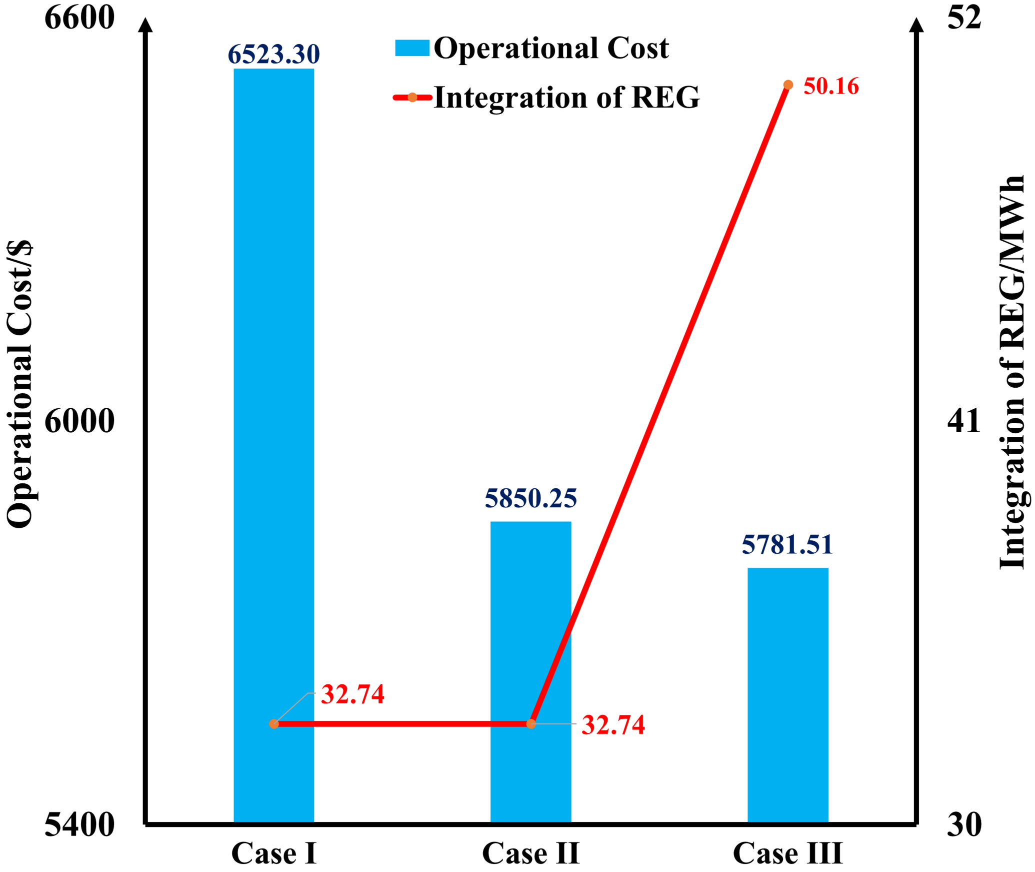

Figure 6.6: Achievements & Comparison of Optimal Results for Each Cases

A distinct downward trajectory in operational costs is observed from Case I through Case III. Transitioning to Case II, the operation of GFUs is involved, resulting in a notable reduction in operational costs to $5850.25, achieving a 10.32% decrease from Case I. Case III takes a further step by fully coupling the electric power grid and the natural gas network through both the GFUs and the P2G unit, causing an additional decrease in operational costs, marking a 1.18% reduction from Case II.

In terms of the integration of REG, the result shows the same value of 32.74 MWh in both Case I and II, implying that without the inclusion of the P2G unit, the capability to enhance REG integration remains unchanged, regardless of other operational adjustments (e.g. GFUs) in the MES. A notable shift occurs in Case III, where the integration of REG dramatically increases to 50.16 MWh, representing a substantial 53.18% increase compared to the REG integration levels in Case I and II. This marked improvement in Case III can be attributed to the incorporation of the P2G unit into the MES.

Collectively, these findings elucidate the proposed method's effectiveness in not only reducing operational costs but also in increasing the accommodation of REG, particularly with a P2G unit incorporated in the MES.

6.4.3 Analysis of Electricity Profiles

In Fig 6.7, the hourly electricity profiles of the upstream power, GFUs, REG and P2G unit are presented. The profiles reveal a significant reduction of 60.18% in upstream power, decreasing from 18.02 MWh in Case I to 7.18 MWh in both Cases II and III. This notable decrease is attributed to the transition from a complete absence of GFU units in Case I to their consistent presence (10.87 MWh) in Cases II and III.

In Cases I and II, the REG maintain a steady output of 32.74 MWh. However, a substantial increase to 50.16 MWh in REG output is noted in Case III. Also, the output power of GFUs in Cases II and III has the same value. Additionally, Case III is distinguished by the P2G

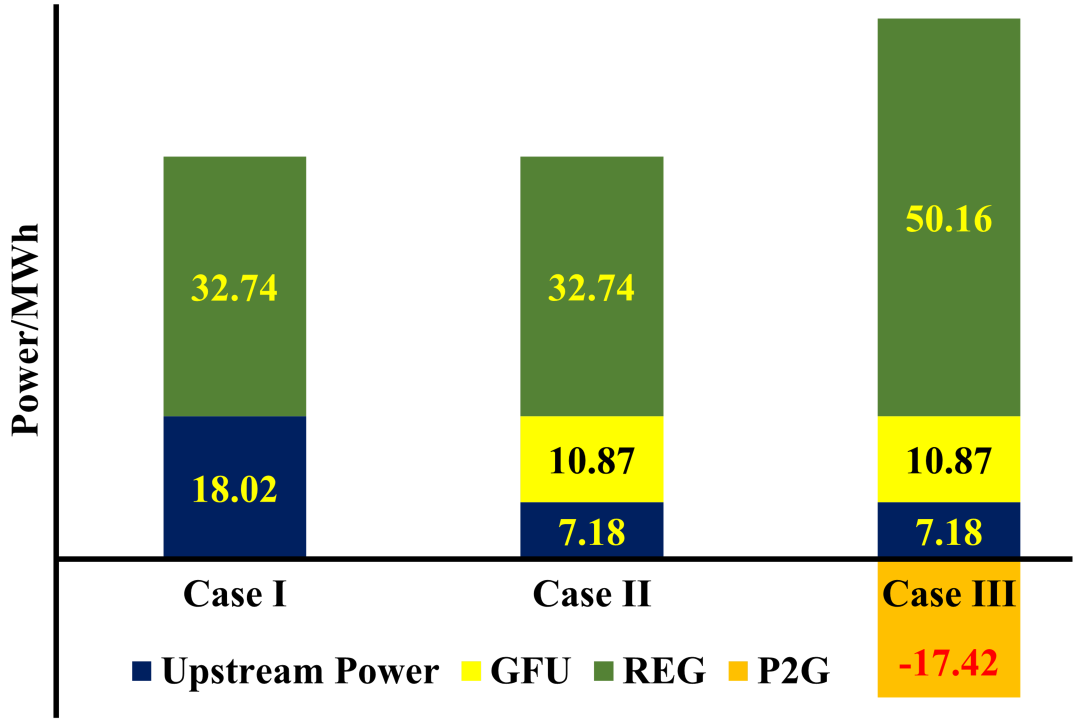

Figure 6.7: Profiles of Electricity for Three Cases

unit's negative value of -17.42 MWh, indicating its role in absorbing electrical energy from the power system. The quantity of energy absorbed by the P2G unit, 17.42 MWh, is nearly equivalent to the differential in REG output between Case III and the earlier Cases I and II. This correlation highlights the P2G unit's significant contribution to enhancing the integration of REG in the EN-MES.

6.4.4 Analysis of Gas Profiles

Fig 6.8 shows the hourly total output of two gas wells. The hourly profiles of electricity consumed by the three compressors are presented in Fig 6.9.

In all three cases, although different in figures, the gas wells exhibit a similar pattern of operations. The first increase, or 'spike', in gas output is observed at hour 2, directly attributed to a

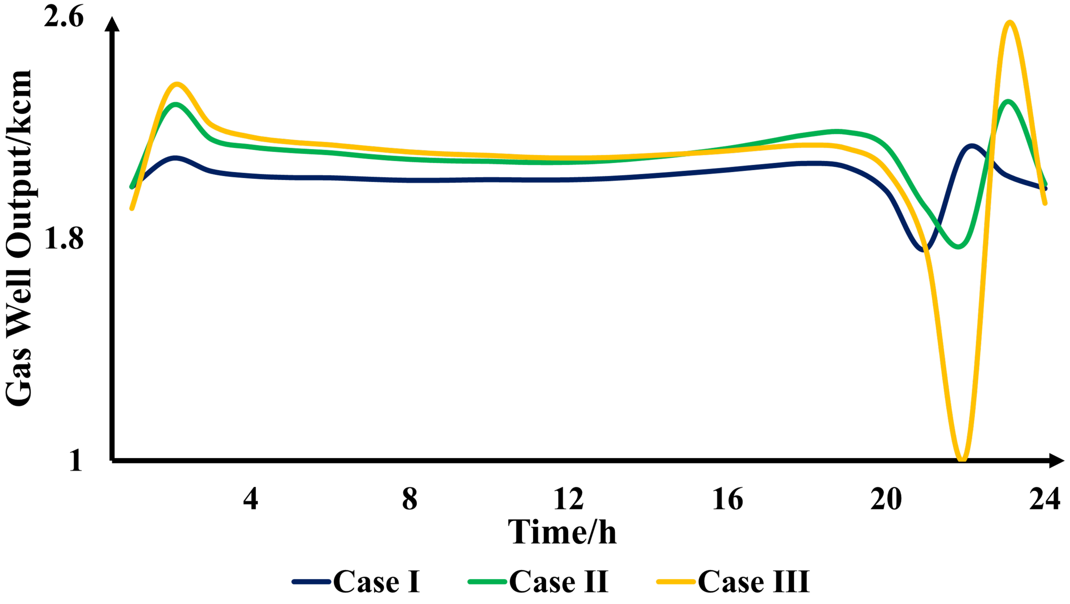

Figure 6.8: Hourly Profiles of Gas Wells

demand surge in gas load between hours 2 and 4 as shown in Fig 6.4. A proactive measure is taken to charge the gas pipelines, ensuring that the pipeline system has sufficient linepack to handle the upcoming spike in gas demand. Furthermore, During the post-hour 20 period, the gas wells perform a sudden and substantial increase in gas output, driven by two key factors: firstly, the evident surge in gas load demand occurs between hours 20 and 23 and, thus, a corresponding increase in gas output is required to meet the demand effectively; secondly, due to the operational constraints (6.34) of gas pipelines that the line pack - the amount of gas stored within the pipeline system - must be restored to its original values. Therefore, the gas output of gas wells is adjusted to meet immediate demand and ensure compliance with the operational constraints.

For the compressors, in all three cases, compressor C2 operates with notably higher power consumption, given its location along the central pipeline, distinguishing it from C1 and C3. Most compressors operated consistently at their individual power level from hour 2 to hour 20. In Cases I and II, compressor C2 exhibits an increase in power consumption at hour 22,

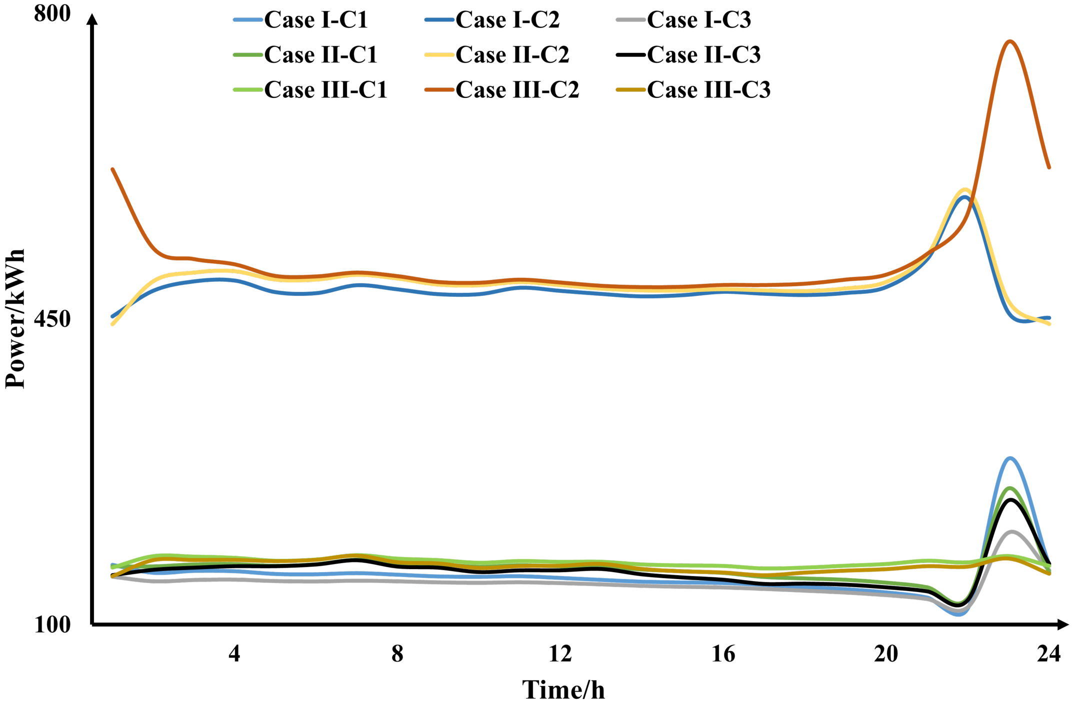

Figure 6.9: Power Consumption of Compressors

whereas compressors C1 and C3 show a similar increase at hour 23. In contrast, during Case III, the power consumption profiles of compressors C1 and C3 remained stable throughout the whole period. However, in comparison with Cases I and II, compressor C2 experienced a sharp rise in power consumption. These variations in the final hours are attributable to the compressors' function in reinstating the line pack to its original levels.

6.4.5 Visualisations of Graph Structure

The visualisation capabilities of the graph-based modelling, conducted by Plasmo.jl, are illustrated in Fig 6.10, 6.11 and 6.12.

As an illustrative example, a visualisation of a 20-bus power grid, comprising 20 buses and 19 branches, is presented in Fig 6.10. The power grid is constructed as an Opti-graph. Within

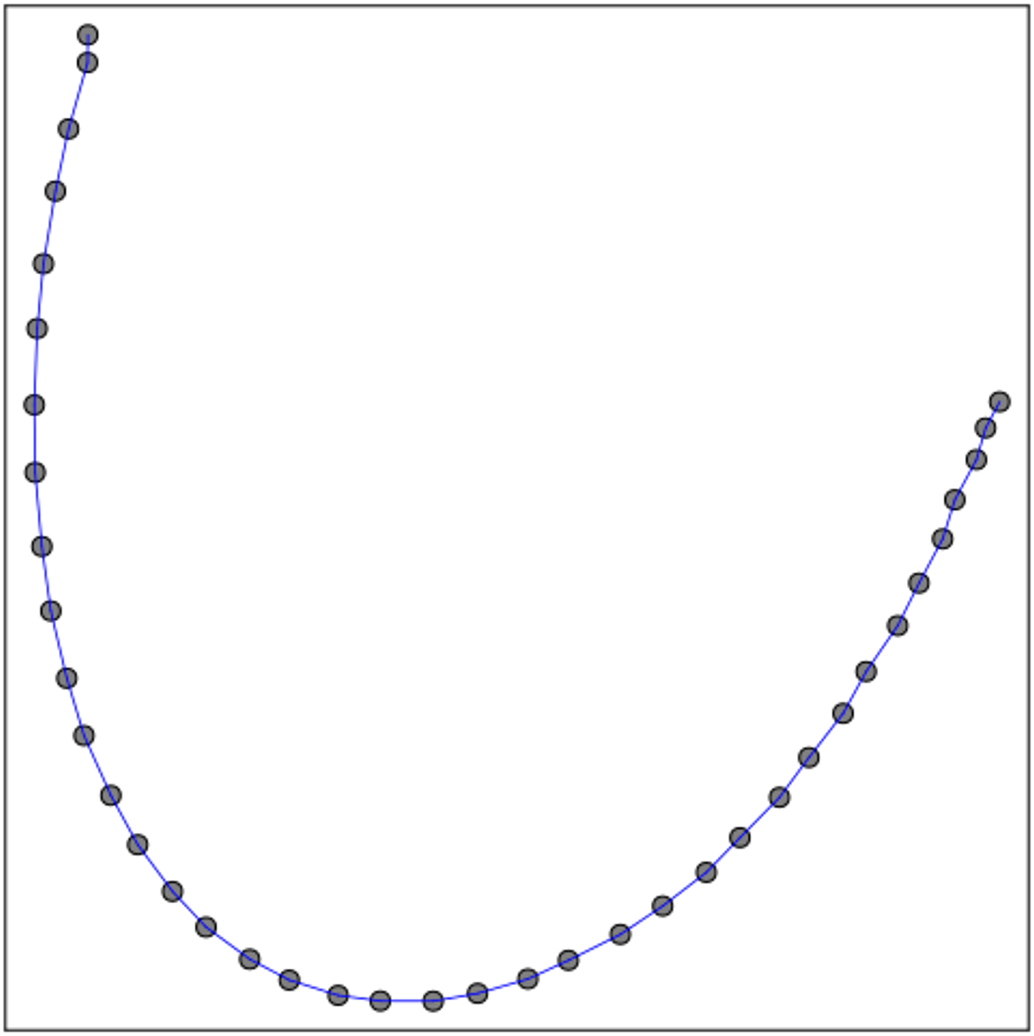

Figure 6.10: Visualisation Example of a 20-Bus Power Gird

the Opti-graph, each bus or branch is modelled as an individual Opti-node, symbolised by a grey dot encircled with a black border. Therefore, the visualised graph for this 20-bus power grid model incorporates, in total, 39 Opti-nodes, corresponding to 39 grey dots with black borders. The interconnecting blue lines between two grey dots denote the Opti-edges, which encapsulate the linking constraints between Opti-nodes. In the same manner of modelling, the visualisation of the electric power grid for the case study, modified from IEEE 123-node test feeder and containing 131 buses, is given in Fig 6.11. The graph was scaled by changing the number of Opti-nodes and Opti-edges within the Opti-graph.

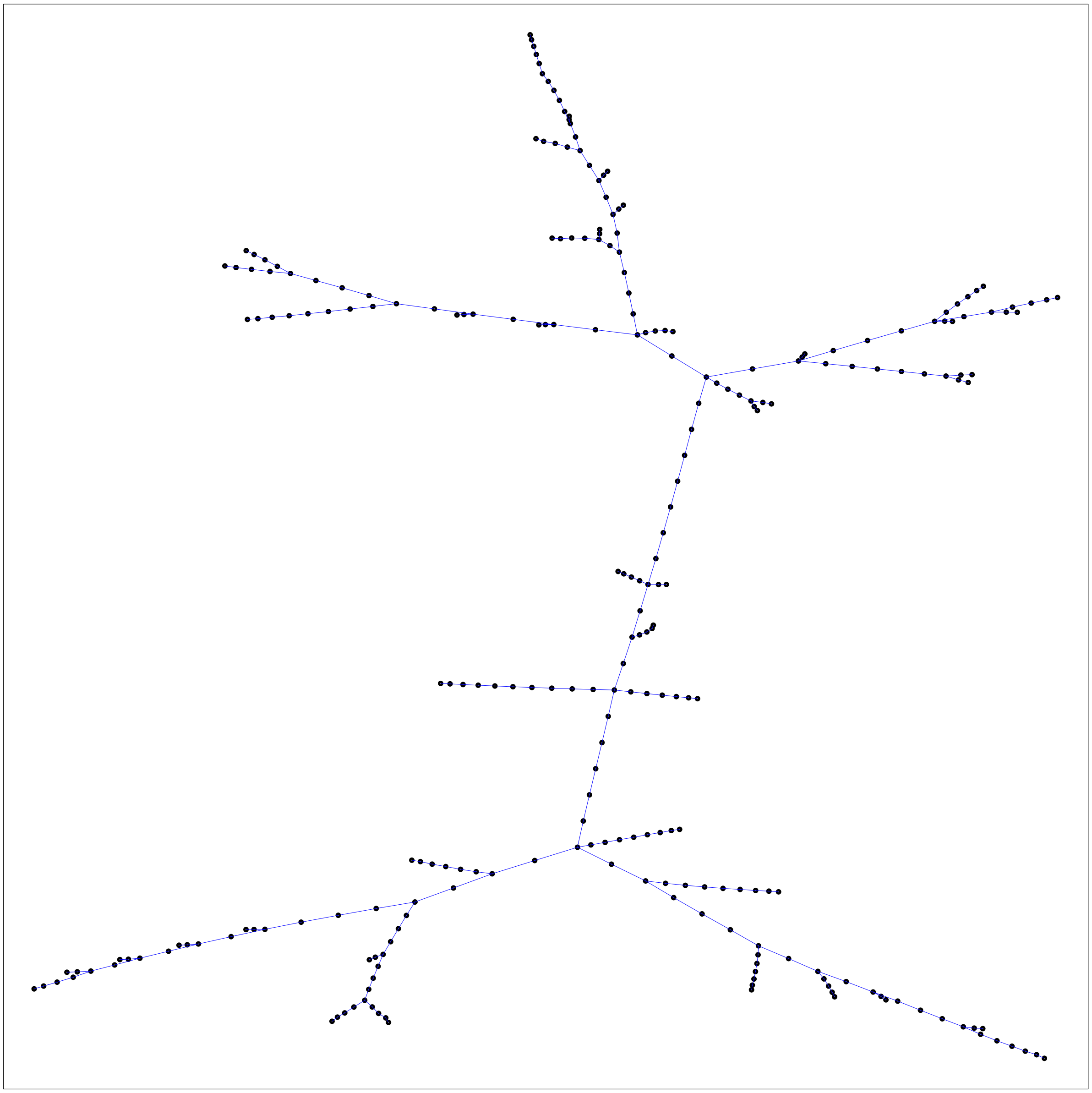

Figure 6.11: Visualisation of the Electric Power Grid for Case Studies

In the visualised natural gas network of Fig 6.12, the modelling approach is similar to the electric power grid. Each gas component, including pipeline, junction or compressor, is modelled as an individual Opti-node, shown as a grey dot encircled with a black border. The Opti-edges, signifying the linking constraints, are represented by the blue lines. The circular formation is resulted from the periodic constraints which mandate that the final linepack in each pipeline must surpass or be equal to the initial value of the linepack of that pipeline. Within each

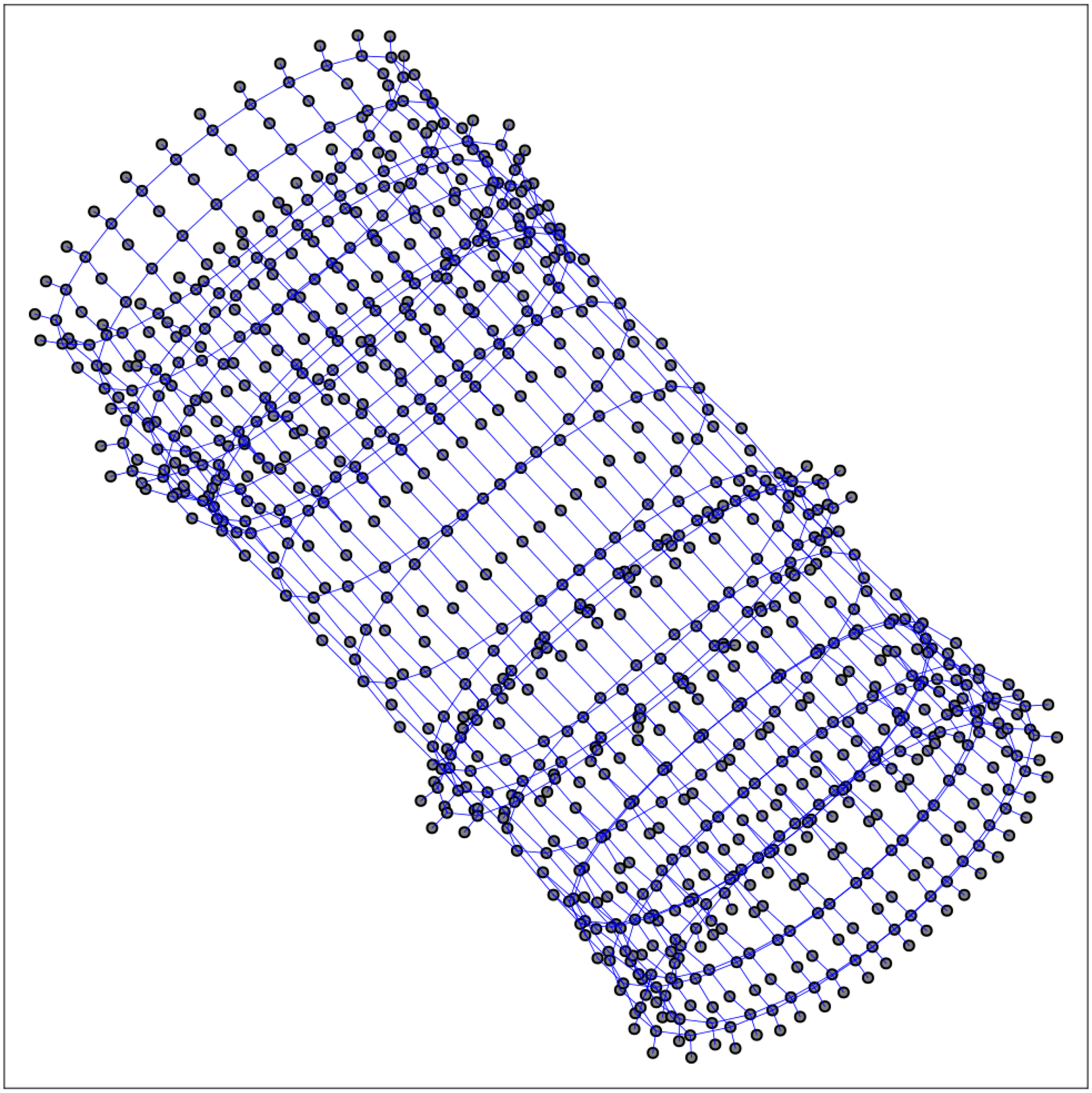

Figure 6.12: Visualisation of the Natural Gas Network for Case Studies

circular layer, 24 Opti-nodes (grey dots) are presented, each corresponding to a time step. Therefore, in the circular layers of each pipeline, the 24 Opti-nodes are interconnected with the blue lines. Conversely, in the layers of each junction or compressor, the Opti-nodes are only connected with adjacent Opti-nodes of pipelines.

6.4.6 Algorithm Performance Evaluation

To test the performance of the graph-structured model, the optimisation problem with different numbers of scenarios is solved with different modelling methods and numbers of threads. As shown in Table II, the Graph-Structured model of 10 scenarios (509040 variables) and 20 scenarios (1018080 variables) are tested in both serial (1 thread) and using parallel multi threads. To compare with the problem model not based on the graph theory, a JuMP model is created and solved with the same solver.

Table 6.2: Solution Times for Different Problem Sizes

Solver/Model	**509040 Variables**	**1018080 Variables**
MA57/Opti-Graph (1 thread)	2860.3s	5854.1s
MA57/Opti-Graph (multi threads)	2375.7s	4717.8s
MA57/JuMP (multi threads)	2787.1s	5763.8s

In the evaluation of the MA57 solver on two distinct models, a noticeable performance differential was observed based on thread configuration and problem size. For the Opti-Graph model, the solver demonstrated a marked improvement in solution time when transitioning from a single-threaded to a multi-threaded approach. Specifically, for the larger problem size with 509040 variables, multi-threading reduced the solution time from 2860.32 to 2375.68 seconds—a 16.9% decrease. A similar trend was evident for the smaller problem size of 101808 variables, with a reduction from 5854.08 seconds in the single-threaded scenario to 4717.76 seconds in the multi-threaded setup, amounting to a 19.4% reduction. This is because, the graph-structured model facilitates parallelisation of both function and derivative evaluations, thereby minimising the overall solution time.

On the other hand, when assessing the JuMP model with multi-threading, the execution times were 2787.04 seconds and 5763.84 seconds for the larger and smaller problem sizes, respectively. These results demonstrate the benefits of a graph-structured model in solving the optimisation problem. Therefore, the Opti-Graph model, with a multi-threaded approach, offers significant computational advantages, underscoring its potential for efficient problem-solving in large datasets.

6.5 Conclusion

In this chapter, a graph-structured model is employed for the first time in addressing the optimisation challenge in electricity and natural gas MES, particularly for modelling and solving the nonlinear optimisation problems. Additionally, to tackle the stochastic challenges posed by REG in MES, a two-stage operational optimisation strategy based on the graph theory is proposed.

The results of the case study demonstrate that the proposed graph-structured two-stage stochastic operational optimisation strategy is effective not only in achieving an optimal power policy for controllable units under various stochastic scenarios but also in minimising the curtailment of REG and reducing overall operational costs. Furthermore, it is proven that the graph-structured method can be applied to the nonlinear optimisation problems of MES and has the capability of visualisation. Also, the significant improvements are highlighted in solving efficiency achieved through the parallelisation of function and derivative evaluations, enhanced by the adoption of decomposition schemes.

Chapter 7

Conclusions & Future Work

7.1 Conclusions

In this thesis, the electricity-gas MES, unlike traditional energy systems that operate in isolation, can embrace the interdependencies between two energy vectors and leverage the strengths of both energy vectors, providing a flexible energy solution to enhance overall system efficiency, reduce operational costs and boost the integration of REG. Within the electric power vector of the MES, the ADN, equipped with the capability of local renewable generation units, flexible power distribution, and energy storage close to the consumers, has evolved from the traditional passive distribution network. The operational optimisation of ADN can not only achieve optimal power flows but also enhance overall grid flexibility and efficiency. The SOP, consisting of the fast-adjustable and controllable power electronic device, can be installed in the normal open points between feeders of ADNs, to realise the reconfiguration and flexible power distribution in the ADN.

The following conclusions are drawn from the research of this thesis where utilising the MES as the key solution, the impact of SOPs on improving the operation of ADNs and the role of MES in facilitating the integration of REGs are investigated.

- The 3P4W-B2B-VSC is employed as the topology of SOP. Building upon this topology, a novel control scheme, termed the ASP control scheme, is developed specifically for the ASP-SOP. The operational strategy of the ASP-SOPs is designed to achieve load balancing across interconnected feeders and to compensate for phase imbalances in the heavily-loaded feeders of the unbalanced ADN. The simulation case studies demonstrate that the 3P4W-B2B-VSC-based ASP-SOP can effectively achieve load balancing and phase imbalance compensation in unbalanced distribution networks.
- With the objectives of reducing both the power loss and the voltage imbalance, an optimal operation strategy based on the developed ASP-SOPs is proposed for unbalanced ADNs. The three-phase OPF optimisation problem is solved by using the symmetrical SDP approach. The case study conducted in the modified IEEE 123-node test system demonstrates that the proposed method can achieve a power loss reduction of up to 49.83% and an imbalance reduction of 69.42%. Similarly, another case study in a 380V 21-node system confirms that the SOP-based optimisation can reduce power loss by up to 48.49% and mitigate the voltage imbalance by 77.68%. Additionally, time-domain simulations of power electronic devices validate that the system-level optimisations are applicable at the device level.
- For electricity-gas MES, a holistic operational coordination optimisation strategy is proposed with the closed energy conversion loop through P2G units and GFUs. The comprehensive model can integrate simultaneous consideration of the phase imbalance in the power distribution system and the line pack dynamics in the natural gas network. Additionally, the impact of the ASP-SOP on the MES is investigated. The results of case

studies indicate that the proposed optimisation method for MESs can reduce the total operational cost by 21.81%, the overall carbon emissions by 33.95% and the curtailment of wind power generations by 94.41%. Furthermore, the implementation of ASP-SOP can significantly mitigate the voltage imbalance condition in three-phase power systems, improving it by up to 36.82%.

- To address the complexities inherent in modelling and solving nonlinear optimisation problems of MES, graph-based modelling is employed to retain the natural characteristics of nonlinear functions and constraints. Meanwhile, to address the stochastic issues posed by REG in MES, a two-stage optimal operation strategy based on the graph theory is developed for MES. Two Julia-based software packages are utilised: Plasmo.jl for constructing and modelling optimisation problems within a graph-based framework, and MadNLP.jl for solving the model. The outcomes of the case study clearly demonstrate that the proposed graph-structured two-stage stochastic operational optimisation strategy is effective for nonlinear optimisation problems of MES not only in achieving optimal operational performance for controllable units under various stochastic scenarios but also in enhancing the integration of REG by 53.21% and reducing overall operational costs by 11.37%. Furthermore, the significant improvements are highlighted in time efficiency achieved through the parallelisation of function and derivative evaluations, enhanced by the adoption of decomposition schemes.

In conclusion, three areas of research are investigated in this thesis, including the device-level topology and control of SOP, the system-level SOP-based optimisation for ADN, and the modelling and optimisation for electricity-gas MES. Firstly, The 3P4W-B2B-VSC is introduced as the new topology for the SOPs. Based on the new topology, the ASP control scheme and the control strategy are developed to achieve load balancing and compensate for phase imbalances in feeders of the unbalanced ADN. Secondly, an optimal operation strategy based on proposed ASP-SOPs is developed for improving the power quality of ADN. Finally, an optimal operational coordination optimisation approach is proposed for electricity-gas MES to increase the system efficiency and the integration of REG.

7.2 Future Work

Potential relevant future research work is proposed and listed as follows:

- For the ASP-SOP, the proposed ASP control and operational strategy are all designed for the steady-state operation of the power grid. To ensure the secure operation of ASP-SOPs in real-world power networks, the control scheme during the transient state operation, the logic of the relay protection and the strategy for the supply restoration should be taken into consideration. The control and operational strategy for the fault conditions and the post-fault supply restoration conditions should be developed. All ASP-SOPs discussed in this thesis fall under the category of B2B SOP, indicating that the multi-terminal SOP has not been subject to analysis. Meanwhile, although the time-domain simulations of power electronic devices and the system-level optimisation have mutually validated and corroborated each other's results, the hardware experiment can be conducted in the future to further verify the feasibility and effectiveness of the ASP-SOPs.
- The technological advantages of ASP-SOPs have been explored in this thesis. To further ascertain the feasibility of deploying ASP-SOPs compared with traditional SOPs, a comprehensive economic assessment, encompassing the cost factors, including man-

ufacturing, installation, maintenance, and operation, should be conducted. Moreover, an evaluation of the life cycle costs for ASP-SOPs can be conducted to make a comparison with the traditional SOPs. Additionally, the focuses of this thesis concentrate on the operational optimisation strategy of the ASP-SOP. The research of the optimal planning strategy, which aims to determine the optimal quantity, the installation location and the capacity of the ASP-SOP, should be essential when considering both capital and operational expenditures.

- In this research, the MESs have primarily addressed the energy vectors of electricity and natural gas. Future studies could expand this scope to encompass the coupling of different energy vectors, including heating, cooling, and hydrogen. In the process of conducting optimisation, this research primarily concentrates on achieving optimal operational performance of the MES. In practical applications, the planning optimisation of MES plays a pivotal role in minimising capital investments, maximising the energy utilisation efficiency of various energy vectors, and reducing carbon footprints. The significance of planning optimisation can become increasingly critical in scenarios where an MES aims to integrate a diverse array of energy vectors. Furthermore, on the demand side, the stochastics of energy demand and the demand-side management, specifically the demand response, can be incorporated into the operational optimisation of the MES.

Appendix A

IEEE test feeders

IEEE 123-node test feeder

The IEEE 123-node test feeder operates at a nominal voltage of 4.16 kV. While this is not a popular voltage level it does provide voltage drop problems that must be solved with the application of voltage regulators and shunt capacitors. This circuit is characterized by overhead and underground lines, unbalanced loading with constant current, impedance, and power, four voltage regulators, shunt capacitor banks, and multiple switches. This circuit is “well-behaved” with minimal convergence problems [171].

Table A1: Regulator Data of the IEEE 123-Node Test Feeder

Regulator ID:	1			Regulator ID:	3		
Line Segment:	150 - 149			Line Segment:	25 - 26		
Location:	150			Location:	25		
Phases:	A-B-C			Phases:	A-C		
Connection:	3-Ph, Wye			Connection:	2-Ph,L-G		
Monitoring Phase:	A			Monitoring Phase:	A & C		
Bandwidth:	2.0 volts			Bandwidth:	1		
PT Ratio:	20			PT Ratio:	20		
Primary CT Rating:	700			Primary CT Rating:	50		
Compensator:	Ph-A	Ph-B	Ph-C	Compenator:	Ph-A	Ph-B	Ph-C
R - Setting:	3	-	-	R - Setting:	0.4	-	0.4
X - Setting:	7.5	-	-	X - Setting:	0.4	-	0.4
Voltage Level:	120	-	-	Voltage Level:	120	-	120

Regulator ID:	2			Regulator ID:	4		
Line Segment:	9 - 14			Line Segment:	160 - 67		
Location:	9			Location:	160		
Phases:	A			Phases:	A-B-C		
Connection:	1-Ph, L-G			Connection:	3-Ph, LG		
Monitoring Phase:	A			Monitoring Phase:	A-B-C		
Bandwidth:	2.0 volts			Bandwidth:	2		
PT Ratio:	20			PT Ratio:	20		
Primary CT Rating:	50			Primary CT Rating:	300		
Compensator:	Ph-A	Ph-B	Ph-C	Compensator:	Ph-A	Ph-B	Ph-C
R - Setting:	0.4	-	-	R - Setting:	0.6	1.4	0.2
X - Setting:	0.4	-	-	X - Setting:	1.3	2.6	1.4
Voltage Level:	120	-	-	Voltage Level:	124	124	124

Table A2: Line Segment Data of the IEEE 123-Node Test Feeder

Node A	Node B	Length (ft.)	Config.	Node A	Node B	Length (ft.)	Config.
1	2	175	10	60	61	550	5
1	3	250	11	60	62	250	12
1	7	300	1	62	63	175	12
3	4	200	11	63	64	350	12
3	5	325	11	64	65	425	12
5	6	250	11	65	66	325	12
7	8	200	1	67	68	200	9
8	12	225	10	67	72	275	3
8	9	225	9	67	97	250	3
8	13	300	1	68	69	275	9
9	14	425	9	69	70	325	9
13	34	150	11	70	71	275	9
13	18	825	2	72	73	275	11
14	11	250	9	72	76	200	3
14	10	250	9	73	74	350	11
15	16	375	11	74	75	400	11
15	17	350	11	76	77	400	6
18	19	250	9	76	86	700	3
18	21	300	2	77	78	100	6
19	20	325	9	78	79	225	6
21	22	525	10	78	80	475	6
21	23	250	2	80	81	475	6
23	24	550	11	81	82	250	6
23	25	275	2	81	84	675	11
25	26	350	7	82	83	250	6
25	28	200	2	84	85	475	11
26	27	275	7	86	87	450	6
26	31	225	11	87	88	175	9
27	33	500	9	87	89	275	6
28	29	300	2	89	90	225	10
29	30	350	2	89	91	225	6
30	250	200	2	91	92	300	11
31	32	300	11	91	93	225	6
34	15	100	11	93	94	275	9
35	36	650	8	93	95	300	6
35	40	250	1	95	96	200	10
36	37	300	9	97	98	275	3
36	38	250	10	98	99	550	3
38	39	325	10	99	100	300	3
40	41	325	11	100	450	800	3
40	42	250	1	101	102	225	11
42	43	500	10	101	105	275	3
42	44	200	1	102	103	325	11
44	45	200	9	103	104	700	11
44	47	250	1	105	106	225	10
45	46	300	9	105	108	325	3
47	48	150	4	106	107	575	10
47	49	250	4	108	109	450	9
49	50	250	4	108	300	1000	3
50	51	250	4	109	110	300	9
51	151	500	4	110	111	575	9
52	53	200	1	110	112	125	9
53	54	125	1	112	113	525	9
54	55	275	1	113	114	325	9
54	57	350	3	135	35	375	4
55	56	275	1	149	1	400	1
57	58	250	10	152	52	400	1
57	60	750	3	160	67	350	6
58	59	250	10	197	101	250	3

Table A3: Spot Loads of the IEEE 123-Node Test Feeder

Node	Load Model	Ph-1 kW	Ph-1 kVAr	Ph-2 kW	Ph-2 kVAr	Ph-3 kW	Ph-4 kVAr	Node	Load Model	Ph-1 kW	Ph-1 kVAr	Ph-2 kW	Ph-2 kVAr	Ph-3 kW	Ph-4 kVAr
1	Y-PQ	40	20	0	0	0	0	60	Y-PQ	20	10	0	0	0	0
2	Y-PQ	0	0	20	10	0	0	62	Y-Z	0	0	0	0	40	20
4	Y-PR	0	0	0	0	40	20	63	Y-PQ	40	20	0	0	0	0
5	Y-I	0	0	0	0	20	10	64	Y-I	0	0	75	35	0	0
6	Y-Z	0	0	0	0	40	20	65	D-Z	35	25	35	25	70	50
7	Y-PQ	20	10	0	0	0	0	66	Y-PQ	0	0	0	0	75	35
9	Y-PQ	40	20	0	0	0	0	68	Y-PQ	20	10	0	0	0	0
10	Y-I	20	10	0	0	0	0	69	Y-PQ	40	20	0	0	0	0
11	Y-Z	40	20	0	0	0	0	70	Y-PQ	20	10	0	0	0	0
12	Y-PQ	0	0	20	10	0	0	71	Y-PQ	40	20	0	0	0	0
16	Y-PQ	0	0	0	0	40	20	73	Y-PQ	0	0	0	0	40	20
17	Y-PQ	0	0	0	0	20	10	74	Y-Z	0	0	0	0	40	20
19	Y-PQ	40	20	0	0	0	0	75	Y-PQ	0	0	0	0	40	20
20	Y-I	40	20	0	0	0	0	76	D-I	105	80	70	50	70	50
22	Y-Z	0	0	40	20	0	0	77	Y-PQ	0	0	40	20	0	0
24	Y-PQ	0	0	0	0	40	20	79	Y-Z	40	20	0	0	0	0
28	Y-I	40	20	0	0	0	0	80	Y-PQ	0	0	40	20	0	0
29	Y-Z	40	20	0	0	0	0	82	Y-PQ	40	20	0	0	0	0
30	Y-PQ	0	0	0	0	40	20	83	Y-PQ	0	0	0	0	20	10
31	Y-PQ	0	0	0	0	20	10	84	Y-PQ	0	0	0	0	20	10
32	Y-PQ	0	0	0	0	20	10	85	Y-PQ	0	0	0	0	40	20
33	Y-I	40	20	0	0	0	0	86	Y-PQ	0	0	20	10	0	0
34	Y-Z	0	0	0	0	40	20	87	Y-PQ	0	0	40	20	0	0
35	D-PQ	40	20	0	0	0	0	88	Y-PQ	40	20	0	0	0	0
37	Y-Z	40	20	0	0	0	0	90	Y-I	0	0	40	20	0	0
38	Y-I	0	0	20	10	0	0	92	Y-PQ	0	0	0	0	40	20
39	Y-PQ	0	0	20	10	0	0	94	Y-PQ	40	20	0	0	0	0
41	Y-PQ	0	0	0	0	20	10	95	Y-PQ	0	0	20	10	0	0
42	Y-PQ	20	10	0	0	0	0	96	Y-PQ	0	0	20	10	0	0
43	Y-Z	0	0	40	20	0	0	98	Y-PQ	40	20	0	0	0	0
45	Y-I	20	10	0	0	0	0	99	Y-PQ	0	0	40	20	0	0
46	Y-PQ	20	10	0	0	0	0	100	Y-Z	0	0	0	0	40	20
47	Y-I	35	25	35	25	35	25	102	Y-PQ	0	0	0	0	20	10
48	Y-Z	70	50	70	50	70	50	103	Y-PQ	0	0	0	0	40	20
49	Y-PQ	35	25	70	50	35	20	104	Y-PQ	0	0	0	0	40	20
50	Y-PQ	0	0	0	0	40	20	106	Y-PQ	0	0	40	20	0	0
51	Y-PQ	20	10	0	0	0	0	107	Y-PQ	0	0	40	20	0	0
52	Y-PQ	40	20	0	0	0	0	109	Y-PQ	40	20	0	0	0	0
53	Y-PQ	40	20	0	0	0	0	111	Y-PQ	20	10	0	0	0	0
55	Y-Z	20	10	0	0	0	0	112	Y-I	20	10	0	0	0	0
56	Y-PQ	0	0	20	10	0	0	113	Y-Z	40	20	0	0	0	0
58	Y-I	0	0	20	10	0	0	114	Y-PQ	20	10	0	0	0	0
59	Y-PQ	0	0	20	10	0	0	Total		1420	775	915	515	1155	630

Table A4: Overhead Line Configurations of the IEEE 123-Node Test Feeder

Config.	Phasing	Phase Cond.	Neutral Cond.	Spacing
		ACSR	ACSR	ID
1	A B C N	336,400 26/7	4/0 6/1	500
2	C A B N	336,400 26/7	4/0 6/1	500
3	B C A N	336,400 26/7	4/0 6/1	500
4	C B A N	336,400 26/7	4/0 6/1	500
5	B A C N	336,400 26/7	4/0 6/1	500
6	A C B N	336,400 26/7	4/0 6/1	500
7	A C N	336,400 26/7	4/0 6/1	505
8	A B N	336,400 26/7	4/0 6/1	505
9	A N	1/0	1/0	510
10	B N	1/0	1/0	510
11	C N	1/0	1/0	510

Table A5: Transformer Data of the IEEE 123-Node Test Feeder

	kVA	kV-high	kV-low	R - %	X - %
Substation	5,000	115 - D	4.16 Gr-W	1	8
XFM - 1	150	4.16 - D	.480 - D	1.27	2.72

Table A6: Underground Line Configuration (Config.) of the IEEE 123-Node Test Feeder

Config.	Phasing	Cable	Spacing ID
12	A B C	1/0 AA, CN	515

Table A7: Three Phase Switches of the IEEE 123-Node Test Feeder

Node A	13	18	60	61	97	150	250	450	54	151	300
Node B	152	135	160	610	197	149	251	451	94	300	350
Normal	closed	closed	closed	closed	closed	closed	open	open	open	open	open

Table A8: IEEE 123-Node Test Feeder Impedance

Configuration 1:

```
          Z (R +jX) in ohms per mile
0.4576  1.0780   0.1560  0.5017   0.1535  0.3849
                 0.4666  1.0482   0.1580  0.4236
                                  0.4615  1.0651
         B in micro Siemens per mile
           5.6765   -1.8319   -0.6982
                     5.9809   -1.1645
                               5.3971
```

Configuration 2:

```
          Z (R +jX) in ohms per mile
0.4666  1.0482   0.1580  0.4236   0.1560  0.5017
                 0.4615  1.0651   0.1535  0.3849
                                  0.4576  1.0780
         B in micro Siemens per mile
           5.9809   -1.1645   -1.8319
                     5.3971   -0.6982
                               5.6765
```

Configuration 3:

```
          Z (R +jX) in ohms per mile
0.4615  1.0651   0.1535  0.3849   0.1580  0.4236
                 0.4576  1.0780   0.1560  0.5017
                                  0.4666  1.0482
         B in micro Siemens per mile
           5.3971   -0.6982   -1.1645
                     5.6765   -1.8319
                               5.9809
```

Configuration 4:

```
          Z (R +jX) in ohms per mile
0.4615  1.0651   0.1580  0.4236   0.1535  0.3849
                 0.4666  1.0482   0.1560  0.5017
                                  0.4576  1.0780
         B in micro Siemens per mile
           5.3971   -1.1645   -0.6982
                     5.9809   -1.8319
                               5.6765
```

Configuration 5:

```
          Z (R +jX) in ohms per mile
0.4666  1.0482   0.1560  0.5017   0.1580  0.4236
                 0.4576  1.0780   0.1535  0.3849
                                  0.4615  1.0651
         B in micro Siemens per mile
           5.9809   -1.8319   -1.1645
                     5.6765   -0.6982
                               5.3971
```

Configuration 6:

```
          Z (R +jX) in ohms per mile
0.4576  1.0780   0.1535  0.3849   0.1560  0.5017
                 0.4615  1.0651   0.1580  0.4236
                                  0.4666  1.0482
         B in micro Siemens per mile
           5.6765   -0.6982   -1.8319
                     5.3971   -1.1645
                               5.9809
```

Configuration 7:

```
          Z (R +jX) in ohms per mile
0.4576  1.0780   0.0000  0.0000   0.1535  0.3849
                 0.0000  0.0000   0.0000  0.0000
                                  0.4615  1.0651
         B in micro Siemens per mile
           5.1154    0.0000   -1.0549
                     0.0000    0.0000
                               5.1704
```

Configuration 8:

```
          Z (R +jX) in ohms per mile
0.4576  1.0780   0.1535  0.3849   0.0000  0.0000
                 0.4615  1.0651   0.0000  0.0000
                                  0.0000  0.0000
         B in micro Siemens per mile
           5.1154   -1.0549    0.0000
                     5.1704    0.0000
                               0.0000
```

Configuration 9:

```
          Z (R +jX) in ohms per mile
 1.3292  1.3475   0.0000  0.0000   0.0000  0.0000
                  0.0000  0.0000   0.0000  0.0000
                                   0.0000  0.0000
         B in micro Siemens per mile
           4.5193    0.0000    0.0000
                     0.0000    0.0000
                               0.0000
```

Configuration 10:

```
          Z (R +jX) in ohms per mile
 0.0000  0.0000   0.0000  0.0000   0.0000  0.0000
                  1.3292  1.3475   0.0000  0.0000
                                   0.0000  0.0000
         B in micro Siemens per mile
           0.0000    0.0000    0.0000
                     4.5193    0.0000
                               0.0000
```

Configuration 11:

```
          Z (R +jX) in ohms per mile
 0.0000  0.0000   0.0000  0.0000   0.0000  0.0000
                  0.0000  0.0000   0.0000  0.0000
                                   1.3292  1.3475
         B in micro Siemens per mile
           0.0000    0.0000    0.0000
                     0.0000    0.0000
                               4.5193
```

Configuration 12:

```
          Z (R +jX) in ohms per mile
 1.5209  0.7521   0.5198  0.2775   0.4924  0.2157
                  1.5329  0.7162   0.5198  0.2775
                                   1.5209  0.7521
         B in micro Siemens per mile
          67.2242    0.0000    0.0000
                    67.2242    0.0000
                              67.2242
```

Bibliography

[1] GOV.UK, “Uk becomes first major economy to pass net zero emissions law.” `http://bit.ly/3O8cJzF`, 2019. Accessed: 14-Jan-2024.

[2] UK.Parliament, “Net zero in the uk.” `https://commonslibrary.parliament.uk/research-briefings/cbp-8590/`, 2019. Accessed: 15-Jan-2024.

[3] J. Deutch, “Is net zero carbon 2050 possible?,” *Joule*, vol. 4, no. 11, pp. 2237–2240, 2020.

[4] S. Mazumdar, D. Thakker, J. Hayes, N. Matos, and P. Bate, “Towards achieving net zero by 2050 in the uk–stakeholder perspectives in integrated urban planning,” *Futures*, p. 103197, 2023.

[5] P. C. Slorach and L. Stamford, “Net zero in the heating sector: Technological options and environmental sustainability from now to 2050,” *Energy Conversion and Management*, vol. 230, p. 113838, 2021.

[6] E. UK and I. Strategy, “‘energy white paper: Powering our net zero future,” *Dept. Bus., Energy Ind. Strategy, UK, Tech. Rep. CCS0220144090, CP*, vol. 337, 2020.

[7] M. Royapoor, A. Allahham, S. H. R. Hosseini, N. A. Rufa'I, and S. L. Walker, "Towards 2050 net zero carbon infrastructure: a critical review of key decarbonization challenges in the domestic heating sector in the uk," *Energy Sources, Part B: Economics, Planning, and Policy*, vol. 18, no. 1, p. 2272264, 2023.

[8] M. D. Galus and G. Andersson, "Integration of plug-in hybrid electric vehicles into energy networks," in *2009 IEEE Bucharest PowerTech*, pp. 1–8, IEEE, 2009.

[9] D. Devoy, E. Wells, R. Lodhia, M. Moran, M. Bray, and C. A. Smith, "The use of multi-purpose interconnectors to meet net zero by 2050," in *The 17th International Conference on AC and DC Power Transmission (ACDC 2021)*, vol. 2021, pp. 150–154, IET, 2021.

[10] Y. Zou, Y. Xu, X. Feng, R. Naayagi, and B.-H. Soong, "Transactive energy systems in active distribution networks: A comprehensive review," *CSEE Journal of Power and Energy Systems*, vol. 8, no. 5, pp. 1302–1317, 2022.

[11] J. Liu, H. Gao, Z. Ma, and Y. Li, "Review and prospect of active distribution system planning," *Journal of Modern Power Systems and Clean Energy*, vol. 3, no. 4, pp. 457–467, 2015.

[12] P. Li, Y. Wang, H. Ji, J. Zhao, G. Song, J. Wu, and C. Wang, "Operational flexibility of active distribution networks: Definition, quantified calculation and application," *International Journal of Electrical Power & Energy Systems*, vol. 119, p. 105872, 2020.

[13] P. Cong, Z. Hu, W. Tang, C. Lou, and L. Zhang, "Optimal allocation of soft open points in active distribution network with high penetration of renewable energy generations," *IET Generation, Transmission & Distribution*, vol. 14, no. 26, pp. 6732–6740, 2020.

[14] W. Chengshan, S. Chongbo, L. Peng, *et al.*, "Optimization and analysis of distribution network operation based on snop [j]," *Automation of electric power systems*, vol. 39, no. 09, pp. 82–87, 2015.

[15] J. M. Bloemink and T. C. Green, "Increasing distributed generation penetration using soft normally-open points," in *IEEE PES general meeting*, pp. 1–8, IEEE, 2010.

[16] W. Wang, S. Huang, G. Zhang, J. Liu, and Z. Chen, "Optimal operation of an integrated electricity-heat energy system considering flexible resources dispatch for renewable integration," *Journal of Modern Power Systems and Clean Energy*, vol. 9, no. 4, pp. 699–710, 2021.

[17] Y. Huo, P. Li, H. Ji, J. Yan, G. Song, J. Wu, and C. Wang, "Data-driven adaptive operation of soft open points in active distribution networks," *IEEE Transactions on Industrial Informatics*, vol. 17, no. 12, pp. 8230–8242, 2021.

[18] Z. Li, Z. Wu, L. Jiang, H. Zhu, M. Meng, Y. Wei, and G. Zhu, "Research on optimal operation of ac/dc active distribution network based on sop," in *IOP Conference Series: Materials Science and Engineering*, vol. 446, p. 012014, IOP Publishing, 2018.

[19] P. S. Onen, G. Mokryani, and R. H. Zubo, "Planning of multi-vector energy systems with high penetration of renewable energy source: A comprehensive review," *Energies*, vol. 15, no. 15, p. 5717, 2022.

[20] J. Reynolds, M. W. Ahmad, and Y. Rezgui, "Holistic modelling techniques for the operational optimisation of multi-vector energy systems," *Energy and Buildings*, vol. 169, pp. 397–416, 2018.

[21] E. U. Institute, “Sector coupling and energy system integration.” `https://fsr.eui.eu/sector-coupling-and-energy-system-integration/`, 2018. Accessed: 24-Jan-2024.

[22] H. Fan, Q. Yuan, S. Xia, J. Lu, and Z. Li, “Optimally coordinated expansion planning of coupled electricity, heat and natural gas infrastructure for multi-energy system,” *IEEE Access*, vol. 8, pp. 91139–91149, 2020.

[23] W. Huang, N. Zhang, Y. Wang, T. Capuder, I. Kuzle, and C. Kang, “Matrix modeling of energy hub with variable energy efficiencies,” *International Journal of Electrical Power & Energy Systems*, vol. 119, p. 105876, 2020.

[24] H. Fan, J. Lu, Z. Li, M. Shahidehpour, and S. Zhang, “Optimal planning of integrated electricity-gas system with demand side management,” *Ieee Access*, vol. 7, pp. 176790–176798, 2019.

[25] C. Andrade, S. Selosse, and N. Maïzi, “The role of power-to-gas in the integration of variable renewables,” *Applied Energy*, vol. 313, p. 118730, 2022.

[26] C. Wang, S. Dong, S. Xu, M. Yang, S. He, X. Dong, and J. Liang, “Impact of power-to-gas cost characteristics on power-gas-heating integrated system scheduling,” *IEEE Access*, vol. 7, pp. 17654–17662, 2019.

[27] F. Kholardi, M. Assili, M. A. Lasemi, and A. Hajizadeh, “Optimal management of energy hub with considering hydrogen network,” in *2018 International Conference on Smart Energy Systems and Technologies (SEST)*, pp. 1–6, IEEE, 2018.

[28] M. Lynch, M. T. Devine, and V. Bertsch, “The role of power-to-gas in the future energy system: Market and portfolio effects,” *Energy*, vol. 185, pp. 1197–1209, 2019.

[29] K. H. M. Azmi, N. A. M. Radzi, N. A. Azhar, F. S. Samidi, I. T. Zulkifli, and A. M. Zainal, “Active electric distribution network: Applications, challenges, and opportunities,” *IEEE Access*, 2022.

[30] T. Yang, “Ict technologies standards and protocols for active distribution network,” in *Smart power distribution systems*, pp. 205–230, Elsevier, 2019.

[31] K. Prakash, A. Lallu, F. Islam, and K. Mamun, “Review of power system distribution network architecture,” in *2016 3rd Asia-Pacific World Congress on Computer Science and Engineering (APWC on CSE)*, pp. 124–130, IEEE, 2016.

[32] B. Hayes, “Distribution generation optimization and energy management,” *Distributed Generation Systems; Gharehpetian, GB, Agah, SMM, Eds.; Elsevier Inc.: Oxford, UK*, pp. 415–451, 2017.

[33] A. Korbik, S. D. McARTHUR, G. W. Ault, G. M. Burt, and J. R. McDONALD, “Enabling active distribution networks through decentralised autonomous network management,” in *CIRED 2005-18th International Conference and Exhibition on Electricity Distribution*, pp. 1–5, IET, 2005.

[34] C. Adamo, S. Jupe, and C. Abbey, “Development and operation of active distribution networks,” *CIGRE Working Group C*, vol. 6, 2011.

[35] L. F. Ochoa, C. J. Dent, and G. P. Harrison, “Distribution network capacity assessment: Variable dg and active networks,” *IEEE Transactions on Power Systems*, vol. 25, no. 1, pp. 87–95, 2009.

[36] S. Bu, L. G. Meegahapola, D. P. Wadduwage, and A. M. Foley, “Stability and dynamics of active distribution networks (adns) with d-pmu technology: a review,” *IEEE Transactions on Power Systems*, vol. 38, no. 3, pp. 2791–2804, 2022.

[37] Y. Li, Q. Chen, G. Strbac, K. Hur, and C. Kang, "Active distribution network expansion planning with dynamic thermal rating of underground cables and transformers," *IEEE Transactions on Smart Grid*, 2023.

[38] T. Lv and Q. Ai, "Interactive energy management of networked microgrids-based active distribution system considering large-scale integration of renewable energy resources," *Applied Energy*, vol. 163, pp. 408–422, 2016.

[39] X. Shang, Z. Li, J. Zheng, and Q. Wu, "Equivalent modeling of active distribution network considering the spatial uncertainty of renewable energy resources," *International Journal of Electrical Power & Energy Systems*, vol. 112, pp. 83–91, 2019.

[40] M. A. Al-Jaafreh and G. Mokryani, "Planning and operation of lv distribution networks: a comprehensive review," *IET Energy Systems Integration*, vol. 1, no. 3, pp. 133–146, 2019.

[41] L. Thomas, *Connection imbalance in low voltage distribution networks*. PhD thesis, Cardiff University, 2015.

[42] W. Kong, K. Ma, and Q. Wu, "Three-phase power imbalance decomposition into systematic imbalance and random imbalance," *IEEE Transactions on Power Systems*, vol. 33, no. 3, pp. 3001–3012, 2018.

[43] G. Mokryani, A. Majumdar, and B. C. Pal, "Probabilistic method for the operation of three-phase unbalanced active distribution networks," *IET Renewable Power Generation*, vol. 10, no. 7, pp. 944–954, 2016.

[44] K. Ma, L. Fang, and W. Kong, "Review of distribution network phase unbalance: Scale, causes, consequences, solutions, and future research directions," *CSEE Journal of Power and Energy systems*, vol. 6, no. 3, pp. 479–488, 2020.

[45] T. Xu, J. Pan, Y. Jiang, H. Hou, and Y. Li, "The effect of three-phase voltage imbalance at pcc on solar panel output power," *Procedia Computer Science*, vol. 52, pp. 1218–1224, 2015.

[46] J. Aramizu and J. C. Vieira, "Analysis of pv generation impacts on voltage imbalance and on voltage regulation in distribution networks," in *2013 IEEE Power & Energy Society General Meeting*, pp. 1–5, IEEE, 2013.

[47] W. Kong, K. Ma, and Q. Wu, "Three-phase power imbalance decomposition into systematic imbalance and random imbalance," *IEEE Transactions on Power Systems*, vol. 33, no. 3, pp. 3001–3012, 2017.

[48] M. W. Siti, D. V. Nicolae, A. A. Jimoh, and A. Ukil, "Reconfiguration and load balancing in the lv and mv distribution networks for optimal performance," *IEEE transactions on power delivery*, vol. 22, no. 4, pp. 2534–2540, 2007.

[49] K. Ma, R. Li, and F. Li, "Quantification of additional asset reinforcement cost from 3-phase imbalance," *IEEE Transactions on Power Systems*, vol. 31, no. 4, pp. 2885–2891, 2015.

[50] A. P. Hota, S. Mishra, and D. P. Mishra, "Active power loss allocation in radial distribution networks with different load models and dgs," *Electric Power Systems Research*, vol. 205, p. 107764, 2022.

[51] A. P. Hota, S. Mishra, and D. P. Mishra, "Loss allocation strategies in active power distribution networks: a review," *Advances in Electrical Control and Signal Systems: Select Proceedings of AECSS 2019*, pp. 889–902, 2020.

[52] V. B. Pamshetti, S. Singh, A. K. Thakur, and S. Singh, "Multistage coordination volt/var control with cvr in active distribution network in presence of inverter-based dg units and

soft open points," *IEEE Transactions on Industry Applications*, vol. 57, no. 3, pp. 2035–2047, 2021.

[53] J. Song, Y. Zhang, Z. Gao, C. Cao, Z. Wang, and F. Xu, "Research on topology and control technology of soft multi-state open point with fault isolation capability," in *2018 China International Conference on Electricity Distribution (CICED)*, pp. 1467–1473, IEEE, 2018.

[54] N. Okada, M. Takasaki, H. Sakai, and S. Katoh, "Development of a 6.6 kv-1 mva transformerless loop balance controller," in *2007 IEEE Power Electronics Specialists Conference*, pp. 1087–1091, IEEE, 2007.

[55] W. Cao, J. Wu, and N. Jenkins, "Feeder load balancing in mv distribution networks using soft normally-open points," in *IEEE PES Innovative Smart Grid Technologies, Europe*, pp. 1–6, IEEE, 2014.

[56] W. Cao, J. Wu, N. Jenkins, C. Wang, and T. Green, "Operating principle of soft open points for electrical distribution network operation," *Applied Energy*, vol. 164, pp. 245–257, 2016.

[57] P. S. Georgilakis and N. D. Hatziargyriou, "Unified power flow controllers in smart power systems: models, methods, and future research," *IET Smart Grid*, vol. 2, no. 1, pp. 2–10, 2019.

[58] H. Ji, H. Yu, G. Song, P. Li, C. Wang, and J. Wu, "A decentralized voltage control strategy of soft open points in active distribution networks," *Energy Procedia*, vol. 159, pp. 412–417, 2019.

[59] H. Hafezi and H. Laaksonen, "Autonomous soft open point control for active distribution network voltage level management," in *2019 IEEE Milan PowerTech*, pp. 1–6, IEEE, 2019.

[60] M. A. Sayed and T. Takeshita, "Line loss minimization in isolated substations and multiple loop distribution systems using the upfc," *IEEE Transactions on power electronics*, vol. 29, no. 11, pp. 5813–5822, 2014.

[61] L. F. Costa, G. De Carne, G. Buticchi, and M. Liserre, "The smart transformer: A solid-state transformer tailored to provide ancillary services to the distribution grid," *IEEE Power Electronics Magazine*, vol. 4, no. 2, pp. 56–67, 2017.

[62] H. Ji, C. Wang, P. Li, J. Zhao, G. Song, and J. Wu, "Quantified flexibility evaluation of soft open points to improve distributed generator penetration in active distribution networks based on difference-of-convex programming," *Applied Energy*, vol. 218, pp. 338–348, 2018.

[63] J. Wang, N. Zhou, Y. Ran, and Q. Wang, "Reducing the active power curtailment of distributed generation based on soft open points in unbalanced distribution networks," *IET Renewable Power Generation*, vol. 14, no. 16, pp. 3252–3258, 2020.

[64] H. Ji, C. Wang, P. Li, J. Zhao, G. Song, F. Ding, and J. Wu, "An enhanced socp-based method for feeder load balancing using the multi-terminal soft open point in active distribution networks," *Applied energy*, vol. 208, pp. 986–995, 2017.

[65] C. Yao, C. Zhou, J. Yu, K. Xu, P. Li, and G. Song, "A sequential optimization method for soft open point integrated with energy storage in active distribution networks," *Energy Procedia*, vol. 145, pp. 528–533, 2018.

[66] F. Attanasio, S. Wasterlain, T. Pidancier, M. Marchesoni, P. Favre-Perrod, and M. Carpita, “Low voltage soft open point with energy storage: system simulation and prototype preliminary test results,” in *2018 International Symposium on Power Electronics, Electrical Drives, Automation and Motion (SPEEDAM)*, pp. 254–261, IEEE, 2018.

[67] B. Li, Y. Liang, G. Wang, H. Li, and J. Ding, “A control strategy for soft open points based on adaptive voltage droop outer-loop control and sliding mode inner-loop control with feedback linearization,” *International Journal of Electrical Power & Energy Systems*, vol. 122, p. 106205, 2020.

[68] M. Li, H. Yang, R. Zhao, T. Zheng, C. Si, Y. Lu, and Y. Yang, “Comparative study on the operating area of m 3 c and b2b mmc for soft open point application,” in *2019 10th International Conference on Power Electronics and ECCE Asia (ICPE 2019-ECCE Asia)*, pp. 1205–1212, IEEE, 2019.

[69] J. M. Bloemink and T. C. Green, “Increasing photovoltaic penetration with local energy storage and soft normally-open points,” in *2011 IEEE power and energy society general meeting*, pp. 1–8, IEEE, 2011.

[70] Y. Zheng, Y. Song, and D. J. Hill, “A general coordinated voltage regulation method in distribution networks with soft open points,” *International Journal of Electrical Power & Energy Systems*, vol. 116, p. 105571, 2020.

[71] S. Ouyang, J. Liu, Y. Yang, X. Chen, S. Song, and H. Wu, “Dc voltage control strategy of three-terminal medium-voltage power electronic transformer-based soft normally open points,” *IEEE Transactions on Industrial Electronics*, vol. 67, no. 5, pp. 3684–3695, 2019.

[72] R. Zhang, V. H. Prasad, D. Boroyevich, and F. C. Lee, “Three-dimensional space vector modulation for four-leg voltage-source converters,” *IEEE Transactions on power electronics*, vol. 17, no. 3, pp. 314–326, 2002.

[73] P. Hayashi and L. Matakas, “Decoupled stationary abc frame current control of three-phase four-leg four-wire converters,” in *2017 Brazilian Power Electronics Conference (COBEP)*, pp. 1–6, IEEE, 2017.

[74] M. Dai, M. N. Marwali, J.-W. Jung, and A. Keyhani, “A three-phase four-wire inverter control technique for a single distributed generation unit in island mode,” *IEEE Transactions on power electronics*, vol. 23, no. 1, pp. 322–331, 2008.

[75] D. I. Brandao, F. E. Mendes, R. V. Ferreira, S. M. Silva, and I. A. Pires, “Active and reactive power injection strategies for three-phase four-wire inverters during symmetrical/asymmetrical voltage sags,” *IEEE transactions on industry applications*, vol. 55, no. 3, pp. 2347–2355, 2019.

[76] J. S. Döhler, R. P. Mota, J. A. G. Archetti, D. C. S. Júnior, C. Boström, and J. G. Oliveira, “An application of four-wire grid-forming power inverter in unbalanced distribution network,” *IET Generation, Transmission & Distribution*, vol. 17, no. 2, pp. 324–336, 2023.

[77] F. Wu, B. Miao, S. Peng, M. Li, and S. Wen, “Analysis of the mechanism and control of the unbalanced operation of three-phase four-wire inverters,” *Applied Sciences*, vol. 13, no. 22, 2023.

[78] N. R. Chaudhuri, R. Majumder, B. Chaudhuri, and J. Pan, “Stability analysis of vsc mtdc grids connected to multimachine ac systems,” *IEEE Transactions on Power Delivery*, vol. 26, no. 4, pp. 2774–2784, 2011.

[79] I. J. Balaguer, Q. Lei, S. Yang, U. Supatti, and F. Z. Peng, "Control for grid-connected and intentional islanding operations of distributed power generation," *IEEE transactions on industrial electronics*, vol. 58, no. 1, pp. 147–157, 2010.

[80] Y. Li, X. Pei, Z. Chen, M. Yang, Z. Lyu, and C. Wang, "The steady-state and fault ride-through control strategies of soft normally open point in distribution network," in *2018 IEEE Energy Conversion Congress and Exposition (ECCE)*, pp. 1146–1150, IEEE, 2018.

[81] W. Taha, M. Bakr, and A. Emadi, "Pi controller tuning optimization for grid-connected vsc using space mapping," in *2020 IEEE Energy Conversion Congress and Exposition (ECCE)*, pp. 5689–5695, IEEE, 2020.

[82] W. Gil-González, S. Sanchez, O. Montoya, and V. Garrido, "Vsc with direct pi power control for frequency compensation in a microgrid: a pbc approach," in *2019 IEEE XXVI International Conference on Electronics, Electrical Engineering and Computing (INTERCON)*, pp. 1–4, IEEE, 2019.

[83] F. Gao and M. R. Iravani, "A control strategy for a distributed generation unit in grid-connected and autonomous modes of operation," *IEEE Transactions on power delivery*, vol. 23, no. 2, pp. 850–859, 2008.

[84] C. Lou, J. Yang, E. Vega-Fuentes, N. K. Meena, and L. Min, "Multi-terminal phase-changing soft open point sdp modeling for imbalance mitigation in active distribution networks," *International Journal of Electrical Power & Energy Systems*, vol. 142, p. 108228, 2022.

[85] C. Lou, J. Yang, and L. Min, "Symmetrical semidefinite programming with bifurcation phase-changing sops for unbalanced power distribution networks," in *2021 IEEE 5th*

conference on energy internet and energy system integration (EI2), pp. 1242–1247, IEEE, 2021.

[86] H. Ji, C. Wang, P. Li, F. Ding, and J. Wu, “Robust operation of soft open points in active distribution networks with high penetration of photovoltaic integration,” *IEEE Transactions on Sustainable Energy*, vol. 10, no. 1, pp. 280–289, 2018.

[87] P. Li, H. Ji, C. Wang, J. Zhao, G. Song, F. Ding, and J. Wu, “Optimal operation of soft open points in active distribution networks under three-phase unbalanced conditions,” *IEEE Transactions on Smart Grid*, vol. 10, no. 1, pp. 380–391, 2017.

[88] C. Wang, G. Song, P. Li, H. Ji, J. Zhao, and J. Wu, “Optimal siting and sizing of soft open points in active electrical distribution networks,” *Applied energy*, vol. 189, pp. 301–309, 2017.

[89] L. Bai, T. Jiang, F. Li, H. Chen, and X. Li, “Distributed energy storage planning in soft open point based active distribution networks incorporating network reconfiguration and dg reactive power capability,” *Applied Energy*, vol. 210, pp. 1082–1091, 2018.

[90] P. Li, H. Ji, C. Wang, J. Zhao, G. Song, F. Ding, and J. Wu, “Coordinated control method of voltage and reactive power for active distribution networks based on soft open point,” *IEEE Transactions on Sustainable Energy*, vol. 8, no. 4, pp. 1430–1442, 2017.

[91] C. Wang, G. Song, P. Li, H. Ji, J. Zhao, and J. Wu, “Optimal configuration of soft open point for active distribution network based on mixed-integer second-order cone programming,” *Energy Procedia*, vol. 103, pp. 70–75, 2016.

[92] T. Ding, Z. Wang, W. Jia, B. Chen, C. Chen, and M. Shahidehpour, “Multiperiod distribution system restoration with routing repair crews, mobile electric vehicles, and soft-

open-point networked microgrids," *IEEE Transactions on Smart Grid*, vol. 11, no. 6, pp. 4795–4808, 2020.

[93] L. Zhang, C. Shen, Y. Chen, S. Huang, and W. Tang, "Coordinated allocation of distributed generation, capacitor banks and soft open points in active distribution networks considering dispatching results," *Applied energy*, vol. 231, pp. 1122–1131, 2018.

[94] S. Liao, H. Liu, B. Liu, H. Zhao, and M. Wang, "An information gap decision theory-based decision-making model for complementary operation of hydro-wind-solar system considering wind and solar output uncertainties," *Journal of Cleaner Production*, vol. 348, p. 131382, 2022.

[95] Y. Jiang, J. Xu, Y. Sun, C. Wei, J. Wang, S. Liao, D. Ke, X. Li, J. Yang, and X. Peng, "Coordinated operation of gas-electricity integrated distribution system with multi-cchp and distributed renewable energy sources," *Applied energy*, vol. 211, pp. 237–248, 2018.

[96] R. Li, W. Wang, X. Wu, F. Tang, and Z. Chen, "Cooperative planning model of renewable energy sources and energy storage units in active distribution systems: A bi-level model and pareto analysis," *Energy*, vol. 168, pp. 30–42, 2019.

[97] I. Petkov and P. Gabrielli, "Power-to-hydrogen as seasonal energy storage: an uncertainty analysis for optimal design of low-carbon multi-energy systems," *Applied Energy*, vol. 274, p. 115197, 2020.

[98] C. Moeller, J. Meiss, B. Mueller, M. Hlusiak, C. Breyer, M. Kastner, and J. Twele, "Transforming the electricity generation of the berlin–brandenburg region, germany," *Renewable Energy*, vol. 72, pp. 39–50, 2014.

[99] H. Blanco, W. Nijs, J. Ruf, and A. Faaij, “Potential of power-to-methane in the eu energy transition to a low carbon system using cost optimization,” *Applied energy*, vol. 232, pp. 323–340, 2018.

[100] C. Gu, Y. Zhang, J. Wang, and Q. Li, “Joint planning of electrical storage and gas storage in power-gas distribution network considering high-penetration electric vehicle and gas vehicle,” *Applied Energy*, vol. 301, p. 117447, 2021.

[101] X. Xing, J. Lin, Y. Song, Y. Zhou, S. Mu, and Q. Hu, “Modeling and operation of the power-to-gas system for renewables integration: a review,” *CSEE Journal of Power and Energy Systems*, vol. 4, no. 2, pp. 168–178, 2018.

[102] C. Wulf, J. Linssen, and P. Zapp, “Power-to-gas—concepts, demonstration, and prospects,” in *Hydrogen supply chains*, pp. 309–345, Elsevier, 2018.

[103] C. Baumann, R. Schuster, and A. Moser, “Economic potential of power-to-gas energy storages,” in *2013 10th International Conference on the European Energy Market (EEM)*, pp. 1–6, IEEE, 2013.

[104] Q. Wu, Q. Hu, L. Hang, A. Botterud, and E. Muljadi, “Power to gas for future renewable based energy systems,” *IET Renewable Power Generation*, vol. 14, no. 17, pp. 3281–3283, 2021.

[105] J. Fan, X. Tong, and J. Zhao, “Multi-period optimal energy flow for electricity-gas integrated systems considering gas inertia and wind power uncertainties,” *International Journal of Electrical Power & Energy Systems*, vol. 123, p. 106263, 2020.

[106] S. Wang, J. Zhai, and H. Hui, “Optimal energy flow in integrated electricity and gas systems with injection of alternative gas,” *IEEE Transactions on Sustainable Energy*, 2023.

[107] F. Liu, Z. Bie, and X. Wang, "Day-ahead dispatch of integrated electricity and natural gas system considering reserve scheduling and renewable uncertainties," *IEEE Transactions on Sustainable Energy*, vol. 10, no. 2, pp. 646–658, 2018.

[108] F. Qi, M. Shahidehpour, F. Wen, Z. Li, Y. He, and M. Yan, "Decentralized privacy-preserving operation of multi-area integrated electricity and natural gas systems with renewable energy resources," *IEEE Transactions on Sustainable Energy*, vol. 11, no. 3, pp. 1785–1796, 2019.

[109] F. Qi, M. Shahidehpour, Z. Li, F. Wen, and C. Shao, "A chance-constrained decentralized operation of multi-area integrated electricity–natural gas systems with variable wind and solar energy," *IEEE Transactions on Sustainable Energy*, vol. 11, no. 4, pp. 2230–2240, 2019.

[110] L. Yang, Y. Xu, W. Gu, and H. Sun, "Distributionally robust chance-constrained optimal power-gas flow under bidirectional interactions considering uncertain wind power," *IEEE Transactions on Smart Grid*, vol. 12, no. 2, pp. 1722–1735, 2020.

[111] S. Chen, A. J. Conejo, R. Sioshansi, and Z. Wei, "Unit commitment with an enhanced natural gas-flow model," *IEEE Transactions on Power Systems*, vol. 34, no. 5, pp. 3729–3738, 2019.

[112] A. Schwele, A. Arrigo, C. Vervaeren, J. Kazempour, and F. Vallée, "Coordination of electricity, heat, and natural gas systems accounting for network flexibility," *Electric Power Systems Research*, vol. 189, p. 106776, 2020.

[113] A. Turk, Q. Wu, M. Zhang, and J. Østergaard, "Day-ahead stochastic scheduling of integrated multi-energy system for flexibility synergy and uncertainty balancing," *Energy*, vol. 196, p. 117130, 2020.

[114] R. Yan, Z. Lu, J. Wang, H. Chen, J. Wang, Y. Yang, and D. Huang, “Stochastic multi-scenario optimization for a hybrid combined cooling, heating and power system considering multi-criteria,” *Energy Conversion and Management*, vol. 233, p. 113911, 2021.

[115] A. Zakaria, F. B. Ismail, M. H. Lipu, and M. A. Hannan, “Uncertainty models for stochastic optimization in renewable energy applications,” *Renewable Energy*, vol. 145, pp. 1543–1571, 2020.

[116] M. Wang, H. Yu, X. Lin, R. Jing, F. He, and C. Li, “Comparing stochastic programming with posteriori approach for multi-objective optimization of distributed energy systems under uncertainty,” *Energy*, vol. 210, p. 118571, 2020.

[117] K. Seddig, P. Jochem, and W. Fichtner, “Two-stage stochastic optimization for cost-minimal charging of electric vehicles at public charging stations with photovoltaics,” *Applied energy*, vol. 242, pp. 769–781, 2019.

[118] F. Mei, J. Zhang, J. Lu, J. Lu, Y. Jiang, J. Gu, K. Yu, and L. Gan, “Stochastic optimal operation model for a distributed integrated energy system based on multiple-scenario simulations,” *Energy*, vol. 219, p. 119629, 2021.

[119] P. Li, Z. Wang, J. Wang, W. Yang, T. Guo, and Y. Yin, “Two-stage optimal operation of integrated energy system considering multiple uncertainties and integrated demand response,” *Energy*, vol. 225, p. 120256, 2021.

[120] K. Li, F. Yang, L. Wang, Y. Yan, H. Wang, and C. Zhang, “A scenario-based two-stage stochastic optimization approach for multi-energy microgrids,” *Applied Energy*, vol. 322, p. 119388, 2022.

[121] G. Mavromatidis, K. Orehounig, and J. Carmeliet, "Uncertainty and global sensitivity analysis for the optimal design of distributed energy systems," *Applied Energy*, vol. 214, pp. 219–238, 2018.

[122] A. Agrawal, R. Verschueren, S. Diamond, and S. Boyd, "A rewriting system for convex optimization problems," *Journal of Control and Decision*, vol. 5, no. 1, pp. 42–60, 2018.

[123] J. Sun and L. Tesfatsion, "Dc optimal power flow formulation and solution using quadprogj," 2010.

[124] C. Coffrin and P. Van Hentenryck, "A linear-programming approximation of ac power flows," *INFORMS Journal on Computing*, vol. 26, no. 4, pp. 718–734, 2014.

[125] J. D. Watson, N. R. Watson, and I. Lestas, "Optimized dispatch of energy storage systems in unbalanced distribution networks," *IEEE Transactions on Sustainable Energy*, vol. 9, no. 2, pp. 639–650, 2017.

[126] R. A. Jabr, "Exploiting sparsity in sdp relaxations of the opf problem," *IEEE Transactions on Power Systems*, vol. 27, no. 2, pp. 1138–1139, 2011.

[127] W. Wang and N. Yu, "Chordal conversion based convex iteration algorithm for three-phase optimal power flow problems," *IEEE Transactions on Power Systems*, vol. 33, no. 2, pp. 1603–1613, 2017.

[128] S. Bruno, S. Lamonaca, G. Rotondo, U. Stecchi, and M. La Scala, "Unbalanced three-phase optimal power flow for smart grids," *IEEE Transactions on Industrial Electronics*, vol. 58, no. 10, pp. 4504–4513, 2011.

[129] E. Dall'Anese, H. Zhu, and G. B. Giannakis, "Distributed optimal power flow for smart microgrids," *IEEE Transactions on Smart Grid*, vol. 4, no. 3, pp. 1464–1475, 2013.

[130] L. Gan and S. H. Low, "Convex relaxations and linear approximation for optimal power flow in multiphase radial networks," in *2014 Power Systems Computation Conference*, pp. 1–9, IEEE, 2014.

[131] Z. Wang, D. S. Kirschen, and B. Zhang, "Accurate semidefinite programming models for optimal power flow in distribution systems," *arXiv preprint arXiv:1711.07853*, 2017.

[132] S. Low, "Convex relaxation of optimal power flow, i: formulations and relaxations," *IEEE Trans. on Control of Network Systems*, vol. 1, no. 1, pp. 15–27, 2014.

[133] S. P. Boyd and L. Vandenberghe, *Convex optimization*. Cambridge university press, 2004.

[134] J. Jalving, S. Abhyankar, K. Kim, M. Hereld, and V. M. Zavala, "A graph-based computational framework for simulation and optimisation of coupled infrastructure networks," *IET Generation, Transmission & Distribution*, vol. 11, no. 12, pp. 3163–3176, 2017.

[135] J. Jalving, Y. Cao, and V. M. Zavala, "Graph-based modeling and simulation of complex systems," *Computers & Chemical Engineering*, vol. 125, pp. 134–154, 2019.

[136] M. Moharir, L. Kang, P. Daoutidis, and A. Almansoori, "Graph representation and decomposition of ode/hyperbolic pde systems," *Computers & Chemical Engineering*, vol. 106, pp. 532–543, 2017.

[137] W. Tang and P. Daoutidis, "Network decomposition for distributed control through community detection in input–output bipartite graphs," *Journal of Process Control*, vol. 64, pp. 7–14, 2018.

[138] V. M. Zavala, C. D. Laird, and L. T. Biegler, “Interior-point decomposition approaches for parallel solution of large-scale nonlinear parameter estimation problems,” *Chemical Engineering Science*, vol. 63, no. 19, pp. 4834–4845, 2008.

[139] J. Kang, Y. Cao, D. P. Word, and C. D. Laird, “An interior-point method for efficient solution of block-structured nlp problems using an implicit schur-complement decomposition,” *Computers & Chemical Engineering*, vol. 71, pp. 563–573, 2014.

[140] S. Heo, S. Rangarajan, P. Daoutidis, and S. S. Jogwar, “Graph reduction of complex energy-integrated networks: Process systems applications,” *AIChE Journal*, vol. 60, no. 3, pp. 995–1012, 2014.

[141] S. S. Jogwar, S. Rangarajan, and P. Daoutidis, “Reduction of complex energy-integrated process networks using graph theory,” *Computers & Chemical Engineering*, vol. 79, pp. 46–58, 2015.

[142] J. Jalving, S. Shin, and V. M. Zavala, “A graph-based modeling abstraction for optimization: Concepts and implementation in plasmo. jl,” *Mathematical Programming Computation*, vol. 14, no. 4, pp. 699–747, 2022.

[143] S. Shin, C. Coffrin, K. Sundar, and V. M. Zavala, “Graph-based modeling and decomposition of energy infrastructures,” *IFAC-PapersOnLine*, vol. 54, no. 3, pp. 693–698, 2021.

[144] D. L. Cole, S. Shin, and V. M. Zavala, “A julia framework for graph-structured nonlinear optimization,” *Industrial & Engineering Chemistry Research*, vol. 61, no. 26, pp. 9366–9380, 2022.

[145] Y. Cai, Z. Qu, H. Yang, R. Zhao, Y. Lu, and Y. Yang, "Research on an improved droop control strategy for soft open point," in *2018 21st International Conference on Electrical Machines and Systems (ICEMS)*, pp. 2000–2005, IEEE, 2018.

[146] J. M. Bloemink and T. C. Green, "Benefits of distribution-level power electronics for supporting distributed generation growth," *IEEE Transactions on Power Delivery*, vol. 28, no. 2, pp. 911–919, 2013.

[147] B. Jacobson, Y. Jiang-Hafner, P. Rey, G. Asplund, M. Jeroense, A. Gustafsson, and M. Bergkvist, "Hvdc with voltage source converters and extruded cables for up to±300 kv and 1000 mw," *Proc. CIGRÉ*, pp. B4–105, 2006.

[148] J. Zhenhua and Y. Xunwei, "Active power-voltage control scheme for islanding operation of inverter-interfaced microgrids," in *2009 IEEE Power & Energy Society General Meeting (PES)*, pp. 7–7, 2009.

[149] L. Min, J. Yang, C. Lou, and J. Yu, "Phase-changing control for three-phase four-wire back-to-back vsc based soft open points," in *11th International Conference on Renewable Power Generation-Meeting net zero carbon (RPG 2022)*, vol. 2022, pp. 110–114, IET, 2022.

[150] D. A. Fernandes, F. F. Costa, M. A. Vitorino, K. I. Queiroz, and F. Salvadori, "Carrier-based pwm scheme for three-phase four-leg inverters," in *IECON 2013-39th Annual Conference of the IEEE Industrial Electronics Society*, pp. 3353–3358, IEEE, 2013.

[151] C. B. Jacobina, A. N. Lima, E. R. C. da Silva, R. N. C. Alves, and P. F. Seixas, "Digital scalar pulse-width modulation: a simple approach to introduce nonsinusoidal modulating waveforms," *IEEE Transactions on Power Electronics*, vol. 16, no. 3, pp. 351–359, 2001.

[152] J. Shang, H. Liu, R. Zhang, and J. Wang, “Optimal economic operation of active distribution networks with energy storage integrated sop,” in *2022 IEEE 3rd China International Youth Conference on Electrical Engineering (CIYCEE)*, pp. 1–5, IEEE, 2022.

[153] F. Gao, L. Zhang, Q. Zhou, M. Chen, T. Xu, and S. Hu, “State-of-charge balancing control strategy of battery energy storage system based on modular multilevel converter,” in *2014 IEEE Energy Conversion Congress and Exposition (ECCE)*, pp. 2567–2574, IEEE, 2014.

[154] X. Qiu, Y. Guo, J. Zhang, H. Zhao, X. Peng, Z. Wu, R. Tian, and J. Yang, “State of charge estimation of lithium battery energy storage systems based on adaptive correntropy unscented kalman filter,” in *2020 5th Asia Conference on Power and Electrical Engineering (ACPEE)*, pp. 851–857, IEEE, 2020.

[155] A. Floriduz, M. Tucci, S. Riverso, and G. Ferrari-Trecate, “Approximate kron reduction methods for electrical networks with applications to plug-and-play control of ac islanded microgrids,” *IEEE Transactions on Control Systems Technology*, vol. 27, no. 6, pp. 2403–2416, 2018.

[156] K. P. Schneider, B. Mather, B. C. Pal, C.-W. Ten, G. J. Shirek, H. Zhu, J. C. Fuller, J. L. R. Pereira, L. F. Ochoa, L. R. de Araujo, *et al.*, “Analytic considerations and design basis for the ieee distribution test feeders,” *IEEE Transactions on power systems*, vol. 33, no. 3, pp. 3181–3188, 2017.

[157] Y. Peng, H. Ishibuchi, and K. Shang, “Multi-modal multi-objective optimization: problem analysis and case studies,” in *2019 IEEE Symposium Series on Computational Intelligence (SSCI)*, pp. 1865–1872, IEEE, 2019.

[158] B. Ahmadi, A. Pappu, G. Hoogsteen, and J. L. Hurink, “Multi-objective optimization framework for integration of distributed energy resources in smart communities,” in

2022 57th International Universities Power Engineering Conference (UPEC), pp. 1–6, IEEE, 2022.

[159] A. M. Jubril, O. A. Komolafe, and K. O. Alawode, "Solving multi-objective economic dispatch problem via semidefinite programming," *IEEE Transactions on power systems*, vol. 28, no. 3, pp. 2056–2064, 2013.

[160] T. L. Saaty, "Decision making—the analytic hierarchy and network processes (ahp/anp)," *Journal of systems science and systems engineering*, vol. 13, pp. 1–35, 2004.

[161] J. Lofberg, "Yalmip: A toolbox for modeling and optimization in matlab," in *2004 IEEE international conference on robotics and automation (IEEE Cat. No. 04CH37508)*, pp. 284–289, IEEE, 2004.

[162] Z. Tian, W. Wu, B. Zhang, and A. Bose, "Mixed-integer second-order cone programing model for var optimisation and network reconfiguration in active distribution networks," *IET Generation, Transmission & Distribution*, vol. 10, no. 8, pp. 1938–1946, 2016.

[163] C. Lou, J. Yang, T. Li, and E. Vega-Fuentes, "New phase-changing soft open point and impacts on optimising unbalanced power distribution networks," *IET generation, transmission & distribution*, vol. 14, no. 23, pp. 5685–5696, 2020.

[164] W. Tang, T. Li, W. Zhang, *et al.*, "Coordinated control of photovoltaic and energy storage system in low-voltage distribution networks based on three-phase four-wire optimal power flow," *Autom Electr Power Syst*, vol. 44, no. 12, pp. 31–42, 2020.

[165] Y. Cai, W. Tang, B. Zhang, and Y. Wang, "Collaborative configuration for distributed energy storages and cyber systems in low-voltage distribution networks with high penetration of pv systems," *IET Cyber-Physical Systems: Theory & Applications*, vol. 4, no. 1, pp. 3–12, 2019.

[166] H. Espeland, P. B. Beskow, H. K. Stensland, P. N. Olsen, S. Kristoffersen, C. Griwodz, and P. Halvorsen, "P2g: A framework for distributed real-time processing of multimedia data," in *2011 40th International Conference on Parallel Processing Workshops*, pp. 416–426, IEEE, 2011.

[167] S. Akbar, N. Liu, T. Khan, and S. Alam, "A review of the main technologies andapplication potentials of p2g system for renewable integration," in *2020 IEEE International Conference on Advent Trends in Multidisciplinary Research and Innovation (ICATMRI)*, pp. 1–9, IEEE, 2020.

[168] A. Arsad, M. Hannan, A. Q. Al-Shetwi, R. Begum, M. Hossain, P. J. Ker, and T. I. Mahlia, "Hydrogen electrolyser technologies and their modelling for sustainable energy production: a comprehensive review and suggestions," *International Journal of Hydrogen Energy*, 2023.

[169] Z. Yang, C. Gao, and M. Zhao, "The optimal investment strategy of p2g based on real option theory," *IEEE Access*, vol. 8, pp. 127156–127166, 2019.

[170] S. E. Networks, "Distribution future energy scenarios (2023)." `https://www.spenergynetworks.co.uk/pages/distribution_future_energy_scenarios.aspx`, 2023. Accessed: 17-Oct-2023.

[171] I. PES, "Ieee pes amps dsas test feeder working group." `https://site.ieee.org/pes-testfeeders/resources/`. Accessed: 2021-05-05.

Publications

Published Articles in Journal

[1] **L. Min**, C. Lou, J. Yang, J. Yu, Z. Yu, J. Cunningham. "Optimal Unbalanced Operation of All-Switching-Phase Soft Open Points Based on Symmetrical Semidefinite Programming”. Protection and Control of Modern Power Systems (Under Second Review)

[2] **L. Min**, C. Lou, J. Yang, J. Yu, Z. Yu. "Operational Coordination of Electricity and Natural Gas Networks with Power-to-Gas based on Symmetrical Semidefinite Programming". Modern Power Systems and Clean Energy (Under Second Review)

[3] **MIN Liang**, LOU Chengwei, YANG Jin, et al. Multi-objective Operation Optimization of Active Distribution Network Considering Three-phase Unbalance Regulation of Phase-switching Soft Open Points[J]. Automation of Electric Power Systems, 2023, 47(12):56-65. DOI:10.7500/AEPS20220917010.

[4] Lou, Chengwei, Jin Yang, Yue Zhou, Eduardo Vega-Fuentes, Nand K. Meena, and **Liang Min**. "Multi-terminal phase-changing soft open point SDP modeling for imbalance mitigation in active distribution networks." International Journal of Electrical Power & Energy Systems 142 (2022): 108228.

[5] Chengwei Lou, Jin Yang, Eduardo Vega Fuentes, Yue Zhou, **Liang Min**, James Yu, Nand Kishor Meena. "Power flow traceable P2P electricity market segmentation and cost allocation." Energy (2023): 130120.

Published Articles in Conference Proceeding

[1] **L. Min**, J. Yang, C. Lou and J. Yu, "Phase-changing control for three-phase four-wire back-to-back VSC based soft open points," 11th International Conference on Renewable Power Generation - Meeting net zero carbon (RPG 2022), Hybrid Conference, London, UK, 2022, pp. 110-114, doi: 10.1049/icp.2022.1683.

[2] Lou, Chengwei, Jin Yang, and **Liang Min**. "Symmetrical semidefinite programming with bifurcation phase-changing SOPs for unbalanced power distribution networks." 2021 IEEE 5th conference on energy internet and energy system integration (EI2). IEEE, 2021.